# LEAKAGE FLOW MODELING FOR MULTIPHASE TWIN SCREW PUMPS

A Thesis

by

JEFFREY SHIAO-JEH SHIVE

Submitted to the Office of Graduate and Professional Studies of
Texas A&M University
in partial fulfillment of the requirements for the degree of

MASTER OF SCIENCE

| | |
|---|---|
| Chair of Committee, | Gerald L. Morrison |
| Committee Members, | Je-Chin Han |
| | Karen Vierow |
| Head of Department, | Andreas A. Polycarpou |

May 2017

Major Subject: Mechanical Engineering

Copyright 2017 Jeffrey Shiao-Jeh Shive

# ABSTRACT

Twin screw pumps (TSPs) are commonly used for multiphase boosting systems to enhance oil and gas production. TSPs are a positive displacement pump that can efficiently handle fluids with a wide range of gas volume fractions (GVFs). The present study has developed a model to predict the performance of TSPs for varying GVFs, pump speeds, suction pressures, and differential pressures. A two-phase compressible flow model is used to determine the rate of leakage backflow through clearances within the pump. The model incorporates the possibility of choking due to sonic flow. Hydraulic imbalances cause rotor deflection, and the model accounts for increased leakage flowrates due to the induced eccentric rotation. The model was validated with experimental data from a Colfax MR-200 TSP, and there is good agreement in most test cases. However, cases with low speeds and high differential pressures were not as reliable. This may be due to uncertainty of the rates of gas infiltration into the clearances at low pump speeds. The study reveals that pump performance is generally better when operating at high pump speeds, high GVF, low suction pressures, or low differential pressures. Linear pressure distributions throughout the pump's chambers generally indicate lower volumetric efficiency compared to steep, concave pressure distributions. The effects of rotor deflection are generally small, but in a few cases they should not be ignored. Choking occurred at the circumferential, flank, and root clearances in 18%, 13%, and 99% of the test cases, respectively. The presence of choked leakage flow marginally improved the pump performance.

# ACKNOWLEDGEMENTS

I would like to thank my committee chair, Dr. Gerald Morrison, for being a wonderful advisor. He has shown me much support and patience throughout the course of this research. I would also like to thank my committee members, Dr. Je-Chin Han and Dr. Karen Vierow Kirkland, for their guidance and support.

Thank you to Dr. Abhay Patil for all of his help and advice whenever I ran into difficulties. Thank you to my labmates for making my time here a great experience. Thank you to all of my friends at Texas A&M for being able to share our fun and hardships together.

Lastly, thank you to my family for their support, and thank you to my girlfriend for all of her love and encouragement.

# CONTRIBUTORS AND FUNDING SOURCES

## Contributors Section

### *Part 1, faculty committee recognition*

This work was supervised by a thesis committee consisting of Dr. Gerald Morrison of the Department of Mechanical Engineering, Dr. Je-Chin Han of the Department of Mechanical Engineering, and Dr. Karen Vierow Kirkland of the Department of Nuclear Engineering.

### *Part 2, student/collaborator contributions*

All work for the thesis was completed by the student, under the advisement of Dr. Gerald Morrison and Dr. Abhay Patil.

## Funding Section

Graduate study was supported by graduate teaching assistantships and a fellowship from Texas A&M University.

# NOMENCLATURE

## Latin

| | |
|---|---|
| $a$ | distance between spindle axes |
| $A_{cc}$ | cross-sectional area of the circumferential clearance |
| $A_{fc,s}$ | surface area of the flank clearance |
| $B$ | width of the screw land |
| $c$ | speed of sound |
| $c_p$ | specific heat at constant pressure |
| $c_v$ | specific heat at constant volume |
| $D_i$ | inner diameter |
| $D_o$ | outer diameter |
| $f$ | Darcy friction factor |
| $F_r$ | radial force |
| $h$ | screw pitch |
| $h$ | enthalpy |
| $H_{fc}$ | width of the flank clearance |
| $k$ | polytropic coefficient |
| $k_e$ | loss coefficient at clearance entrance |
| $L_{cc}$ | length of the circumferential clearance |
| $L_{fc}$ | length of the approximated flank clearance |
| $L_{fc,a}$ | length of the actual flank clearance |

| | |
|---|---|
| $m$ | mass |
| $M$ | Mach number |
| $n$ | number of threads |
| $N$ | pump speed |
| $P$ | power |
| $P$ | pressure |
| $\Delta P_i$ | pressure rise between consecutive chambers |
| $Q_{lkg}$ | leakage volumetric flowrate |
| $Q_{th}$ | theoretical volumetric flowrate |
| $R$ | specific gas constant |
| $R_i$ | inner radius |
| $R_o$ | outer radius |
| Re | Reynolds number |
| $T$ | temperature |
| $T_0$ | stagnation temperature |
| $U$ | internal energy |
| $V$ | velocity |
| $V_{lkg}$ | leakage flow velocity |
| $x$ | quality or gas mass fraction |

**Greek**

| | |
|---|---|
| $\alpha$ | gas volume fraction |
| $\alpha_{ch}$ | gas volume fraction of a chamber |
| $\alpha_s$ | spindle inclination angle |
| $\beta$ | angle between the centerline and the overlap of the screws |
| $\gamma$ | ratio of specific heats |
| $\delta_{cc}$ | thickness of the circumferential clearance |
| $\delta_{fc}$ | thickness of the flank clearance |
| $\delta_{rc}$ | thickness of the root clearance |
| $\eta_{eff}$ | pump effectiveness |
| $\eta_{mech}$ | mechanical efficiency |
| $\eta_v$ | volumetric efficiency |
| $\mu_G$ | viscosity of gas |
| $\mu_L$ | viscosity of liquid |
| $\rho_G$ | density of gas |
| $\rho_L$ | density of liquid |
| $\sigma$ | standard deviation |
| $\omega$ | rotational speed |

## Abbreviations

| | |
|---|---|
| CC | circumferential clearance |
| CV | control volume |
| dP | differential pressure |
| ESP | electrical submersible pump |
| FC | flank clearance |
| GVF | gas volume fraction |
| RC | root clearance |
| TSP | twin screw pump |

# TABLE OF CONTENTS

Page

ABSTRACT ....ii

ACKNOWLEDGEMENTS .... iii

CONTRIBUTORS AND FUNDING SOURCES....iv

NOMENCLATURE....v

TABLE OF CONTENTS ....ix

LIST OF FIGURES....xi

LIST OF TABLES ....xvi

1. INTRODUCTION....1

   1.1. Overview of Oil and Gas Production ....2
   1.2. Fundamentals of Twin Screw Pumps....4
   1.3. Literature Review....9

2. OBJECTIVE....17

3. MULTIPHASE TWIN SCREW PUMP MODEL ....19

   3.1. Chamber Model....20
   3.2. Homogeneous Two-Phase Fluids....22
   3.3. Leakage Flow Model....26
      3.3.1. Two-Phase Compressible Flow....26
      3.3.2. Circumferential Clearance....33
      3.3.3. Flank Clearance....37
      3.3.4. Root Clearance ....38
      3.3.5. Couette Flow ....41
      3.3.6. Eccentricity Effects on the Circumferential Leakage Flow ....43
   3.4. Structure of the Computational Model....46

4. RESULTS AND DISCUSSION ....49

   4.1. Model Validation....50
      4.1.1. Statistical Overview ....50
      4.1.2. Validation....52

Page

4.2. Pressure Distribution along the TSP ....................59
4.3. Volumetric Efficiency Prediction....................63
  4.3.1. Effect of Differential Pressure on Performance ....................64
  4.3.2. Effect of GVF on Performance ....................69
  4.3.3. Effect of Pump Speed on Performance ....................72
  4.3.4. Effect of Suction Pressure on Performance....................75
4.4. Critical Flows ....................76
4.5. Eccentricity Effects ....................82
4.6. Circumferential, Flank, and Root Clearance Analysis....................87

5. CONCLUSION ....................92

REFERENCES....................95

APPENDIX ....................97

A.1. Volumetric Efficiency vs. Differential Pressure Graphs....................97
A.2. Mach Number Graphs ....................112
A.3. Proportion of Leakage Flow Through Each Clearance and Pressure Distributions ....................126

# LIST OF FIGURES

Page

Figure 1.1. Global energy consumption projections until the year 2040, from the U.S. Energy Information Administration, 2016 [1] ........................................... 1

Figure 1.2. Subsea application of a multiphase pumping package, from Vetter et al., 2000 [3] ........................................................................................... 3

Figure 1.3. Cutaway of a double-ended twin screw pump, from Liu, 2016 [5] ................. 5

Figure 1.4. Single-threaded spindle (left) and double-threaded spindle (right) ................. 6

Figure 1.5. Intermeshed screws of the Colfax MR-200 twin screw pump ......................... 6

Figure 1.6. Chamber volume between the screw teeth, from Patil, 2013 [6] ..................... 6

Figure 1.7. The three types of clearances in TSPs, from Räbiger, 2009 [7] ...................... 8

Figure 1.8. Pump diagram and pressure distribution across a TSP. (*a*: single-phase; *b*: two-phase), from Vetter & Wincek, 1993 [8] ............................................. 10

Figure 1.9. Liquid ring disturbed by the meshing of the screws, from Vetter et al., 2000 [3] ........................................................................................... 12

Figure 1.10. Volumetric efficiency as a function of differential pressure for varying GVFs, from Vetter et al., 2000 [3] ................................................................. 13

Figure 3.1. Diagram of the simplified circular disc model, from Liu, 2016 [5] .............. 19

Figure 3.2. Control volume of the chamber with leakage mass flow from the neighboring chambers ........................................................................ 20

Figure 3.3. Speed of sound of water/air mixtures at 100 psig, from Liu, 2016 [5] .......... 25

Figure 3.4. Control volume within a clearance .............................................................. 29

Figure 3.5. Inlet condition for a clearance control volume ............................................. 30

Figure 3.6. Correlation between the GVF at the circumferential clearance and the inlet GVF at 2000 RPM and 2900 RPM, from Räbiger, 2009 [7] ................... 31

Figure 3.7. Correlation used to estimate the GVF at the inlet to the clearance ................ 32

Figure 3.8. Profile view showing the circumferential ($\delta cc$) and radial clearances ($\delta rc$).....34

Figure 3.9. Circumferential clearance, from Muhammad, 2013 [11] .....34

Figure 3.10. Pressure and Mach distributions for subsonic Fanno flow with varying back pressures, $Pb$. Dimensionless length of 1 denotes the outlet of the channel......36

Figure 3.11. Flank clearance and a rectangular approximation of the channel.....37

Figure 3.12. Root clearance flow region, from Muhammad, 2013 [11] .....39

Figure 3.13. Domain and control volume for the root clearance flow region.....39

Figure 3.14. Pressure, velocity, and temperature distributions through the radial clearance, from Räbiger, 2009 [7] .....41

Figure 3.15. Unwrapped screw geometry for the circumferential clearance (left) and velocity profile with Couette flow (right), from Vetter et al., 2000 [3] .....42

Figure 3.16. Pressure distribution throughout the TSP chambers, from Prang & Cooper, 2004 [9].....43

Figure 3.17. Change in the circumferential clearance due to rotor deflection, from Prang & Cooper, 2004 [9] .....44

Figure 3.18. Exaggerated deflection of the screw rotor, from Muhammad 2013 [11] ....46

Figure 3.19. Computer algorithm for solving leakage flows .....48

Figure 4.1. Error distribution for volumetric efficiency.....51

Figure 4.2. Efficiency curve for 15 psi suction, 1350 RPM, and 47% GVF. Predicted points have an average error of 0.6%. .....53

Figure 4.3. Efficiency curve for 100 psi suction, 1800 RPM, and 66% GVF. Predicted points have an average error of 1.9%. .....53

Figure 4.4. Efficiency curve for 75 psi suction, 1800 RPM, and 93% GVF. Predicted points have an average error of 3.7%. This curve represents the median cases. .....54

Figure 4.5. Efficiency curve for 50 psi suction, 1350 RPM, and 90% GVF. Predicted points have an average error of 6.4%. ....55

Figure 4.6. Efficiency curve for 15 psi suction, 900 RPM, and 85% GVF. Predicted points have an average error of 10.6%. ....56

Figure 4.7. Efficiency curve for 50 psi suction, 900 RPM, and 94% GVF. Predicted points have an average error of 19.5%, which is the highest average error across all sets of cases....56

Figure 4.8. Correlation between the GVF at the circumferential clearance and the inlet GVF at 2000 RPM and 2900 RPM, from Räbiger, 2009 [7]....58

Figure 4.9. Pressure distribution for 15 psi suction pressure, 1800 RPM, 250 psi dP, and varying GVF ....59

Figure 4.10. Pressure distribution for 1350 RPM, 95% GVF, 50 psi dP, and varying suction pressure ....61

Figure 4.11. Pressure distribution for 15 psi suction pressure, 1350 RPM, 85% GVF, and varying differential pressure ....61

Figure 4.12. Pressure distribution for 15 psi suction pressure, 47% GVF, 50 psi dP, and varying pump speed ....62

Figure 4.13. Volumetric efficiency (averaged across different suction pressures) as a function of RPM, differential pressure, and GVF....64

Figure 4.14. Pump performance curve averaged across all cases ....65

Figure 4.15. Pump performance curve for 15 psi suction, 47% GVF, and varying RPM. ....66

Figure 4.16. Pump performance curve for 100 psi suction, 47% GVF, and varying RPM. ....66

Figure 4.17. Pump performance curve for 15 psi suction, 95% GVF, and varying RPM. A red star indicates that choked flow occurs in the circumferential clearance. ....67

Figure 4.18. Pump performance curve for 100 psi suction, 95% GVF, and varying RPM. ....67

Figure 4.19. Pump performance for 50 psi suction and 900 RPM at varying GVFs ....69

Figure 4.20. Pump performance for 50 psi suction and 1350 RPM at varying GVFs .....70

Figure 4.21. Pump performance for 50 psi suction and 1800 RPM at varying GVFs .....70

Figure 4.22. Pump performance for 50 psi suction and 66% GVF at varying pump speeds.....73

Figure 4.23. Pump performance for 50 psi suction and 90% GVF at varying pump speeds.....73

Figure 4.24. Pump performance for 75 psi suction and 66% GVF at varying pump speeds.....74

Figure 4.25. Pump performance for 75 psi suction and 90% GVF at varying pump speeds.....74

Figure 4.26. Pump performance for 1800 RPM and 66% GVF at varying suction pressures .....75

Figure 4.27. Pump performance for 900 RPM and 85% GVF at varying suction pressures .....76

Figure 4.28. Maximum Mach numbers reached in each clearance for 15 psi suction, 1350 RPM, and 47% GVF.....78

Figure 4.29. Pressure distribution for 15 psi suction, 1350 RPM, and 47% GVF .....78

Figure 4.30. GVF distribution for 15 psi suction, 1350 RPM, and 47% GVF.....79

Figure 4.31. Speed of Sound in the circumferential clearance for 15 psi suction, 1350 RPM, and 47% GVF.....79

Figure 4.32. Maximum Mach numbers reached in each clearance for 75 psi suction, 1800 RPM, and 90% GVF.....81

Figure 4.33. Pressure distribution for 75 psi suction, 1800 RPM, and 90% GVF .....81

Figure 4.34. Ratio of eccentricity at each clearance position for varying differential pressures .....83

Figure 4.35. Increase in circumferential leakage flowrate vs. ratio of eccentricity .....83

Figure 4.36. Increase in circumferential leakage flowrate vs. axial direction for 300 psi differential pressure.....84

Page

Figure 4.37. Effects of eccentricity on performance curves for 15 psi suction pressure and 47% GVF ........ 85

Figure 4.38. Effects of eccentricity on performance curves for 15 psi suction pressure and 95% GVF ........ 85

Figure 4.39. Effects of eccentricity on performance curves for 100 psi suction pressure and 47% GVF ........ 86

Figure 4.40. Effects of eccentricity on performance curves for 100 psi suction pressure and 95% GVF ........ 86

Figure 4.41. Proportion of leakage through each clearance for 15 psi suction, 900 RPM, 66% GVF, and 248 psi dP ........ 89

Figure 4.42. Proportion of leakage through each clearance for 15 psi suction, 1350 RPM, 85% GVF, and 53 psi dP ........ 89

Figure 4.43. Proportion of leakage through each clearance for 15 psi suction, 1800 RPM, 93% GVF, and 50 psi dP ........ 90

# LIST OF TABLES

Page

Table 3.1. Correlation used to estimate the GVF at the inlet to the clearance.................32

Table 4.1. Test matrix for the Colfax MR-200 TSP........................................................49

Table 4.2. Correlation between error from the model and the input parameters .............52

# 1. INTRODUCTION

Today, oil and gas are the most dominant energy sources in the world. Petroleum and other liquid fuels account for one-third of the global energy consumption, while natural gas accounts for one-quarter, as shown in Figure 1.1. Collectively, oil and gas supply more than half of the world's energy needs. Even though there are increased efforts to rely more on alternative energy through initiatives like the United States Clean Power Plan, petroleum consumption will continue to grow over the next 20 years in order to meet global energy needs. Further advancements in research and engineering within the industry are critical in extending the lifecycles of reservoirs and improving oil recovery techniques.

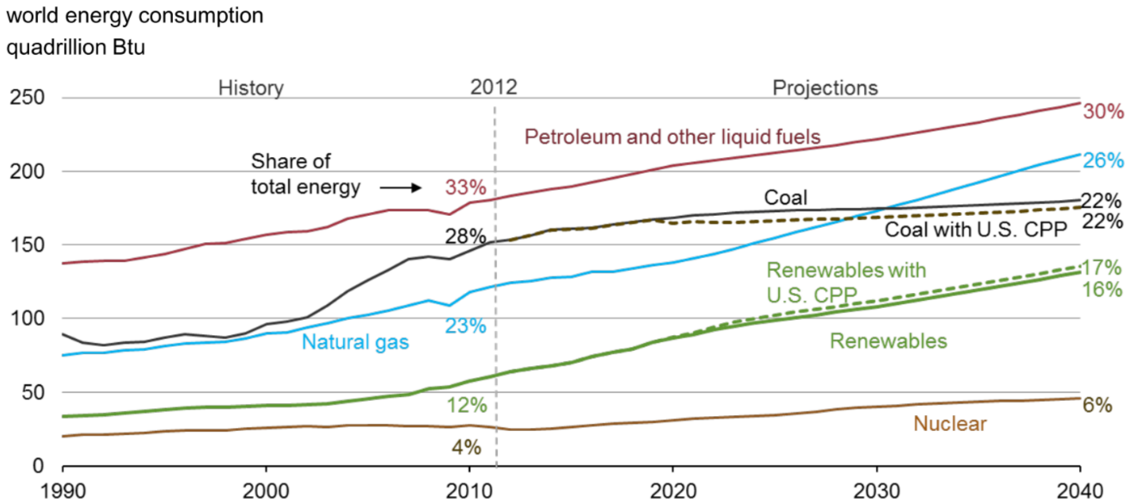

**Figure 1.1.** Global energy consumption projections until the year 2040, from the U.S. Energy Information Administration, 2016 [1]

## 1.1. Overview of Oil and Gas Production

An oil reservoir's lifecycle is commonly divided into primary, secondary, and tertiary stages. Throughout its life, a reservoir's production decreases. Water or gas injections may be used to stimulate production, but eventually wells cease to be economically feasible and are sealed. Reservoir conditions vary greatly through changes in pressure and in the mixtures of water, oil, gas, and sand. It is important that operators be able to use equipment that can adapt to a wide range of conditions. The vast majority of reservoirs do not contain sufficient pressure to produce oil on its own, and so operators need to use methods of artificial lift to drive the oil to the surface. This can be in the form of gas lift, which is a process of injecting gas into the well to raise the pressure of the reservoir and lower the viscosity of the fluid, or pumping systems used within the well.

Once a mixture of oil, gas, and water has been produced at the wellhead, it may also be necessary to use a multiphase pumping system to move the mixture to a distant processing site for fluid separation and storage or transport. In a sense, this multiphase boosting serves two purposes: to transport the oil and gas to a production center and to reduce the wellhead back pressure so that artificial lift methods may work more effectively. In particular, multiphase pumping systems are important for tying in a remote well to an existing production center and, similarly, for subsea operations. In offshore applications, the use of multiphase boosting allow operators to establish wells at greater depths and at distances farther from a central production platform. This allows production from fields that may otherwise not be economically feasible. An example of a subsea system setup is shown in Figure 1.2.

There are many challenges that the oil industry faces to produce oil effectively. A critical aspect is the pumping systems. For artificial lift, one common system is the electrical submersible pump (ESP). This is composed of a stack of centrifugal pump stages that operate within the wellbore. They are efficient and can handle high flow rates, but, by themselves, many designs cannot handle fluids with very high gas volume fractions (GVFs) effectively. At high GVFs, ESPs are susceptible to phenomena, such as surging and gas locking, which drastically reduces fluid flow [2]. For older wells and those with high gas content, ESP systems may require additional components, such as a gas separator, and separate oil and gas pipelines.

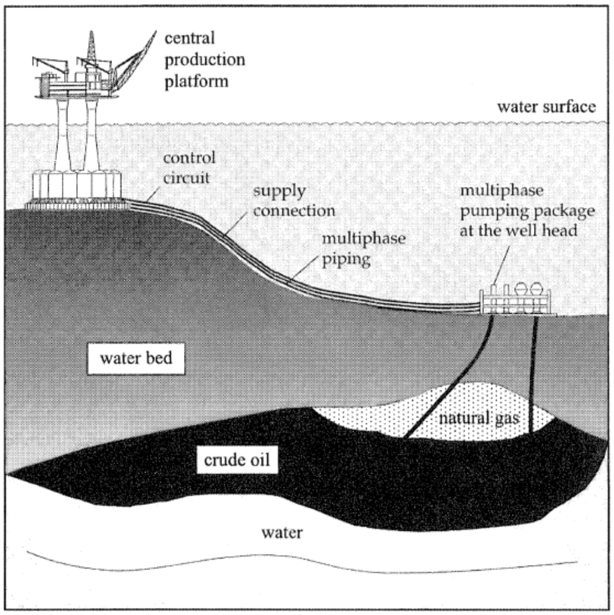
central
production
platform
water surface
control
circuit
supply
connection
multiphase
pumping package
at the well head
multiphase
piping
water bed
natural gas
crude oil
water

**Figure 1.2.** Subsea application of a multiphase pumping package, from Vetter et al., 2000 [3]

Twin screw pumps (TSPs) are a type of positive displacement pump that can handle gas volume fractions ranging anywhere from 0-100%. Due to their ability to pump multiphase flow, they are a good alternative to conventional pumping systems that would require additional equipment for phase separation. Compared to a conventional system, a multiphase system can have 30% lower investment costs, 15% increased production, and a 50% smaller footprint [4]. Although TSPs are more commonly used for multiphase boosting either onshore or on the seabed, there are also electrical submersible twin screw pumps that are designed to operate within the oil well casing. Due to their wide operating envelope, TSPs are a valuable option for operators at production sites.

## 1.2. Fundamentals of Twin Screw Pumps

TSPs are comprised of two screws that mesh together to form isolated chambers between the screw threads. As the screws rotate in counter directions, the chambers travel from the suction side to the discharge side. Figure 1.3 shows a double-ended TSP with suction on the outer sides and discharge in the middle. In this diagram, the upper spindle is connected to a motor (not pictured), which then drives the other spindle via timing gears.

There are a few varieties of twin screw pumps. TSPs can be single-ended, with suction on one side and discharge on the other, or they can be double-ended, with suction inlets at both ends and a discharge outlet at the center of the spindles. Double-

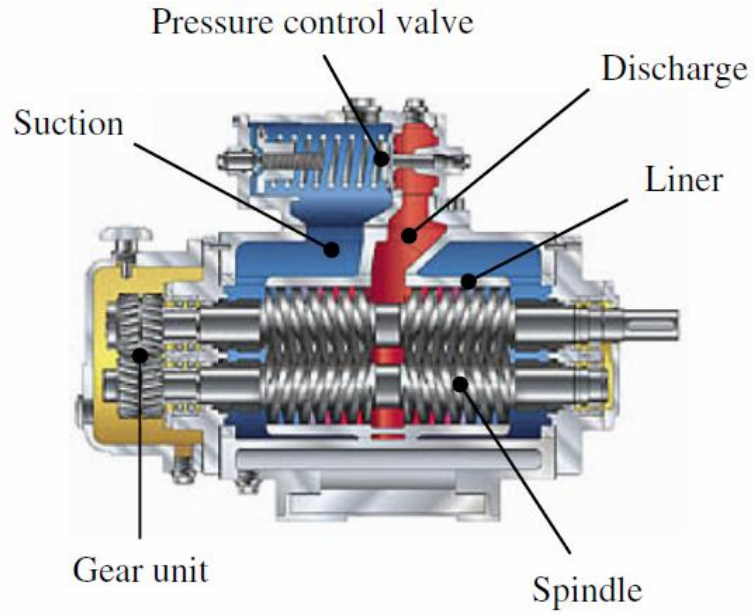

**Figure 1.3.** Cutaway of a double-ended twin screw pump, from Liu, 2016 [5]

ended TSPs are more common, and the symmetry is used to balance the axial load. TSP spindles can also be single-threaded or double-threaded as shown in Figure 1.4. In this study, the focus is on double-ended and single-threaded TSPs. Key features of the screw are shown in Figure 1.5. The suction side is on the left, and the discharge is on the right. In this diagram, there are seven teeth and eight chambers separated by the teeth. The leftmost chamber is open to suction, there are six isolated chambers in the middle, and the rightmost chamber is open to the discharge. The volume of each chamber is shown in Figure 1.6.

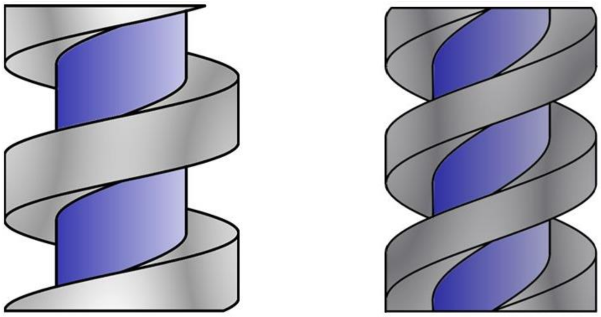

**Figure 1.4.** Single-threaded spindle (left) and double-threaded spindle (right)

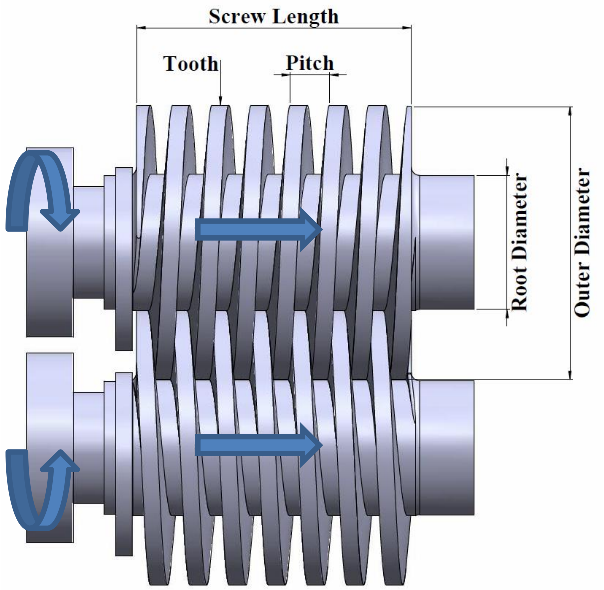
Screw Length
Tooth
Pitch
Root Diameter
Outer Diameter

**Figure 1.5.** Intermeshed screws of the Colfax MR-200 twin screw pump

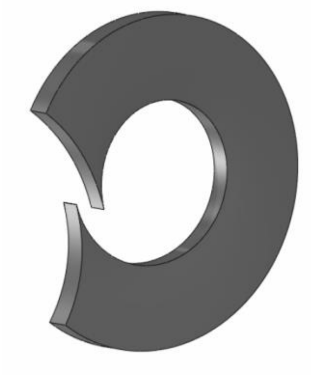

**Figure 1.6.** Chamber volume between the screw teeth, from Patil, 2013 [6]

TSPs fundamentally operate differently than centrifugal pumps.  The rotational speed dictates the flowrate and how quickly the chambers travel from suction to discharge.  Whereas, the pressure head is dictated by the back pressure.  While the bulk of the fluid is conveyed from the inlet to the outlet, there is leakage flow through clearances in the reverse direction.  The clearances exist in order to prevent metal-to-metal contact during operation.  The volumetric efficiency is the actual net flow divided by the ideal flow without any clearances, as shown in Equation (1.1),

$$\eta_v \equiv \frac{Q_{actual}}{Q_{th}} = \frac{Q_{th} - Q_{lkg}}{Q_{th}} \tag{1.1}$$

where $Q_{th}$ is the theoretical flowrate and $Q_{lkg}$ is the leakage flowrate.

The theoretical flowrate, $Q_{th}$, can be calculated from the geometry alone.  For a pair of screws, every revolution would displace a total of two chambers.  Thus $Q_{th}$ can be easily calculated given the chamber volume and the pump speed.  The theoretical flowrate is then used to calculate the volumetric efficiency as given in Equation (1.1).  While leakage occurs between every consecutive pair of chambers, only the leakage rate from the first isolated chamber back to the suction is needed to calculate the volumetric efficiency.

There are three main types of clearances: circumferential clearance, flank clearance, and radial (or sometimes called root) clearance.  These types are shown in Figure 1.7.  The circumferential clearance (CC) is the gap between the housing and the outer diameters of the meshed screws.  The flank clearance (FC) is the gap between the flanks of the interacting screw profiles.  The radial clearance (RC) is the gap between the

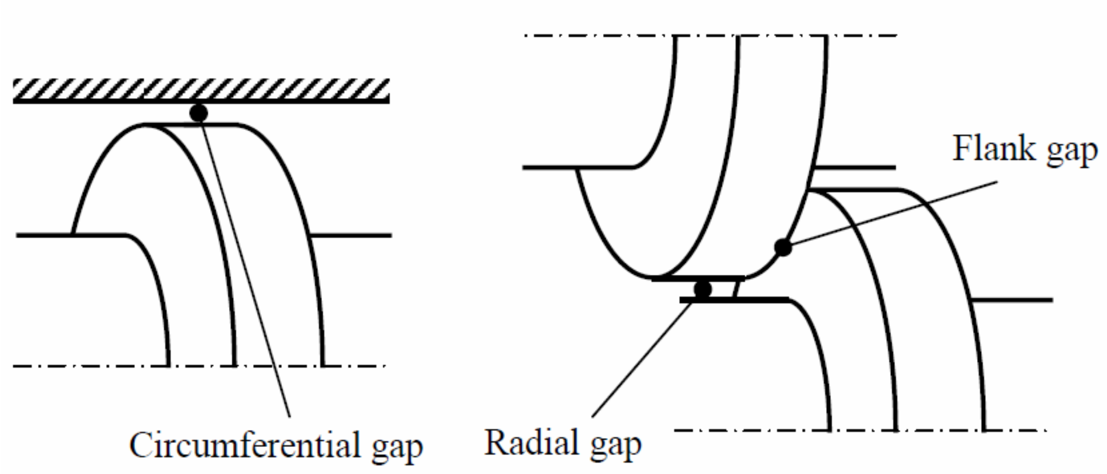

**Figure 1.7.** The three types of clearances in TSPs, from Räbiger, 2009 [7]

inner shaft of one screw and the outer diameter of the other. In order to improve the performance of these pumps, it is important to study the leakages and to be able to understand all of the factors that influence the losses.

The pump effectiveness, $\eta_{eff}$, describes the pump's ability to deliver power to a compressible fluid relative to an incompressible fluid. In general, the pump effectiveness decreases when the GVF or compressibility of the fluid increases. It is defined as

$$\eta_{eff} = \frac{P_{net}}{P_{hydraulic}} \tag{1.2}$$

where $P_{net}$ is the net power delivered to the fluid and $P_{hydraulic}$ is the hydraulic power if the fluid were incompressible.

The mechanical efficiency, $\eta_{mech}$, represents the total frictional and mechanical losses. Sources of these losses are viscous effects and friction from the bearings, seals, and gears. The mechanical efficiency is defined as

$$\eta_{mech} = \frac{P_{net}}{P_{drive}} \tag{1.3}$$

where $P_{drive}$ is the total electrical power supplied to the motor to run the pump. In this study, the volumetric efficiency remains the key metric for evaluating the performance of TSPs.

## 1.3. Literature Review

There has been much research and performance modeling on twin screw pumps over the past two decades. Leakage flow analysis is a particularly important topic due to its direct impact on efficiency. The leakage rate is affected by factors such as the gas volume fraction, differential pressure across the pump, and viscosity. Due to the complicated nature of multiphase flow, the effect of GVF on TSP performance has been difficult to model accurately. For flows ranging from pure liquid (0% GVF) to pure gas (100% GVF), the qualitative behavior can vary significantly. On the other hand, models for purely liquid flows have generally been more reliable. In this section, a survey of the current state of research on twin screw pumps is presented.

In 1993, Vetter and Wincek [8] developed a computational model of TSPs for single-phase and two-phase operation. A key assumption in the two-phase model was that the flow through the clearances is entirely liquid, despite the fact that the chambers contain a mixture of liquid and gas. This assumption is made for simplicity, yet it is still reasonable because centrifugal forces from the high speed rotation cause the denser liquid phase to be dominant in the clearances. The model incorporates explicit calculations for each of the three clearances. In general, the leakage flow is calculated based on the sum effect of the pressure difference between chambers and the rotational component from the spindles. Another factor that was considered is that the pressure gradients throughout the pump bend the rotor slightly. The deflection causes eccentric rotation about the axis, which increases the cross-sectional area of the circumferential clearance. Vetter and Wincek account for this by using a correction factor.

For two-phase flow, the pressure difference across each circumferential clearance is larger closer to the discharge end. A simplified diagram of the pressure distribution is shown in Figure 1.8. The pressure is uniform within each chamber and rises linearly through each clearance. For single-phase flow, the pressure differentials and mass flow rates for each of the clearances are the same. However for the two-phase flow model,

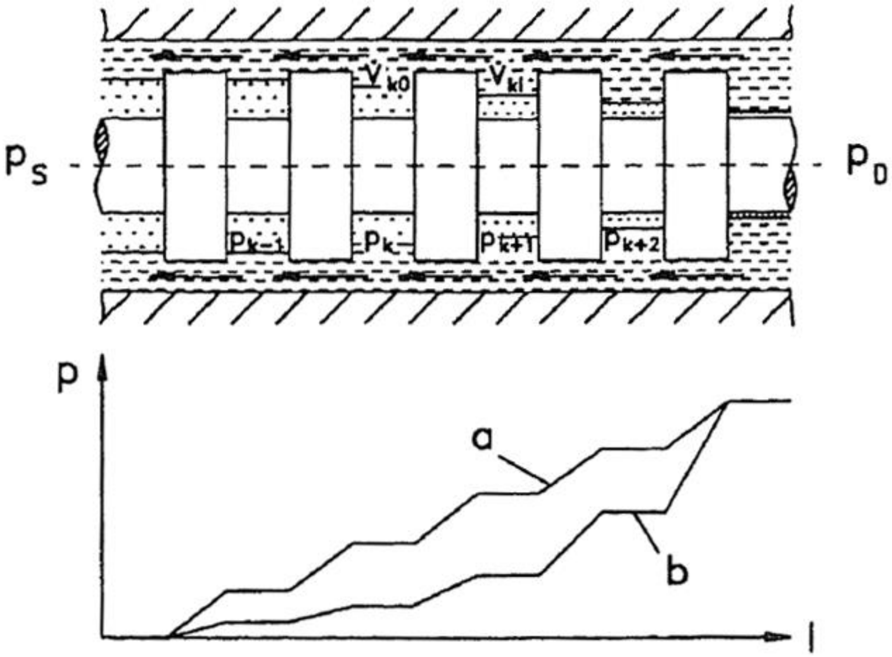

**Figure 1.8.** Pump diagram and pressure distribution across a TSP.
(*a*: single-phase; *b*: two-phase), from Vetter & Wincek, 1993 [8]

gas compression in the chambers occurs due to the accumulation of liquid from the leakages. In each chamber, there is more leakage into the chamber than out of it. Consequently, as the chambers travel from suction to discharge, the GVF decreases, and the pressure rises more quickly.

Vetter and Wincek validated their model using experimental tests. The model used for one-phase flow matches the experimental data. The model used for two-phase flow showed larger deviations for GVFs above 50% and also for lower speeds. A likely explanation is that the assumption that the leakage flow is purely liquid is not appropriate for higher GVFs. An important finding was that 80% of the total leakage passed through the circumferential clearances, 15% passed through the radial clearances, and 5% passed through the flank clearances.

In 2000, Vetter et al. [3] expanded on the previous model and also discussed the effects of hydroabrasive wear. They relaxed the assumption that the leakage flow is entirely liquid. They state that below 85% GVF, the assumption seems valid. Figure 1.9 shows an illustration of a liquid ring—created by centrifugal forces—that could completely fill the clearances with liquid. However above 85% GVF, the liquid and gas phases likely become a quasihomogeneous foam. The high GVF mixture is modeled as a weighted average of the two phases. It is also noted that due to the intensive mixing and high specific heat capacity of the liquid compared to that of the gas, the gas compression is nearly isothermal.

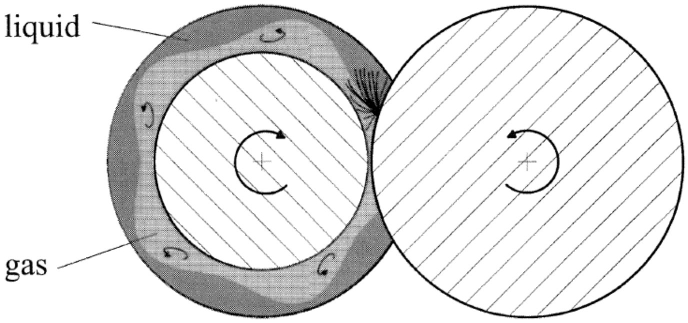

**Figure 1.9.** Liquid ring disturbed by the meshing of the screws, from Vetter et al., 2000 [3]

The paper further discusses experimental results for a series of tests at varying gas volume fractions. As seen in Figure 1.10, the volumetric efficiency remained relatively high for large pressure rises if the GVF was below 95%. At GVFs above 95%, the volumetric efficiency quickly drops if the pressure rise is too large. This is because liquid can seal the clearances much better than gas. The experimental results also showed that the pressure distribution would go from linear to concave up as the GVF increased from 0% to 80%. This is consistent with Figure 1.8. However for even higher GVFs, the pressure distribution tended to be more linear again. This behavior indicates that above 80% GVF, the fluid behaves as homogenous rather than as discrete gas-liquid phases.

Prang and Cooper [9] developed a model based on the previous two models. The two assumptions made are that the leakage flow is only liquid and that the total leakage can be calculated as the circumferential leakage increased by some factor. Based on Vetter and Wincek's [8] study, 80% of the leakage goes through the circumferential clearance. However, Prang and Cooper note that viscosity affects the ratio because of

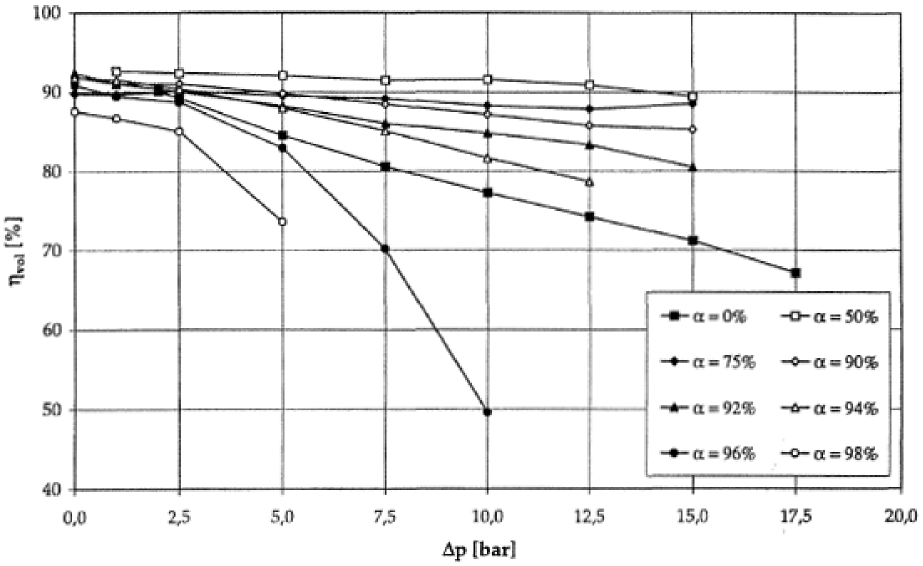

**Figure 1.10.** Volumetric efficiency as a function of differential pressure for varying GVFs, from Vetter et al., 2000 [3]

the differences in the clearance geometries. The leakage flow velocity is calculated as flow through a pipe with friction:

$$V_{lkg} = \sqrt{\frac{2\Delta P}{\rho_L\left(k_e + f\,\frac{l}{D_h}\right)}} \tag{1.4}$$

where $\rho_L$ is the density of the liquid, $k_e$ is a loss coefficient at the clearance entrance and $f$ is the friction factor. The radial force on the rotor, which causes eccentric rotation is calculated as follows:

$$F_r = h(D_i + D_o)\Delta P \tag{1.5}$$

where $h$ is the screw pitch, $D_i$ is the inner diameter of the spindle, $D_o$ is the outer diameter, and $\Delta P$ is the pressure rise across the entire pump.

The model was validated using experimental tests. It predicted single-phase flow with both low and high viscosities very well. The computational results were greatly affected by the clearance size, which was expected. It was found that decreasing the viscosity can also decrease the performance for TSPs because there could be greater leakage flow through the clearances. This behavior may be counterintuitive because decreasing viscosity decreases viscous losses. The model was also tested at 58%, 86%, and 93% GVF for a water/air mixture. The model shows good agreement with the experimental results for all cases. For the 93% GVF case compared to the others, the intake volume flow rate remains relatively constant as the differential pressure rises. This is explained by the fact that as GVF rises, most of the pressure rise occurs across the last clearance. Conversely, there is very little pressure rise across the first clearance. Thus there is little leakage from the chambers of the TSP back to the suction.

Nakashima et al. [10] developed a thermo-hydraulic model with a greater emphasis on the effect of tangential velocity on the circumferential leakage flow. With previous models, the friction factor was calculated based on the average axial velocity. Previously, there have been general studies on axial flow in an annular channel, in which the inner concentric cylinder rotates. Fundamentally, this flow is the same as circumferential leakage flow for TSPs. The general finding is that high rotation speed leads to regimes where the axial velocity is dependent on the tangential velocity. For example after a certain critical Reynolds number, Taylor vortices form around the circumference of the cylinder due to centrifugal forces. These vortices directly interfere with the axial component of the flow. To account for this, the model calculates the friction factor based on correlations for this type of flow.

Muhammed [11] developed a hydrodynamic model in order to study the rotordynamics of TSPs. The model calculates the velocity and pressure distributions across the circumferential and radial clearances but not for the flank clearances since it has negligible impact on the rotordynamics. The model assumes that the flow through the clearances is entirely liquid. For the radial clearance, the flow was modeled based on Hirs' bulk flow theory [12]. The bulk flow velocity through the clearance is calculated using the momentum equation from Reynolds transport theorem. The shear stress is calculated using the bulk flow velocity relative to the rotating spindles rather than the absolute velocity. The friction factor is calculated from the Blasius friction model.

Liu [5] developed a multiphase TSP model that does not assume that the clearances are filled with only liquid. Removing this assumption complicates the model because a mixture of liquid and gas has a sonic speed much lower than that of either pure liquid or pure gas. The sonic speed of the mixture can be in the order of 60 meters per second, and it is possible that the leakage flow will choke within the gaps if it reaches the speed of sound. The model incorporates Fanno flow, which is applicable to compressible flow through a channel with friction. The model assumes homogeneous flow, where the fluid is treated as a uniform phase without any slip between the bubbles and the liquid phase. Only flow through the circumferential clearance is calculated, and the total leakage is extrapolated based on Vetter and Wincek's [8] finding that the circumferential clearance leakage accounted for 80% of the total leakage. Further, the model does not factor in eccentric rotation, which would lead to greater leakages through the circumferential clearance. The model was validated using experimental data from a few different pumps. The changes in test parameters were GVF, pressure rise, inlet suction pressure, and RPM. Overall, the model showed good agreement with the experimental results for gas volume fractions ranging from 50-100% and for differential pressures ranging from 50-300 psi.

# 2. OBJECTIVE

Multiphase TSPs are a simple and cost-effective pump system to implement for multiphase boosting. They are one of the most commonly used multiphase pumps within the oil & gas industry. Understanding the performance of TSPs under a wide range of operating conditions is essential to improving their design and efficiency during operation in the field. In previous research, it has been difficult to model varying GVF and multiphase flow effectively. Most models do not account for compressibility effects of two phase leakage flows and the possibility of choked flow within the clearances. Instead, leakage fluid is often treated as entirely liquid or as an incompressible homogeneous fluid.

The objective of this study is to develop a more robust model to predict the performance of TSPs during multiphase operation. A key improvement in the present model is the incorporation of two-phase compressible flow and critical conditions. Additionally, the leakage through the flank and root clearances are explicitly calculated unlike in previous models that calculate the total leakage from the circumferential clearance and multiply by an assumed factor. Due to the fundamental differences in each of clearances, changes in GVF and pressure distribution can affect the proportion of leakages going through each clearance. Increases in leakage flowrates due to eccentric rotation are also taken into account.

TSPs often encounter a wide range of inlet conditions as the fluid properties vary drastically over the life of an oil field. The present model is used to investigate how changes in the GVF, pump speed, differential pressure, and suction pressure affect the performance of TSPs.  The volumetric efficiency is a key metric used to evaluate the TSP, but, additionally, the proportion of leakage through each of the clearances, the pressure and velocity distributions, and the presence of critical flows are all explored in this study.  The model is also validated against experimental data from a Colfax MR-200 multiphase TSP running water and air in a study by Patil [6].

# 3. MULTIPHASE TWIN SCREW PUMP MODEL

This section discusses the development of the twin screw pump model. It is based on thermodynamic and fluid dynamic theory. As with any model, there are some simplifying assumptions. The model is based off of the circular disc model originally proposed by Vetter and Wincek [8] and later expanded upon by Liu [5]. The chambers are treated as circular discs that move axially from suction to discharge and that are connected via the clearances as shown in Figure 3.1. Due to high rotational speed and intensive mixing, the two-phase flow is treated as a homogeneous average of the gas and liquid phases. The gas, which is air in this study, is treated as an ideal gas. The system as a whole is assumed to be adiabatic with no heat transfer between the fluid and any of the metal parts.

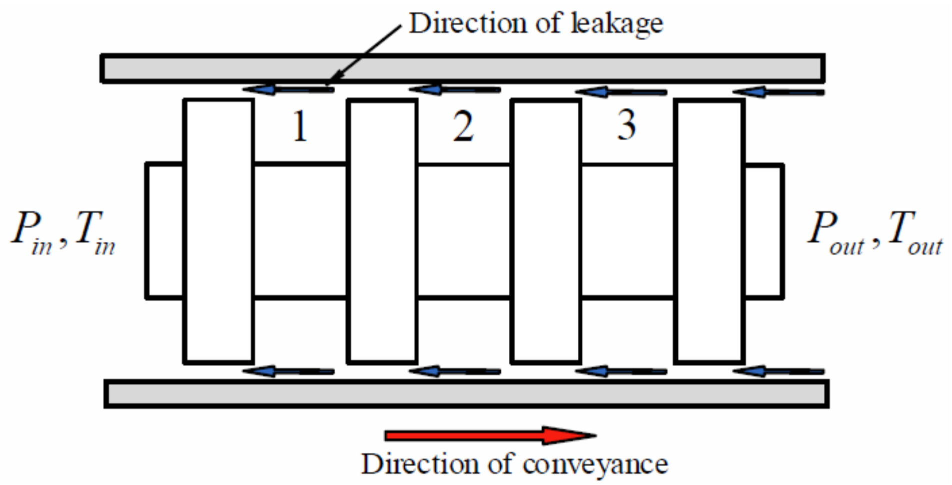

**Figure 3.1.** Diagram of the simplified circular disc model, from Liu, 2016 [5]

### 3.1. Chamber Model

The chambers in this model are treated as open, transient, and stagnant thermodynamic control volumes (CVs). These control volumes are open to mass flow via the clearances as shown in Figure 3.2. As the CVs are conveyed from suction to discharge, they start at a given position, $i$, and after one revolution, they travel to the next position, $i+1$. Also after one revolution, a chamber is created at the suction end, and a chamber disappears at the discharge end. To account for the change in properties as a chamber travels from $i$ to $i+1$, the model discretizes each revolution into small time steps. The lifetime of a chamber is defined as the time it takes to complete one revolution:

$$\Delta t_{life} = \frac{60}{N} \tag{3.1}$$

where $N$ is the pump speed in RPM.

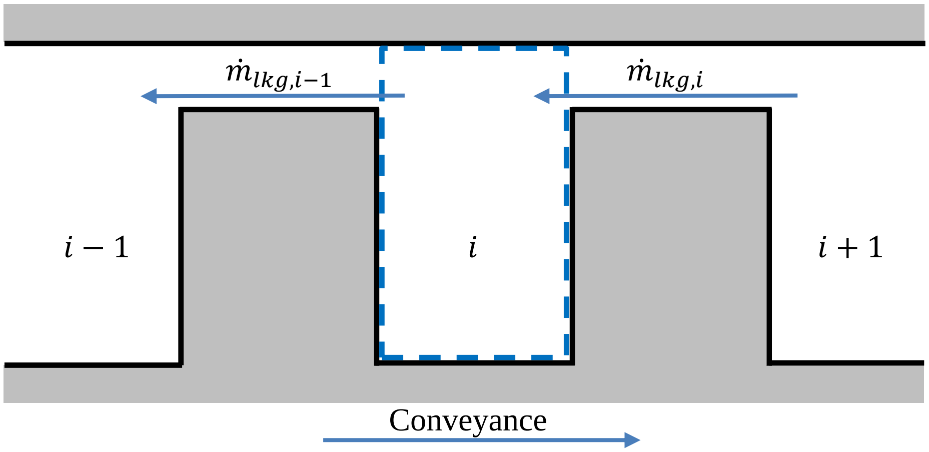

**Figure 3.2.** Control volume of the chamber with leakage mass flow from the neighboring chambers

The model is setup such that at $t = 0$, a chamber is formed with the same thermodynamic state as the suction. At every time step, $dt$, the states of each CV are re-calculated according to the mass exchange between the chambers. Once $t = \Delta t_{life}$, a complete revolution has occurred, and the process is started over again. The last chamber disappears, a new chamber is created at the suction, and the state of every chamber $i$ then becomes the new state for the chamber $i + 1$.

The properties of each chamber are calculated from mass and energy balances. The following conditions are assumed when analyzing the chambers:

- The CVs are adiabatic
- The properties of the CV are constant and uniform at any given time step
- Kinetic energy and viscous effects within the chamber are ignored

In essence, the chambers are treated as stagnant with mass flow in and out.

The mass balance is split into liquid and gas, and it simply states that the change in mass of the CV is equal to the net mass flow in. The equations are the following:

$$\frac{dm_{L,CV}}{dt} = \frac{dm_{L,in}}{dt} - \frac{dm_{L,out}}{dt} \tag{3.2}$$

$$\frac{dm_{G,CV}}{dt} = \frac{dm_{G,in}}{dt} - \frac{dm_{G,out}}{dt} \tag{3.3}$$

The following transient energy equation states that the change in energy of the CV is equal to the net energy flow in. After simplifying assumptions, the equation is

$$\frac{dU_{CV}}{dt} = \left(\frac{dm_{L,in}}{dt} \cdot h_{L,in} + \frac{dm_{G,in}}{dt} \cdot h_{G,in}\right) - \left(\frac{dm_{L,out}}{dt} \cdot h_{L,out} + \frac{dm_{G,out}}{dt} \cdot h_{G,out}\right) \tag{3.4}$$

The mass flow rates and the properties of the fluid entering and leaving the CV are known, based on the fluid model that is discussed in a later section. The gas mass fraction or quality ($x$), as well as the density, can be determined from the mass balance in Equations (3.2) and (3.3). From Equation (3.4), the change in energy and subsequently the temperature of the CV can be calculated. Finally, the ideal gas law in Equation (3.5) is used to calculate the pressure.

$$P = \rho_G RT \tag{3.5}$$

## 3.2. Homogeneous Two-Phase Fluids

Homogeneous flow can be described as flow with no relative motion between the phases. This would occur if the bubble size is small enough and the fluid is mixed sufficiently such that all phases move at the same velocity and there is no interaction between the phase interfaces. The mixture of the phases can be represented as either the gas volume fraction or the quality. The GVF is more commonly used within the oil & gas industry, but the quality is generally more appropriate for calculations. The definitions of GVF ($\alpha$) and quality ($x$) are given in Equations (3.6) and (3.7).

$$\alpha \equiv \frac{V_G}{V_{mix}} \tag{3.6}$$

$$x \equiv \frac{m_G}{m_{mix}} \tag{3.7}$$

The GVF and quality can be converted given the densities of the two phases, as shown in Equations (3.8) and (3.9).

$$\alpha = \frac{x\rho_L}{x\rho_L + (1-x)\rho_G} \tag{3.8}$$

$$x = \frac{\alpha\rho_G}{\alpha\rho_G + (1-\alpha)\rho_L} \tag{3.9}$$

The properties of the homogeneous fluid are calculated as a weighted average of the properties of the phases. Pressure and temperature for the mixture is the same as for the individual phases, but other important properties are the density, viscosity, specific heats, and ratio of specific heats. These properties can be calculated according to Equations (3.10), (3.11), (3.12), (3.13), and (3.14).

$$\rho_{mix} = \alpha\rho_G + (1-\alpha)\rho_L \tag{3.10}$$

$$\mu_{mix} = \alpha\mu_G + (1-\alpha)\mu_L \tag{3.11}$$

$$c_{v,mix} = xc_{v,G} + (1-x)c_{v,L} \tag{3.12}$$

$$c_{p,mix} = xc_{p,G} + (1-x)c_{p,L} \tag{3.13}$$

$$\gamma_{mix} = \frac{c_{p,mix}}{c_{v,mix}} \tag{3.14}$$

Note that the ratio of specific heats for a mixture is not calculated as a weighted average of the ratios for the two phases.

These physical properties depend on temperature. Although the temperature rise throughout a TSP is generally not very large, the model recalculates the properties at every time step using various correlations. For density, the liquid is assumed to be incompressible, and the density for air is calculated from the ideal gas law in Equation (3.5). The viscosity for water is calculated from the Vogel equation,

$$\mu_{water} = e^{-3.7188+\frac{578.919}{T-137.546}} \tag{3.15}$$

where $T$ ranges from 273K to 373K. The viscosity for air is calculated from the Sutherland's formula,

$$\mu_{air} = \mu_0 \frac{a}{b}\left(\frac{T}{T_0}\right)^{1.5} \tag{3.16}$$

where $a$, $b$, $\mu_0$, and $T_0$ are constants. The specific heats for air are calculated using the following two equations:

$$c_{v,air} = 0.716 + (5 \times 10^5)(T - 250) \tag{3.17}$$

$$c_{p,air} = c_{v,air} + R \tag{3.18}$$

where $R = 0.2869$ KJ/kg·K is the specific gas constant for air. The specific heats for water are roughly constant for the range of temperatures to which the TSP is exposed.

Another important aspect of two-phase fluids is the low speed of sound. The speed of sound of a water/air mixture is much lower than the speed of sound of either pure water or pure air as shown in Figure 3.3. This plays an important role in two-phase compressible flow because within a duct, the flow will become choked if the velocity reaches the speed of sound. Once the flow chokes, the mass flowrate cannot increase any further, regardless of the pressure gradient pushing the fluid. As is discussed in the following Section 3.3.1, choking can be caused by friction, change in cross-sectional area, or heat input.

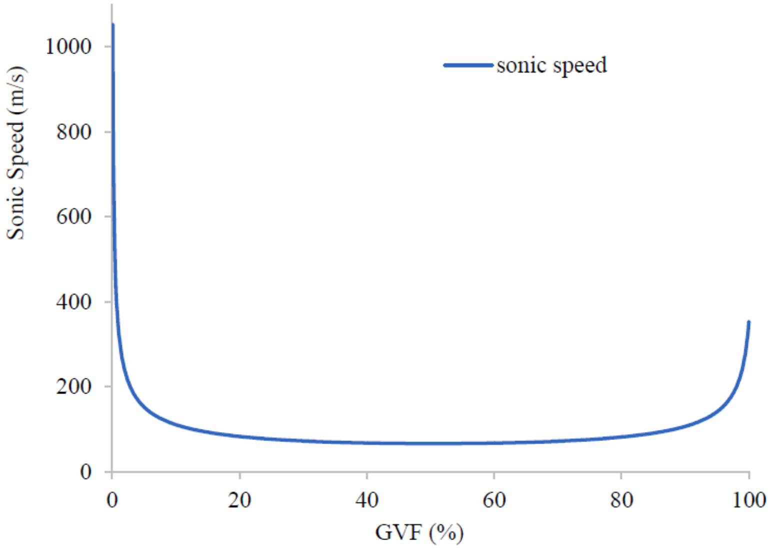

**Figure 3.3.** Speed of sound of water/air mixtures at 100 psig, from Liu, 2016 [5]

The speed of sound of a gas/liquid mixture is given by Brennen [13],

$$\frac{1}{c_{mix}^2} = [\rho_L(1-\alpha) + \rho_G\alpha]\left[\frac{\alpha}{kP} + \frac{1-\alpha}{\rho_L c_L^2}\right] \tag{3.19}$$

where $k$ is the polytropic coefficient and $c_L$ is the speed of sound of the liquid. Equation (3.19) assumes that there is no surface tension, which is true when $P = P_G = P_L$, and that the gas is perfect and behaves polytropically with the relationship $\rho_G^k \propto P$. In contrast, the speed of sound for an ideal gas is given by the following equation:

$$c_{IG} = \sqrt{\gamma RT} \tag{3.20}$$

In Equation (3.19), the $(1-\alpha)/\rho_L c_L^2$ term is related to the compressibility of the liquid phase. In most cases, especially when $\alpha$ is not too small, this term can be neglected.

## 3.3. Leakage Flow Model

The model for the flows through each the circumferential, flank, and root clearances share similarities. The leakage is treated as steady flow through a 1-D channel connecting two reservoirs. There are two components to the flow: pressure-driven flow and flow due to the movement of the walls. The pressure-driven flow is calculated as if the walls were static, and the flow is solved as a 1-D compressible flow problem. The movement of the walls contributes to the leakage as well, and this component is modeled as Couette flow. In Couette flow, there is no pressure gradient, and all flow is caused by shear stress with the moving walls. The total leakage flow is then simply a sum of the pressure-driven flow and the Couette flow.

This section discusses the development of the compressible flow model. Choked flow is a possibility that will occur at higher velocities. The geometries of each of the clearances differ, and those leakage flows are individually discussed in later subsections. The contribution of Couette flow is discussed in Section 0, and the increased leakage rate due to rotor deflection is discussed in Section 3.3.6

### *3.3.1. Two-Phase Compressible Flow*

The flow through the 1-D clearances are calculated based on a generalized form of compressible flow equations. For subsonic flow through a channel, the velocity can be increased through a decrease in area, an increase in friction, or an increase in heat transfer. Specifically, compressible flow through a constant area channel with friction is termed Fanno flow, and flow through a frictionless channel with heat transfer is termed

Rayleigh flow. In gas dynamics, equations for these flows have been developed from the continuity, momentum, and energy equations. Rather than velocity, the flows are more conveniently described using the Mach number, which is defined as the ratio of velocity to the speed of sound,

$$M \equiv \frac{V}{c} \tag{3.21}$$

The generalized form of the compressible flow equations given by Young [14] can be used to calculate the change in Mach number given the cross-sectional area, friction, heat transfer, and mass injection in the channel. The present model neglects heat transfer, and mass injections through the channel walls are irrelevant. The simplified form of the governing equation used in the model is the following:

$$\frac{dM^2}{M^2} = -\left[\frac{2 + (\gamma - 1)M^2}{1 - M^2}\right]\frac{dA_c}{A_c} + \left[\frac{\gamma M^2\left(1 + \frac{\gamma - 1}{2}M^2\right)}{1 - M^2}\right]\left(\frac{f\,dx}{D_h}\right) \tag{3.22}$$

where $\gamma$ is the ratio of specific heats, $A_c$ is the cross-sectional area, $f$ is the friction factor, and $D_h$ is the hydraulic diameter. On the right hand side of the equation, the first term represents the effect of changing cross-sectional area, and the second term represents the effect of friction.

Within the clearances, friction causes a stagnation pressure drop, entropy generation, but an increase in velocity. The friction factor used in Equation (3.22) is a ratio of the wall shear stress to the kinetic energy as described in the following equation [15],

$$f = \frac{8\tau_w}{\rho V^2} \tag{3.23}$$

There are many models to estimate the friction factor empirically. Most of them depend on the Reynolds number,

$$\mathrm{Re} = \frac{\rho V D_h}{\mu} \tag{3.24}$$

The hydraulic diameter is defined as,

$$D_h = \frac{4A_c}{\text{Perimeter}} \tag{3.25}$$

For laminar flow with $\mathrm{Re} < 2300$, the friction factor is estimated as,

$$f = \frac{64}{\mathrm{Re}} \tag{3.26}$$

For turbulent flow, the friction factor is estimated using the Blasius friction factor correlation:

$$f = 0.361\mathrm{Re}^{-0.25} \tag{3.27}$$

Along the clearances, the domain is discretized into many control volumes, as shown in Figure 3.4. Equation (3.22) gives the change in Mach number with every step, $dx$, and with the change in cross-sectional area. Based on the Mach number, the change in pressure and temperature can also be determined from the following equations [5],

$$\frac{dT}{T} = -\frac{(\gamma - 1)MdM}{1 + \frac{\gamma - 1}{2}M^2} \tag{3.28}$$

$$\frac{dP}{P} = -\frac{dM}{M} + \frac{1}{2}\frac{dT}{T} \tag{3.29}$$

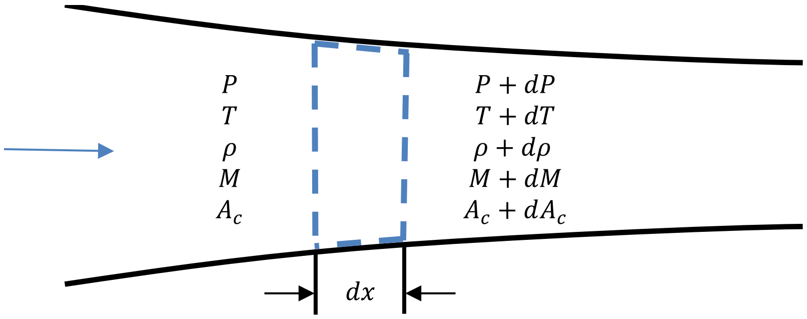

**Figure 3.4.** Control volume within a clearance

It is assumed that the gas mass fraction is constant throughout the entire channel. Thus after calculating the Mach number, pressure, and temperature, all of the property values for the gas and liquid phases, such as density and viscosity, can be calculated using the equations from Section 3.2. While the gas mass fraction is constant, the gas volume fraction will change as the pressure changes. As shown in Equation (3.19), the speed of sound is dependent on the GVF and pressure. The mixture's property changes throughout the gap, and they must be recalculated at each step.

Given only inlet and outlet pressure boundary conditions, a direct solution of the flow is impossible. It must be solved through iteration by first guessing an initial static pressure as the fluid accelerates into the gap and then determining if the outlet pressure is consistent with the downstream reservoir pressure. A diagram of the inlet condition is shown in Figure 3.5. The upstream reservoir has a given stagnation pressure and temperature. At the entrance to the CV, the static pressure drops below the stagnation pressure as the fluid flows in. For incompressible and inviscid flow, Bernoulli's equation could be used to calculate the velocity given a guess of the static pressure.

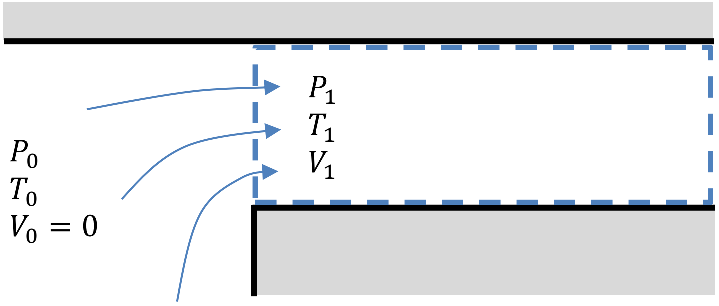

**Figure 3.5.** Inlet condition for a clearance control volume

However, this would not be appropriate for two-phase compressible flow.

For the case of frictionless, two-phase nozzle flow, the velocity is a function of the stagnation conditions and the GVF only, as shown in Equation (3.30) from Brennen [13],

$$V^2 = \frac{2p_0\alpha_0}{\rho_0}\left[\frac{1-\alpha_0}{\alpha_0} - \frac{(1-\alpha)}{\alpha} + \ln\left(\frac{(1-\alpha_0)\alpha}{\alpha_0(1-\alpha)}\right)\right] \tag{3.30}$$

where the 0 subscripts represent the reservoir conditions. This equation assumes that the fluid is barotropic (density is a function of pressure only) and isothermal. The isothermal assumption is a reasonable approximation for water and air mixtures due to the high heat capacity of water compared to air. Given enough mixing and a small enough bubble size, any rise in thermal energy in the gas phase could be absorbed by the liquid phase with negligible temperature rise. With an isothermal assumption, the fluid is also barotropic since it is composed of an incompressible liquid and a constant temperature ideal gas. Thus, Equation (3.30) is used to calculate the inlet velocity based on a guess of the static pressure.

In addition to the inlet pressure to the clearance, the inlet GVF is also an important factor that affects the leakage flow. The gas volume fraction that enters the clearance is not necessarily the same GVF as in the chamber. For example, the high speed rotation of the screws and resultant centrifugal forces usually cause the denser liquid phase to be more dominant at the clearance entrances. At low GVFs, there is little gas infiltration through the clearances. At GVFs higher than 80%, the fluid regime changes to a foam with more evenly distributed phases, so the GVF that enters the clearance is significantly larger. The GVF of the fluid that enters the clearance depends on many factors, but pump speed and the chamber GVF are perhaps the two most important. Räbiger [7] investigated this, and found that at lower pump speeds, there will be higher levels of gas infiltration as shown in Figure 3.6.

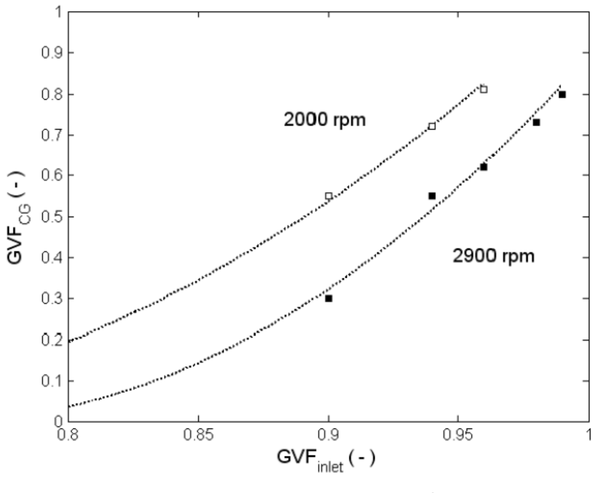

**Figure 3.6.** Correlation between the GVF at the circumferential clearance and the inlet GVF at 2000 RPM and 2900 RPM, from Räbiger, 2009 [7]

The present model incorporates a similar correlation that was developed empirically from experimental data. The specific equations for the correlation are shown in Table 3.1, and they are plotted in Figure 3.7.

On the topic of choked flow, Equation (3.22) shows that there is a singularity at $M = 1$. At this point, the flow chokes. For pure Fanno flow, the choke will always occur at the end of the duct. If the duct were extended, it will still choke at the end, but

**Table 3.1.** Correlation used to estimate the GVF at the inlet to the clearance

| Pump Speed [RPM] | Clearance GVF |
|---|---|
| 900 | $\alpha_{clearance} = \begin{cases} 0.5\alpha_{ch}, & x \leq 0.5 \\ 1.1\alpha_{ch}^2 - 0.43\alpha_{ch} + 0.19, & x > 0.5 \end{cases}$ |
| 1350 | $\alpha_{clearance} = \begin{cases} 0.4\alpha_{ch}, & x \leq 0.5 \\ 1.4667\alpha_{ch}^2 - 0.96\alpha_{ch} + 0.3133, & x > 0.5 \end{cases}$ |
| 1800 | $\alpha_{clearance} = \begin{cases} 0.3\alpha_{ch}, & x \leq 0.6 \\ 2.625\alpha_{ch}^2 - 2.2675\alpha_{ch} + 0.84, & x > 0.6 \end{cases}$ |

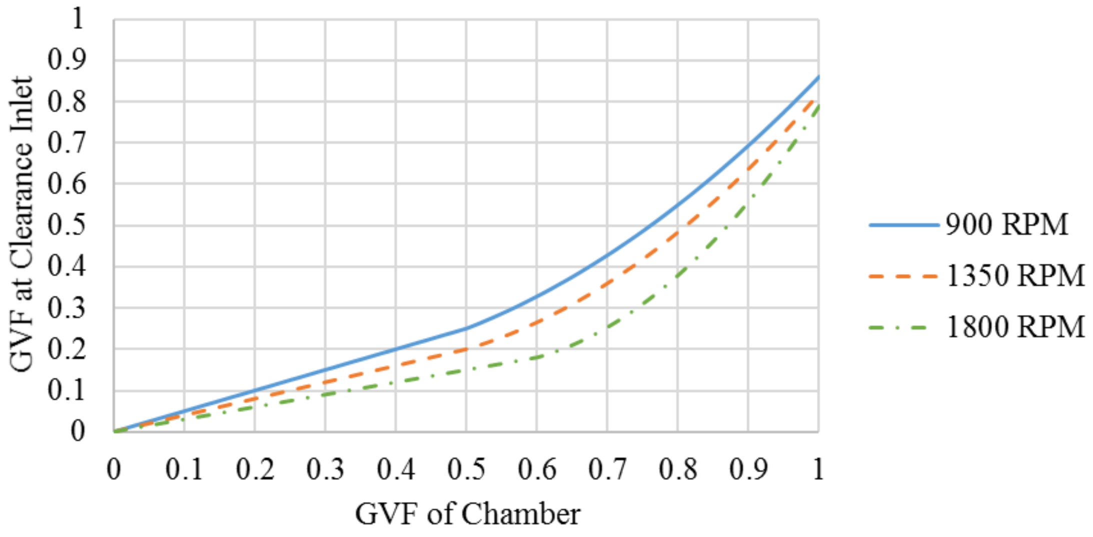

**Figure 3.7.** Correlation used to estimate the GVF at the inlet to the clearance

the mass flow rate would decrease to compensate. The Fanno flow model is most relevant for the circumferential and flank clearances. For a converging-diverging duct, choking would only occur at the throat where $dA/A = 0$. Flow through a duct with changing area is most applicable to the root clearance. The geometry and further discussion on choking conditions for the clearances are presented in the following sections.

To summarize this section, frictionless nozzle flow is assumed to determine the inlet velocity to the clearance, using Equation (3.30). The clearance channel is discretized into many 1-D control volumes. Based on a generalized form of compressible flow equations involving changing area and friction, the flow is solved using Equations (3.22), (3.28), and (3.29). The iterative guess of the inlet flow is correct if one of two conditions occur:

1. The flow chokes and the outlet pressure is higher than the downstream reservoir pressure
2. If the flow does not choke and the outlet pressure matches the downstream reservoir pressure.

The solver algorithm is discussed in more detail in Section 3.4.

### *3.3.2. Circumferential Clearance*

The circumferential clearance is the gap between the screws and the liner, as shown in Figure 3.8. The clearance has a helical shape, but nonetheless it is approximated as a rectangular channel. Different views of the circumferential clearance are shown in Figure 3.9. For these diagrams, $\delta_{cc}$ is the circumferential clearance height, $\delta_{rc}$ is the radial clearance height, $R_i$ and $R_o$ are the inner and outer diameters, $a$ is the distance between the axes of the rotors, $h$ is the screw pitch, $B$ is the width of the screw land over which the circumferential leakage flows, $L_{cc}$ is the length of the circumferential clearance region for one spindle, and $\beta$ is the angle between the

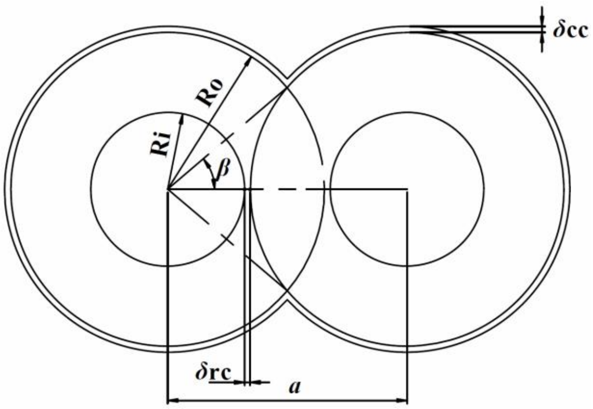
δcc
Ro
Ri
β
δrc
a

**Figure 3.8.** Profile view showing the circumferential ($\delta_{cc}$) and radial clearances ($\delta_{rc}$)

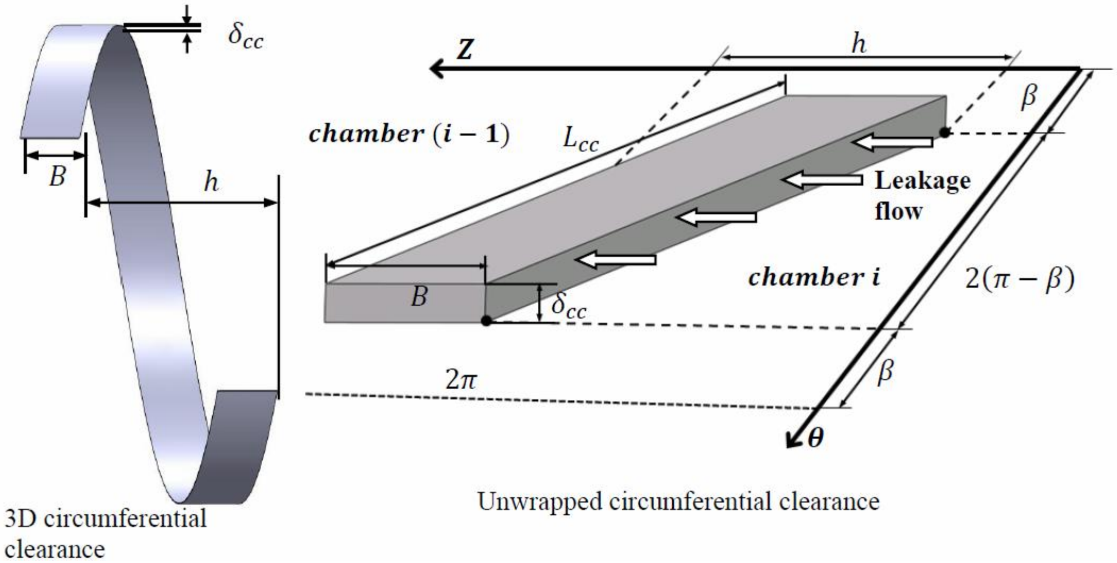
$\delta_{cc}$
B
h
3D circumferential clearance
Z
h
$\beta$
chamber $(i-1)$
$L_{cc}$
Leakage flow
chamber $i$
$2(\pi-\beta)$
B
$\delta_{cc}$
$2\pi$
$\beta$
$\theta$
Unwrapped circumferential clearance

**Figure 3.9.** Circumferential clearance, from Muhammad, 2013 [11]

centerline and the point where the screws begin to overlap. The cross-sectional area for the clearance over one spindle is given by Equation (3.31),

$$A_{cc} = L_{cc}\delta_{cc} \tag{3.31}$$

and the term $L_{cc}$ can be calculated from the following equation [11],

$$L_{cc} = 2(\pi - \beta)\sqrt{R_o^2 + \left(\frac{h}{2\pi}\right)^2} \tag{3.32}$$

The angle $\beta$ is calculated as

$$\beta = \cos^{-1}\left(\frac{a}{2R_o}\right) \tag{3.33}$$

where,

$$a = R_i + R_o + \delta_{rc} \tag{3.34}$$

This completes the geometry for the circumferential clearance.

The pressure-driven leakage flow through the circumferential clearance is calculated according to the method described in Section 3.3.1. The cross-sectional area is constant throughout, so the governing equations simply reduce to Fanno flow equations. The behavior of the flow is dictated by upstream (chamber $i$) and downstream (chamber $i-1$) reservoir pressures. As the pressure difference across the channel increases, the flow increases. The critical pressure, $P^*$, is defined as the pressure when the flow reaches $M = 1$. For a given upstream stagnation pressure, the static pressure anywhere in the gap will not decrease below $P^*$ regardless of how low the back pressure is. The pressure and Mach distributions for Fanno flow are shown in Figure 3.10. If the back pressure is higher than the critical pressure, the flow is not

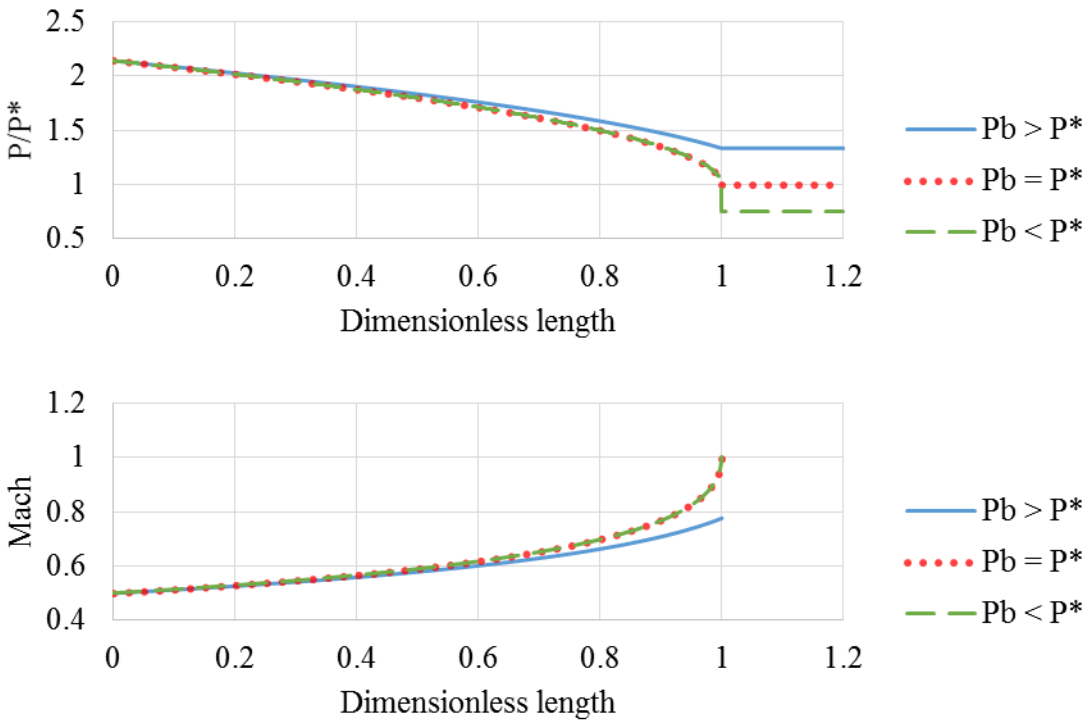

**Figure 3.10.** Pressure and Mach distributions for subsonic Fanno flow with varying back pressures, $P_b$. Dimensionless length of 1 denotes the outlet of the channel.

choked. If the back pressure is lower than or equal to the critical pressure, the flow chokes at the outlet of the channel. Once the flow chokes, decreasing the back pressure any further would have no effect on the flow within the channel. Any difference between the outlet pressure and the downstream reservoir pressure are equalized through expansion waves, which are neglected in the present model. While typical Fanno flow problems can be solved analytically by calculating the critical conditions, two-phase compressible flow must be solved iteratively in small steps since the gas volume fraction changes as the flow progresses through the clearance.

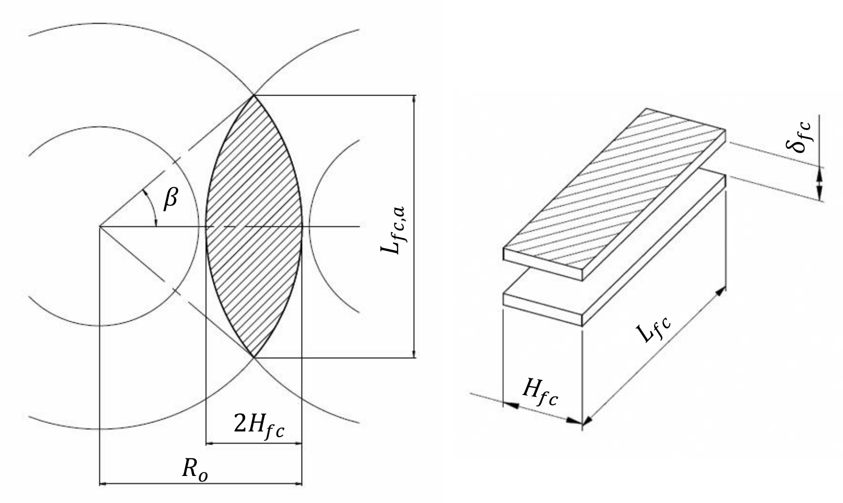

**Figure 3.11.** Flank clearance and a rectangular approximation of the channel

### *3.3.3. Flank Clearance*

The flank leakage is similar to the circumferential leakage. They both are constant area channels. The surface area of the flank clearance forms a lens shape from the overlap of the two screws, as shown in Figure 3.11. To simplify the geometry, the channel is treated as rectangular with the same surface area as the lens shape. The maximum width of the actual lens-shaped flank clearance is calculated as,

$$2H_{fc} = R_o - R_i - \delta_{rc} \tag{3.35}$$

and the width of the approximated. rectangular clearance is set to $H_{fc}$. The surface area of one side of the flank clearance channel is calculated as,

$$A_{fc,s} = \frac{1}{2}\left[D_o^2\beta - aD_o\sin(\beta)\right] \tag{3.36}$$

The length of the approximated channel is then simply,

$$L_{fc} = \frac{A_{fc,s}}{H_{fc}} \tag{3.37}$$

The cross-sectional area of the channel is the width times the clearance thickness,

$$A_{fc} = H_{fc}\delta_{fc} \tag{3.38}$$

The flank clearance connects four chambers: a pair of $i$ and $i + 1$ chambers on one spindle and the neighboring pair on the other spindle. For simplicity, the flank clearance leakage flow was assumed to travel only from the $i + 1$ chamber to the $i$ chamber corresponding to a single spindle. Given the geometry of the flank clearance that has been described, the flank leakage flow is solved in a similar way as the circumferential clearance.

### *3.3.4. Root Clearance*

The root clearance is more complex due to its converging-diverging shape. The radial gap between the root diameter of one spindle and the outer diameter of the other is shown in Figure 3.12. In this diagram, the upper portion is chamber $i$, and the lower portion is chamber $i - 1$. A coordinate system is set up as shown in the diagram, with $y = 0$ corresponding to the centerline connecting points $C_1$ and $C_2$. Figure 3.13 shows the root clearance domain and the control volume used. The flow goes in the downward direction, and the rotation of the screws increase the leakage rate. At a given location, $y$, the width of the control volume, $H_{rc}(y)$, is variable. At the throat, $H_{rc}(0) = \delta_{rc}$. The control volume has a depth equal to the width of the screw land, $B$. The width of the control volume is calculated as,

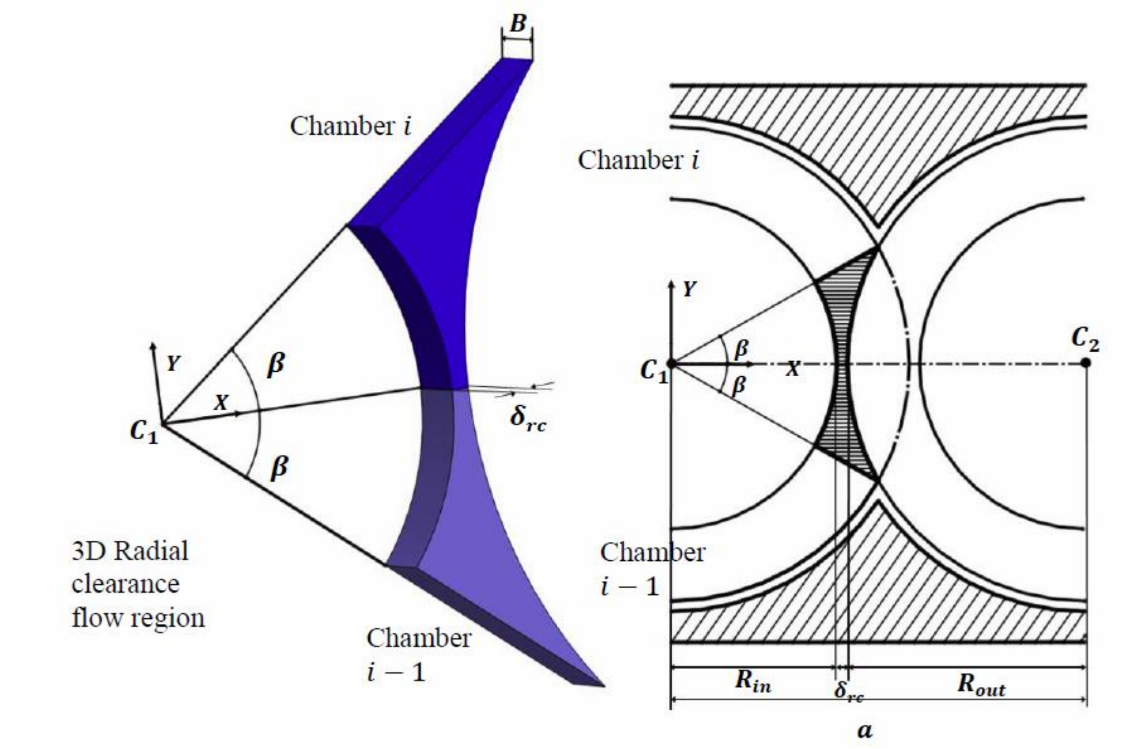
B
Chamber $i$
Chamber $i$
$Y$
$\beta$
$X$
$C_1$
$\beta$
$\delta_{rc}$
3D Radial clearance flow region
Chamber $i-1$
$Y$
$C_2$
$C_1$
$\beta$
$X$
$\beta$
Chamber $i-1$
$R_{in}$
$\delta_{rc}$
$R_{out}$
$a$

**Figure 3.12.** Root clearance flow region, from Muhammad, 2013 [11]

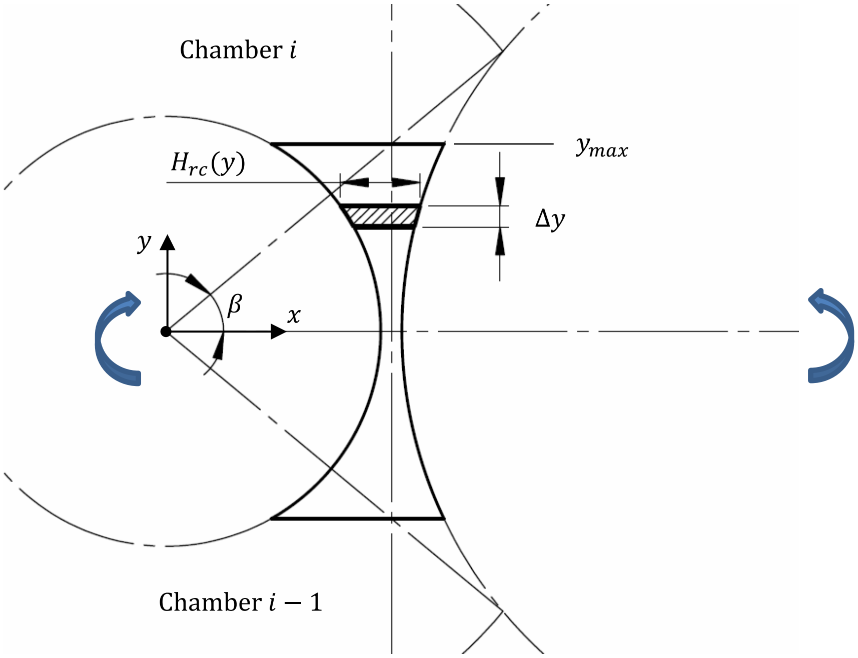
Chamber $i$
$y_{max}$
$H_{rc}(y)$
$\Delta y$
$y$
$\beta$
$x$
Chamber $i-1$

**Figure 3.13.** Domain and control volume for the root clearance flow region

$$H_{rc}(y) = a - \sqrt{R_i^2 - y^2} - \sqrt{R_o^2 - y^2} \tag{3.39}$$

The top of the root clearance domain is set at the location,

$$y_{max} = \left(R_i + \frac{\delta_{rc}}{2}\right)\tan\beta \tag{3.40}$$

as shown in the diagram. The domain is symmetric across the x-axis. The cross-sectional area of the converging-diverging channel is the following,

$$A_{rc} = B \cdot H_{rc}(y) \tag{3.41}$$

For the root clearance, the flow is solved using the same governing equations as the circumferential and flank clearances that were presented in Section 3.3.1. However in this case, both friction and change in area are accounted for. The pressure and velocity distributions of the flow through a converging-diverging channel is much different. As the fluid passes through the throat, it must accelerate to satisfy the continuity equation. As the velocity increases, the pressure will drop, and choked flow is much more likely to occur. An example of the pressure, velocity, and temperature distributions through the root clearance is shown in Figure 3.14. In the graphs, the throat is located in the middle when the gap length equals 0.009 m. If the velocity at the throat reaches Mach 1, the flow will choke. Equivalently, if the pressure at the throat drops to the critical pressure, the flow will choke. The differential pressure across the gap can also be seen in the pressure graph. Decreasing the differential pressure will increase the pressure at the throat. Conversely, if the differential pressure is too large, then the throat pressure drops, which may lead to choking. The method for solving the root leakage

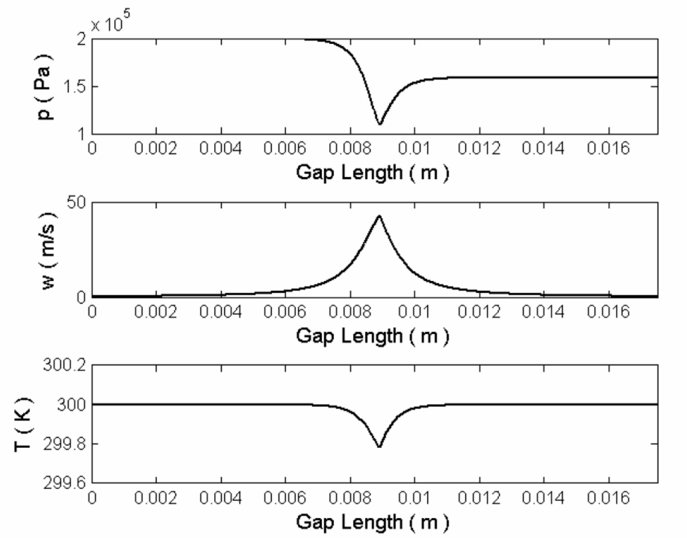

**Figure 3.14.** Pressure, velocity, and temperature distributions through the radial clearance, from Räbiger, 2009 [7]

remains mostly the same except that the critical condition is checked at the throat rather than at the end of the clearance.

### *3.3.5. Couette Flow*

Up until this point, only pressure-driven flow under the assumption of static walls has been discussed. The other component is the Couette flow, where pressure gradients are ignored and flow occurs due to the shear stress from moving walls. Couette flow for each of the three clearances is discussed.

For the circumferential clearance, shear stress occurs in the tangential direction when the screws rotate. However during the rotation, the length of the circumferential gap effectively decreases. This can be visualized from the unwrapped screw lands shown in Figure 3.15. Based on the $\eta$-$\zeta$-$\xi$ coordinate system defined in the diagram, the

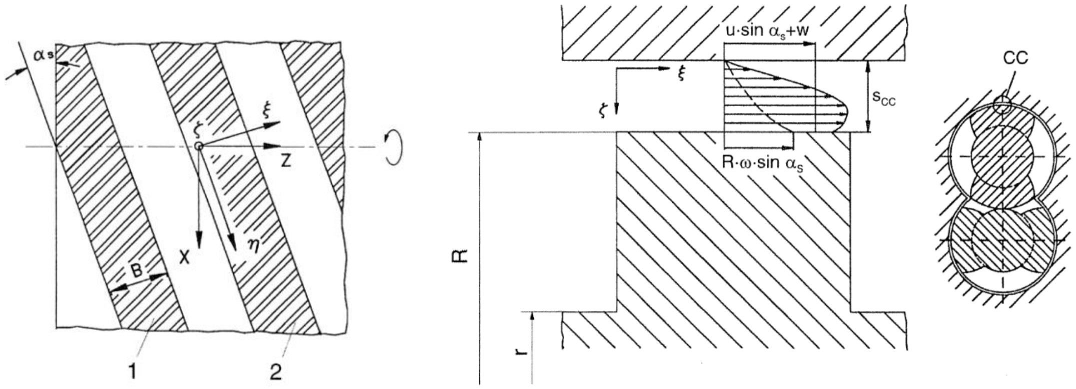

**Figure 3.15.** Unwrapped screw geometry for the circumferential clearance (left) and velocity profile with Couette flow (right), from Vetter et al., 2000 [3]

tangential rotation will contribute to the circumferential leakage. The velocity profile with the contribution of Couette flow is also shown in Figure 3.15. The Couette flow through the circumferential clearance is given by the following Equation (3.42) [7],

$$Q_{Couette,cc} = \delta_{cc} L_{cc} \sin(\alpha_s) \left(\frac{R_o^2 \omega}{\delta_{cc}}\right) \left[\ln\left(\frac{R_o + \delta_{cc}}{R_o}\right) \left(1 + \frac{R_o^2}{(R_o + \delta_{cc})^2 - R_o^2}\right) - \frac{1}{2}\right] \tag{3.42}$$

where $\alpha_s$ is the spindle inclination angle. This angle can be calculated using the screw pitch and outer diameter,

$$\alpha_s = \tan^{-1}\left(\frac{h}{\pi D_o}\right) \tag{3.43}$$

For the flank clearance, the screws rotate in the same direction as the leakage flow. The average volumetric flowrate can be approximated as the velocity at the center of the clearance times the cross-sectional area,

$$Q_{Couette,fc} = \delta_{fc} H_{fc} \omega \frac{R_i + R_o}{2} \tag{3.44}$$

For the root clearance, the Couette flow is again determined from the average wall speed since the velocity profile is linear. This equation is,

$$Q_{Couette,rc} = \delta_{rc} B \omega \frac{R_i + R_o}{2} \tag{3.45}$$

Finally, the total leakage will be the sum of the pressure-driven flow and Couette flow.

### *3.3.6. Eccentricity Effects on the Circumferential Leakage Flow*

Due to the helical shape of the chambers, the pressure distribution around the spindle is not symmetrically balanced. Figure 3.16 shows the staggered pressure distribution that causes the unbalanced radial loading. The pressure on one side of the spindle is higher than the other, so the net radial force deflects the rotor. From Prang &

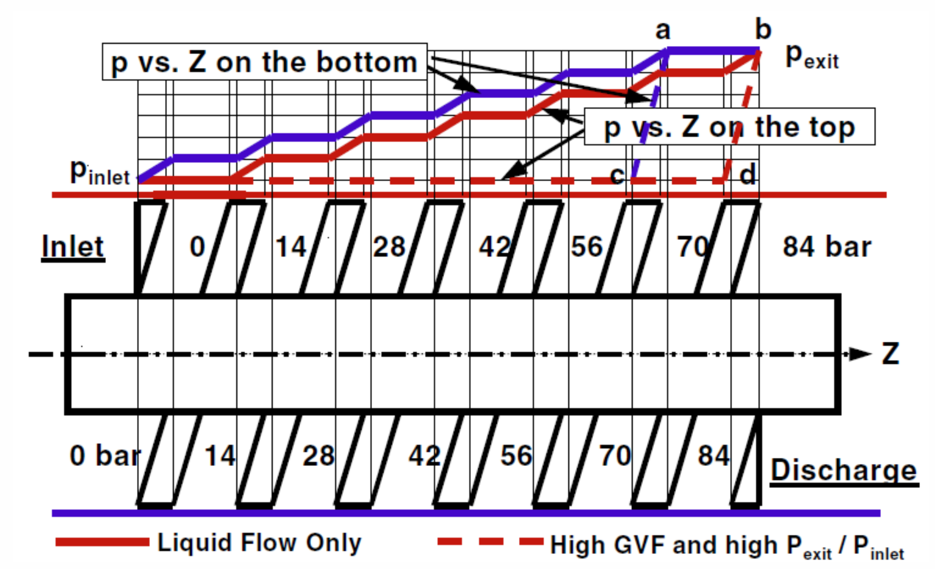
a
b
$p_{exit}$
p vs. Z on the bottom
p vs. Z on the top
$p_{inlet}$
c
d
Inlet
0
14
28
42
56
70
84 bar
Z
0 bar
14
28
42
56
70
84
Discharge
Liquid Flow Only
High GVF and high $P_{exit}$ / $P_{inlet}$

**Figure 3.16.** Pressure distribution throughout the TSP chambers, from Prang & Cooper, 2004 [9]

Cooper [9], the net hydraulic forces on the rotor are independent of the specific pressure distribution. Instead, it is dependent on the pressure difference across the entire pump as well as the screw pitch. Specifically, the radial force is calculated from the following equation:

$$F_r = h(D_i + D_o)\Delta P \tag{3.46}$$

The deflection of the rotor causes variation in the size of the clearance around the circumference as shown in Figure 3.17. The clearance is no longer uniform around the screw, and the eccentricity leads to increased leakage flow. The increase in leakage rates can be quantified as the ratio of the flowrate during eccentric operation to the flowrate during centered operation:

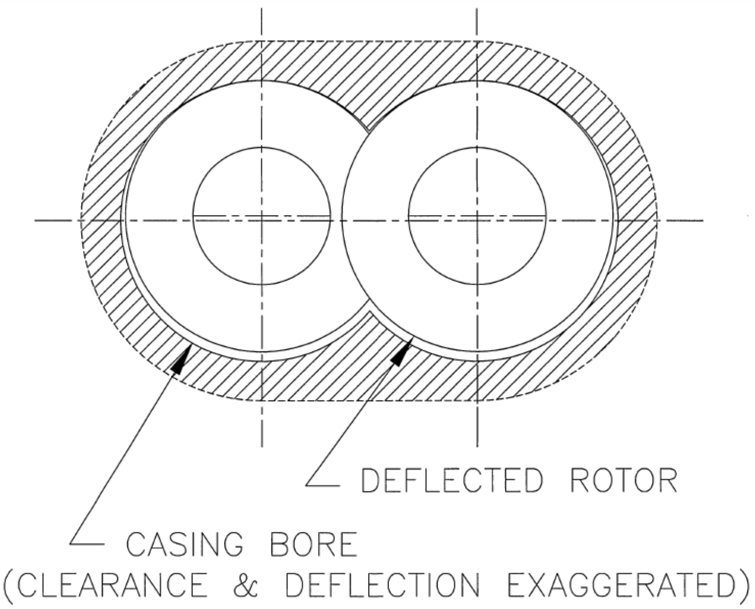

**Figure 3.17.** Change in the circumferential clearance due to rotor deflection, from Prang & Cooper, 2004 [9]

$$r_\varepsilon \equiv \frac{Q_{cc,eccentric}}{Q_{cc,centered}} \tag{3.47}$$

For laminar flow, this ratio is given by the following equation [11]:

$$r_\varepsilon = 1 + \frac{3}{2}\varepsilon^2 \tag{3.48}$$

For turbulent flow, the ratio can be calculated as,

$$r_\varepsilon = \frac{1}{\pi}\int_0^\pi (1 + \varepsilon \cos\theta)^{\frac{3}{2-n_e}}\, d\theta \tag{3.49}$$

where $\varepsilon$ is a dimensionless variable of eccentricity and $n_e$ is a factor equal to 0.25 for smooth surfaces and 0 for rough surfaces. The relative eccentricity, $\varepsilon$, is defined as,

$$\varepsilon(z) \equiv \frac{e(z)}{\delta_{cc}} \tag{3.50}$$

where $e$ is the deflection.

As shown in Figure 3.18, the deflection and eccentricity is not constant along the rotor. Bearings support the rotor at the ends, and the deflection is greatest in the middle. To calculate the deflection, the rotor is modeled as a simply supported beam with uniform loading. The deflection at any given point is given by,

$$e(z) = \frac{2F_r}{L_{rotor}} \frac{z(L_{rotor} - z)}{24EI} [L_{rotor}^2 + z(L_{rotor} - z)] \tag{3.51}$$

where $E$ is the elastic modulus, $I$ is the second moment of area, and $L_{rotor}$ is the length of the rotor between the bearings. The second moment of area for the rotor can be calculated from the following equation:

$$I = \frac{\pi D_i^4}{64} \tag{3.52}$$

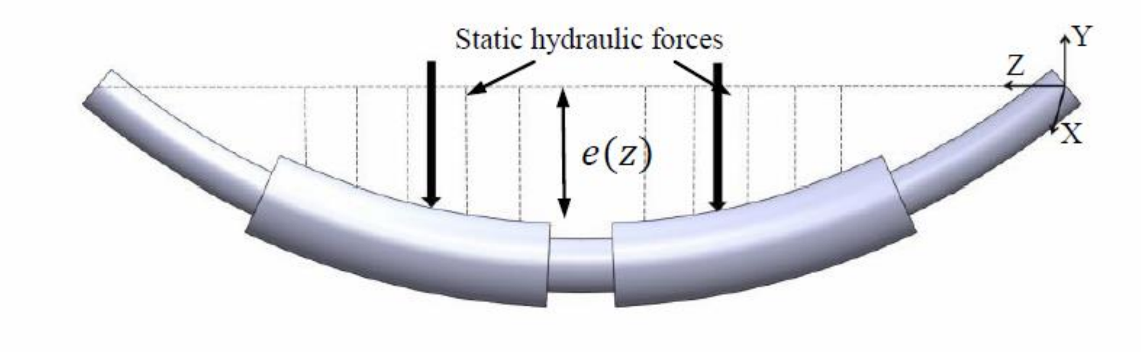

**Figure 3.18.** Exaggerated deflection of the screw rotor, from Muhammad 2013 [11]

All of these equations can be used to calculate the increase in leakage flow rate, $r_\varepsilon$, at any given position $z$. The final leakage flow rates are calculated by factoring in $r_\varepsilon$ for each circumferential clearance according to their position along the rotor.

### 3.4. Structure of the Computational Model

In the computational model, the program is first initialized with many input parameters. These include physical dimensions, pump speed, inlet GVF, differential pressure, and suction pressure. Initially, the pressure distribution throughout the TSP is set as linear, and the temperature distribution is set as uniform. Every revolution is divided into many small time steps.

During each time step, two main processes occur. The program first calculates the leakage through each circumferential, flank, and root clearance across the pump. After knowing the leakage flow rates, the program solves the liquid and gas mass balances in each chamber, and then it calculates the thermodynamic state of each chamber.

At the end of one rotation, the state of every chamber $i$ becomes the new state for the chamber $i + 1$. The last chamber disappears, and a new chamber is created at the front with the same properties as the suction.

For solving the flow through each clearance, an iterative algorithm is necessary to determine the correct initial inlet condition. The algorithm is shown in Figure 3.19. The program has solved the flow correctly if either of two cases are reached:

1. The flow has not choked, and the clearance exit pressure equals the downstream reservoir pressure
2. The flow has choked, and the clearance exit pressure is greater than or equal to the downstream reservoir pressure

The critical conditions for the circumferential, flank, and root clearances are different, but the overall process remains the same. After several rotations have been solved so that the solution converges, the volumetric efficiency is calculated based on the theoretical flowrate minus the sum of the leakage rates from the first chamber back to the suction inlet.

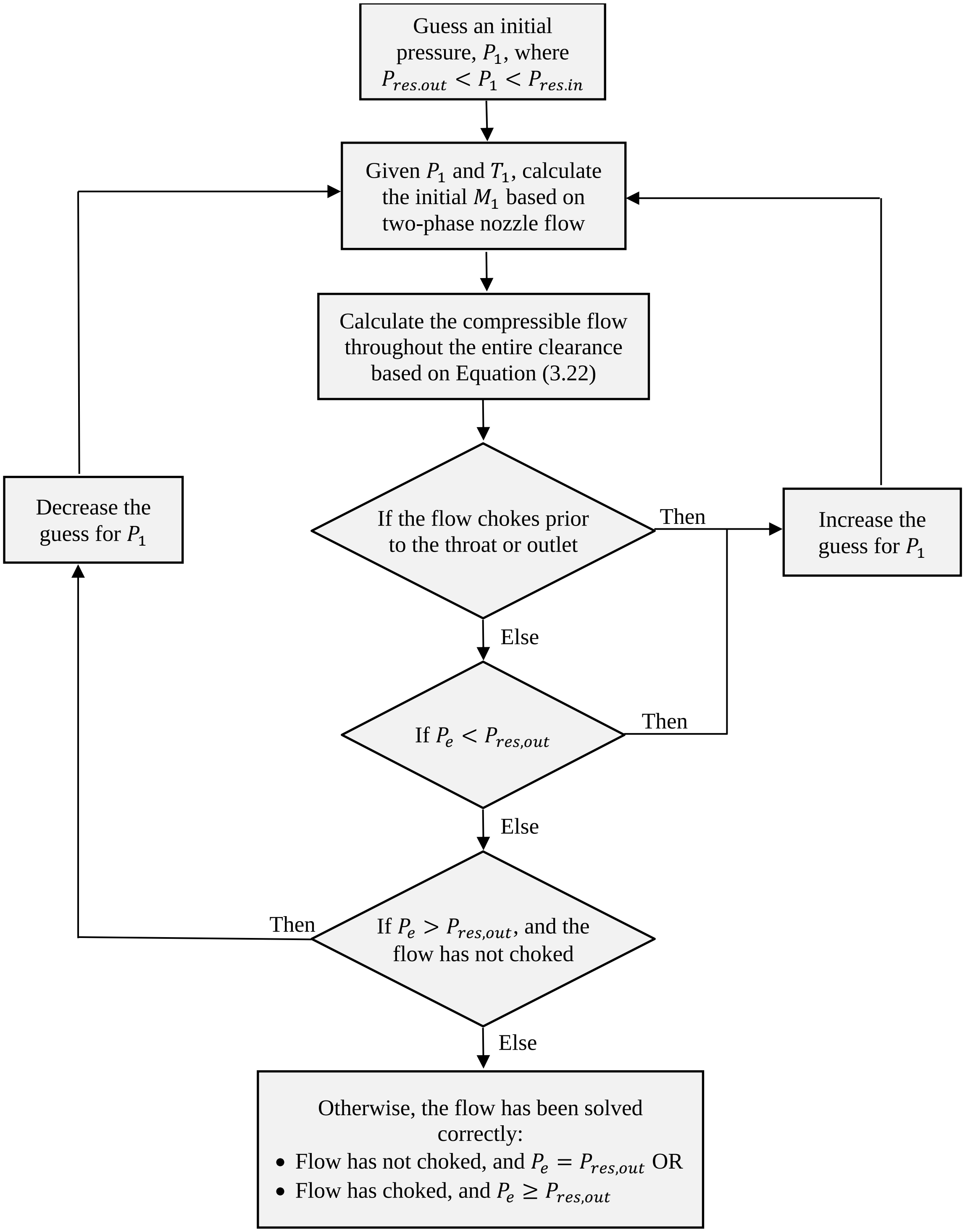
Guess an initial pressure, $P_1$, where $P_{res.out} < P_1 < P_{res.in}$
Given $P_1$ and $T_1$, calculate the initial $M_1$ based on two-phase nozzle flow
Calculate the compressible flow throughout the entire clearance based on Equation (3.22)
If the flow chokes prior to the throat or outlet
Then
Increase the guess for $P_1$
Else
If $P_e < P_{res,out}$
Then
Else
Decrease the guess for $P_1$
Then
If $P_e > P_{res,out}$, and the flow has not choked
Else
Otherwise, the flow has been solved correctly:
• Flow has not choked, and $P_e = P_{res,out}$ OR
• Flow has choked, and $P_e \geq P_{res,out}$

**Figure 3.19.** Computer algorithm for solving leakage flows

# 4. RESULTS AND DISCUSSION

The model is validated with experimental results from a study done by Patil [6]. The specific TSP is the Colfax MR-200 running water and air mixtures. The operating conditions varied with the following parameters: pump speed, GVF, suction pressure, and differential pressure (dP). The specific test parameters are listed in Table 4.1. The nominal GVF is the GVF to the inlet of the pump. However, this pump uses seal flush recirculation, which recirculates liquid from the discharge back to the suction. This function helps block the clearances during very high GVF operation by adding liquid to the working fluid. However, the results in the present study refer to actual GVF values within the pump rather than the nominal values.

TSP performance is affected by many factors, including the pressure distribution, presence of critical flows, and eccentric rotation caused by spindle deflection. These factors all vary according to the pump's operating conditions. This study first validates

**Table 4.1.** Test matrix for the Colfax MR-200 TSP

| Pump Speed (RPM) | Nominal GVF | Suction Pressure (psig) | dP (psig) |
|---:|---:|---:|---:|
| 900 | 50% | 15 | 50 |
| 1350 | 70% | 50 | 100 |
| 1800 | 90% | 75 | 150 |
| | 95% | 100 | 200 |
| | 98% | | 250 |
| | 99% | | 300 |
| | 100% | | |

the model based on experimental data and then thoroughly examines the relationships among the pump performance, operating conditions, and flow behavior. Section 4.2 discusses how the operating conditions affect the pressure distribution within the pump. Section 4.3 analyzes how each of the operating parameters affect the volumetric efficiency. Section 4.4 and 4.5 discuss the impact of critical flows and eccentric operation, respectively. Lastly, Section 4.6 examines the differences among each of the circumferential, flank, and root clearances.

## 4.1. Model Validation

From the permutations of the four testing parameters, there were a total of 495 experimental data points. Overall, the model has good agreement with the experimental data. Section 4.1.1 provides a statistical overview comparing results from the present model and experimental data. Section 4.1.2 presents a selection of the results and discusses deviations with the experimental data and the overall validity of the model.

### *4.1.1. Statistical Overview*

For all of the cases, the relative error between volumetric efficiency of the model and the experimental data was calculated. The histogram in Figure 4.1 shows the distribution of the error. Around 60% of cases had less than 5% error, and 85% of cases had less than 10% error. The average for all of the cases is 6.0%, and the median error is 3.7%.

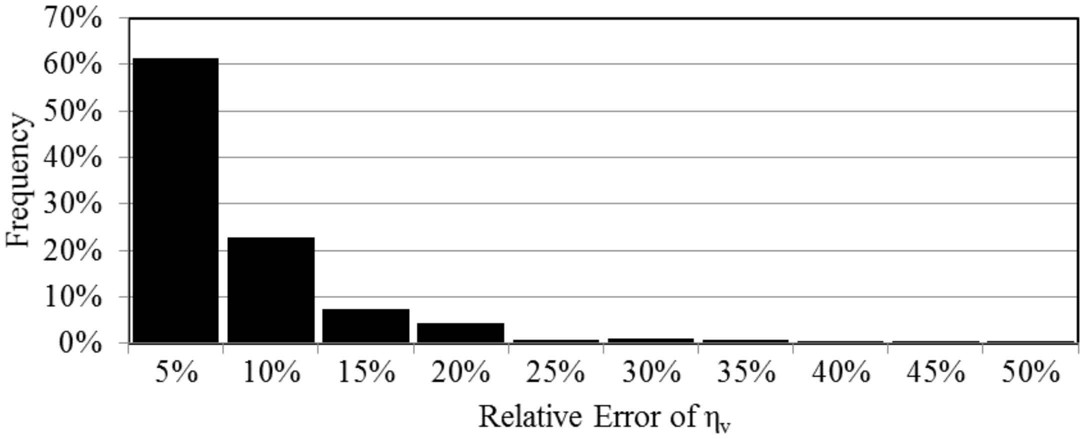

**Figure 4.1.** Error distribution for volumetric efficiency

In general, the model matches the experimental data more consistently at the design speed of 1800 RPM. The model is less consistent when the pump operates at conditions of low pump speeds combined with high pressure heads. Table 4.2 shows a statistical correlation between the error and the input parameters. The values describe how the error changes with specific parameters, holding all else equal. Based on the correlation, the model tends to be more accurate for higher speeds, lower GVF, and lower differential pressures. Changes in suction pressure do not have a statistically significant influence on the error.

Throughout all the results presented, there are a few cases that were omitted due to lack of data. Specifically, 9 out of 21 of the cases with 100 psi suction and 300 psi differential pressures lacked data. Therefore, any averages involving either 100 psi suction pressure or 300 psi dP may be slightly skewed.

**Table 4.2.** Correlation between error from the model and the input parameters

| Correlation | Pump Speed | GVF | Suction Pressure | Differential Pressure |
|---|---|---|---|---|
| **Relative Error** | -0.449 | 0.181 | -0.024 | 0.263 |

### *4.1.2. Validation*

This section presents the efficiency curves comparing the present model with experimental data and with the model developed by Liu [5]. The graphs are selected, in order of increasing error, as a representative sample to demonstrate the range of cases where the model shows good agreement and poor agreement. Graphs for the complete set of cases can be found in the Appendix. Figures 4.2, 4.3, and 4.4 show efficiency curves as a sample of the best 50% of the cases. As seen from the figures, some of the predictions match the experimental data very well. However, curves generated by the model inevitably may deviate from the experimental data, such as for the 50-100 psi differential pressure cases shown in Figure 4.4.

In general, there are many inter-related factors that affect the shape of an efficiency curve. With Figure 4.4 as an example, the curve appears as a relatively flat line, which means that the model is not as sensitive to the differential pressure as it should be. Aspects of the model that tend to make the slope more negative are pressure-driven flows and eccentricity effects. Conversely, critical flows and Couette flow tend to make the slope flatter. For example, Liu’s model calculates leakage solely based on the flow through the circumferential clearance, which is almost entirely dependent on a

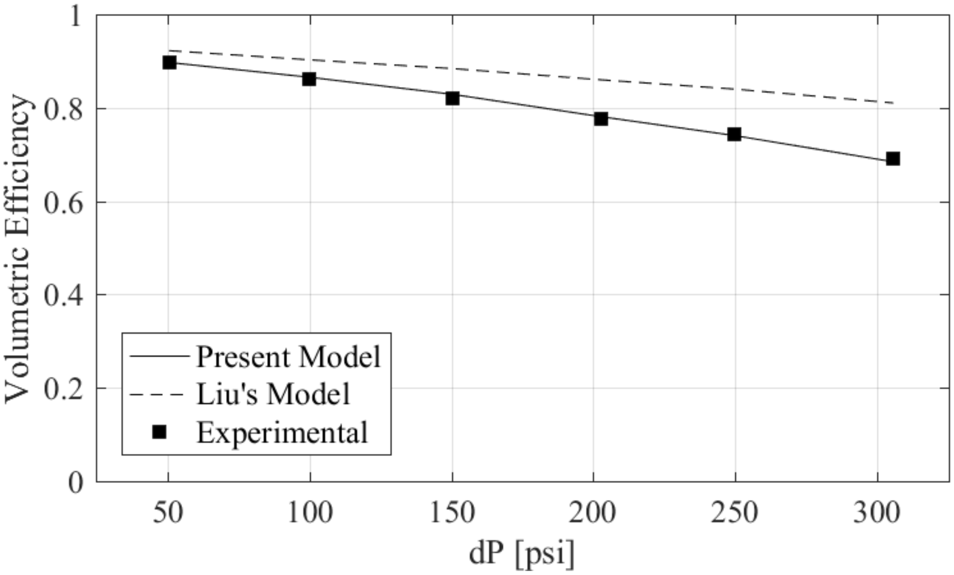

**Figure 4.2.** Efficiency curve for 15 psi suction, 1350 RPM, and 47% GVF. Predicted points have an average error of 0.6%.

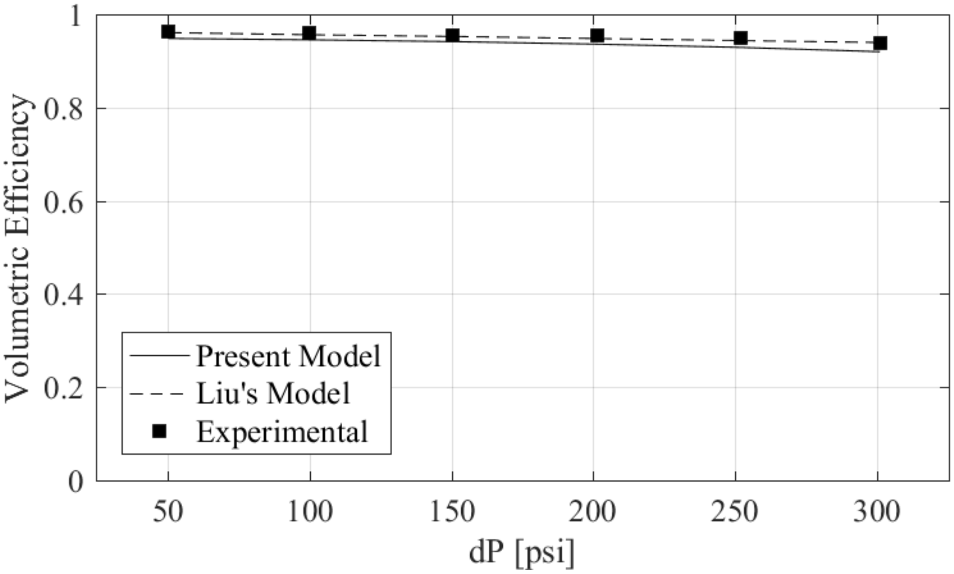

**Figure 4.3.** Efficiency curve for 100 psi suction, 1800 RPM, and 66% GVF. Predicted points have an average error of 1.9%.

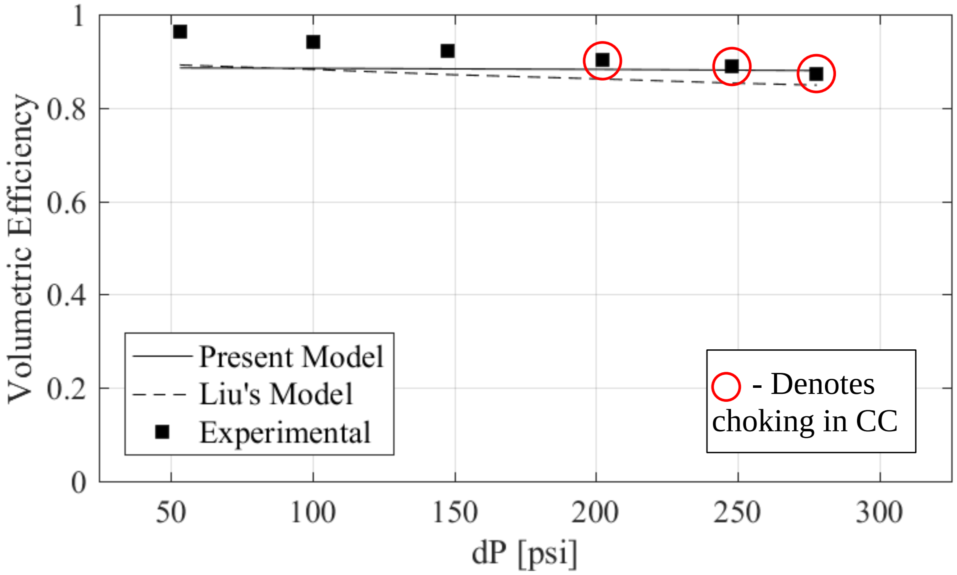

**Figure 4.4.** Efficiency curve for 75 psi suction, 1800 RPM, and 93% GVF. Predicted points have an average error of 3.7%. This curve represents the median cases.

pressure gradient. Leakage through the flank and root clearances is then attributed using a multiplied factor. Couette flow for the flank and root clearances is not accounted for in his model, and therefore his model is relatively more dependent on the differential pressure from this aspect.

The present model incorporates eccentricity effects, which are prominent at higher differential pressures due to increased rotor deflection. This should cause the efficiency curve to slope downward slightly. In this case, choked flow also occurs for the differential pressures of 200-300 psi. The choked flow causes the curve to be flatter because it limits the leakage that occurs due to large pressure gradients. Lastly, the high speed also causes the efficiency curve to be flatter because it increases the contribution of Couette flow—or equivalently, it decreases the relative importance of the pressure-driven flow—and raises the efficiency drastically. There are many interrelated factors that affect the graphs, but overall for the cases shown, the model has good agreement with the experimental data.

A curve that represents the average case with an error of 6.4% is shown in Figure 4.5. A set of curves that represent 25% of cases with the least accuracy are shown in Figures 4.6 and 4.7. In these figures, there is larger error for cases with high differential pressures, but overall the model shows the correct downward trend. Again at high differential pressures, two effects that become more prominent are the possibility of critical flow and rotor bending. While the model overestimates the efficiency, choking does not occur for any of these three figures. Further, the model never predicts choked flow at the slower 900 RPM speed under any of the tested operating conditions. This is because a higher speed is necessary to cause a steeper pressure distribution among the

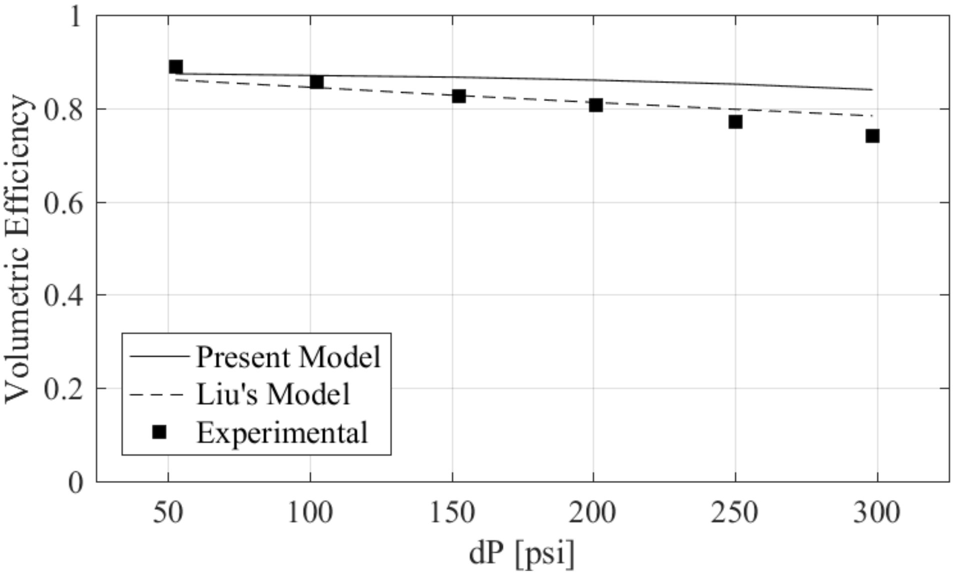

**Figure 4.5.** Efficiency curve for 50 psi suction, 1350 RPM, and 90% GVF. Predicted points have an average error of 6.4%.

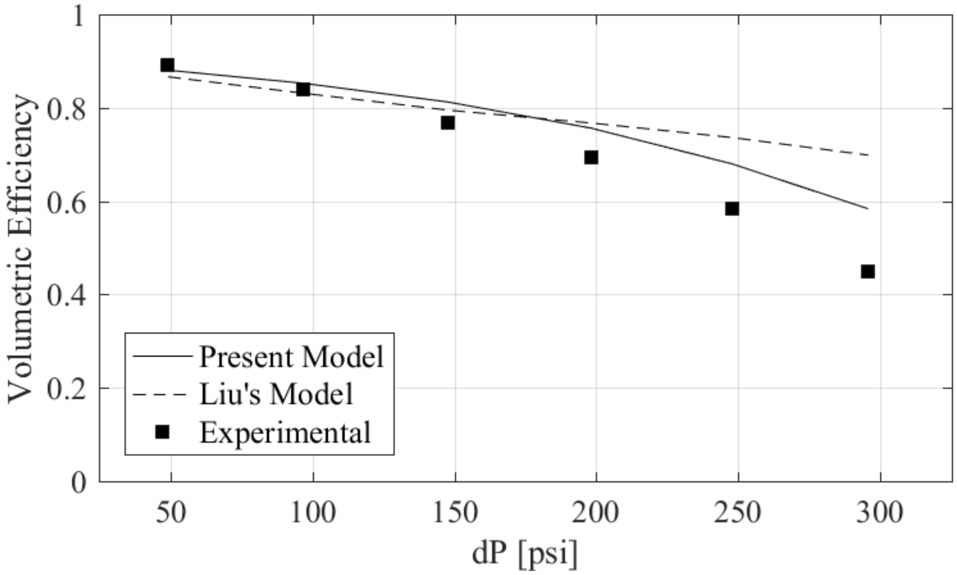

**Figure 4.6.** Efficiency curve for 15 psi suction, 900 RPM, and 85% GVF. Predicted points have an average error of 10.6%.

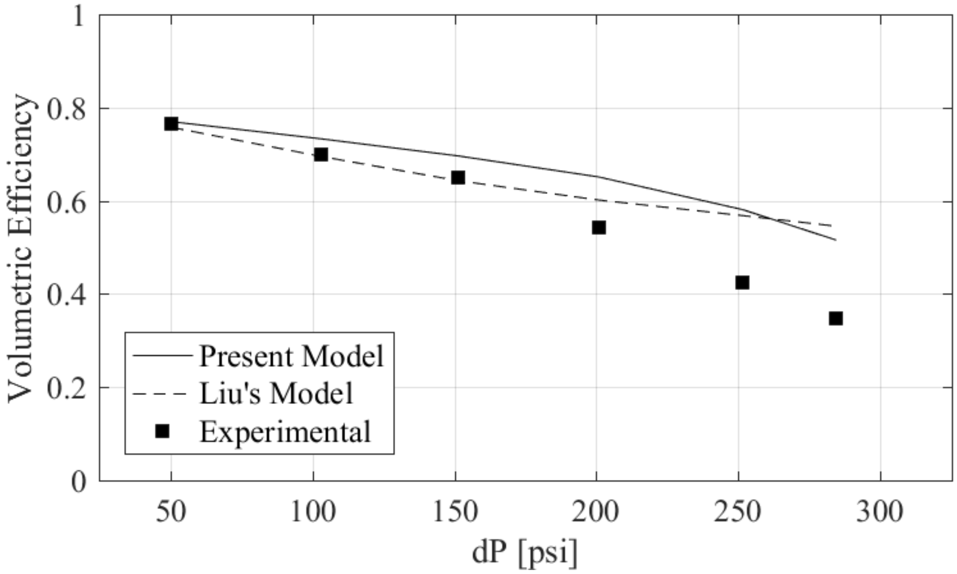

**Figure 4.7.** Efficiency curve for 50 psi suction, 900 RPM, and 94% GVF. Predicted points have an average error of 19.5%, which is the highest average error across all sets of cases.

chambers.  The eccentricity effect accounts for some of the lower efficiency at high heads, but the contribution is minor.  This is discussed in more detail in Section 4.5.

The main factor that contributes to the error is the slower pump speed.  At 1800 RPM, the present model, as well as Liu's model, shows very good agreement with the experimental data.  At this speed, the average error for the model is 2.9%.  At the slower speeds, both models exhibit larger deviations from the data.  On average, the present model is slightly more consistent than Liu's model at lower speeds, but there are a few cases where Liu's model has better agreement with the experimental data than the current model.

A main source of uncertainty at low speeds is the level of gas infiltration into the clearances and possible effects of different two-phase flow regimes, which are not directly modeled.  For the Colfax MR-200 TSP, the speed of 900 RPM is significantly below its design speed of 1800 RPM.  As described previously in Section 3.3.1, there is more gas infiltration at lower speeds when centrifugal effects are lower.  In the present model, this relationship is estimated empirically due to the lack of correlations in the current base of research.  In addition, there are also qualitative differences in the two-phase flow regimes that can occur at different conditions.  As described by Räbiger [7], the different flow regimes include slug flow with liquid droplets, churn flow, and annular flow with droplets.  In addition, Vetter et al. [3] have stated that the fluid in the cavity remains as two discrete phases below 85% GVF, and above 85% GVF, the fluid becomes a quasihomogeneous foam.  This effect would also certainly be influenced by

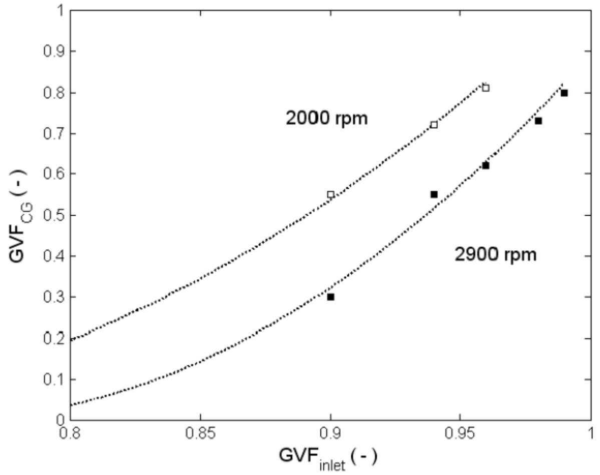

**Figure 4.8.** Correlation between the GVF at the circumferential clearance and the inlet GVF at 2000 RPM and 2900 RPM, from Räbiger, 2009 [7]

the pump speed. The present study makes simplifications, such as treating the leakage flow as homogeneous, despite the range of operating conditions.

Another source of uncertainty is the clearance dimensions. The clearances were determined based on a solid model of the pump. However, the measurements may differ from the actual pump depending on manufacturing tolerances and any abrasive wear. For the circumferential clearance, the model used a gap height of 280 microns, but even a change of 10 microns would lead to a noticeable change in efficiency. If the circumferential clearance size is smaller in the model than it is in the experimental conditions, then that would explain the model’s tendency to overestimate the volumetric efficiency at high differential pressures. This is because there would be a smaller proportion of leakage going through the circumferential clearances rather than the other two clearances, and this smaller proportion makes the leakage flow calculations less dependent on the pressure gradients.

Overall, the model shows good agreement in the majority of cases, especially at 1800 RPM. At slower speeds, the model also predicts the volumetric efficiency with reasonable accuracy, but there are a few cases when the model exhibits large errors. Despite this, the average error is 6%, and the model is still very useful for identifying the trends and behavior for TSP performance.

## 4.2. Pressure Distribution along the TSP

The pressure distribution along each of the chambers in a TSP has a major effect on the leakage flow and subsequently the pump performance. Vetter et al. [3] stated that the pressure distribution should be linear for pure liquid operation, and it should become more concave up as the GVF increases. At high GVF most of the pressure rise across the pump should occur within the last few chambers. The present model is consistent

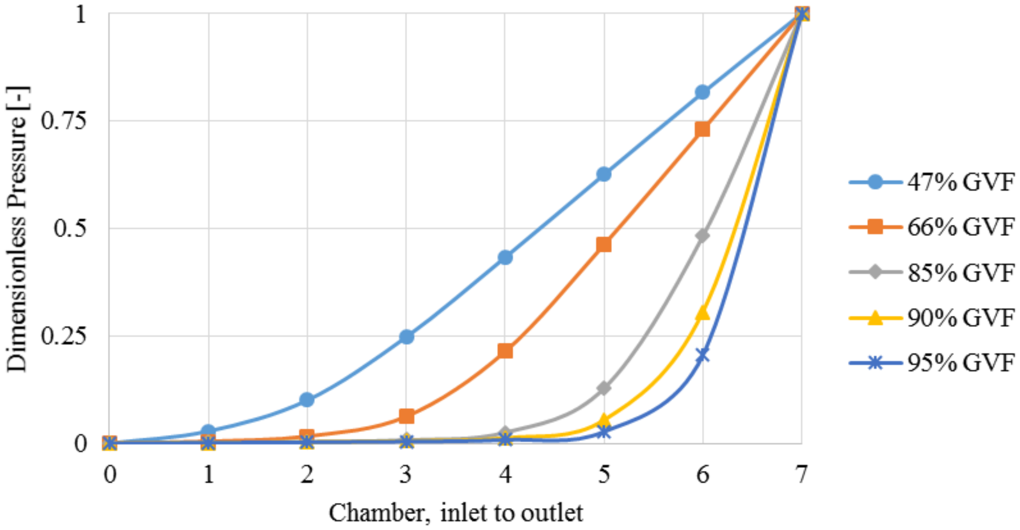

**Figure 4.9.** Pressure distribution for 15 psi suction pressure, 1800 RPM, 250 psi dP, and varying GVF

with this trend as shown in Figure 4.9. However, Vetter et al. continued to state that gas volume fractions higher than 85% would tend to become more linear again. The results do not show this change. The results are more consistent with Prang & Cooper's [9] opposite claim that very high GVF would lead to extreme pressure rise near the last lock. However, Prang & Cooper's claim is tenuous because, for the case of 100% GVF, there would be no liquid to seal the clearances, and there would be significant backflow and pressure equalization across the chambers.

The pressure distribution is very important for analyzing TSP performance due to the following: the leakage through the circumferential clearance comprises most of the total leakage, and the circumferential leakage is dominated by pressure-driven flow rather than Couette flow. Each of the operating parameters has an effect on the pressure distribution, and the following conditions lead to more concave pressure distributions:

- high GVF
- low suction pressure
- low differential pressure
- high pump speed

The effect of GVF was shown previously in Figure 4.9, and examples of varying suction pressures, pressure heads, and pump speeds are shown Figures 4.10, 4.11, and 4.12, respectively.

When the GVF is higher, the compressibility of the mixture is higher. Pressure and compressibility do not have a linear relationship, which explains the increased concavity in the distribution. Similarly, at low suction pressures, the gas phase is at

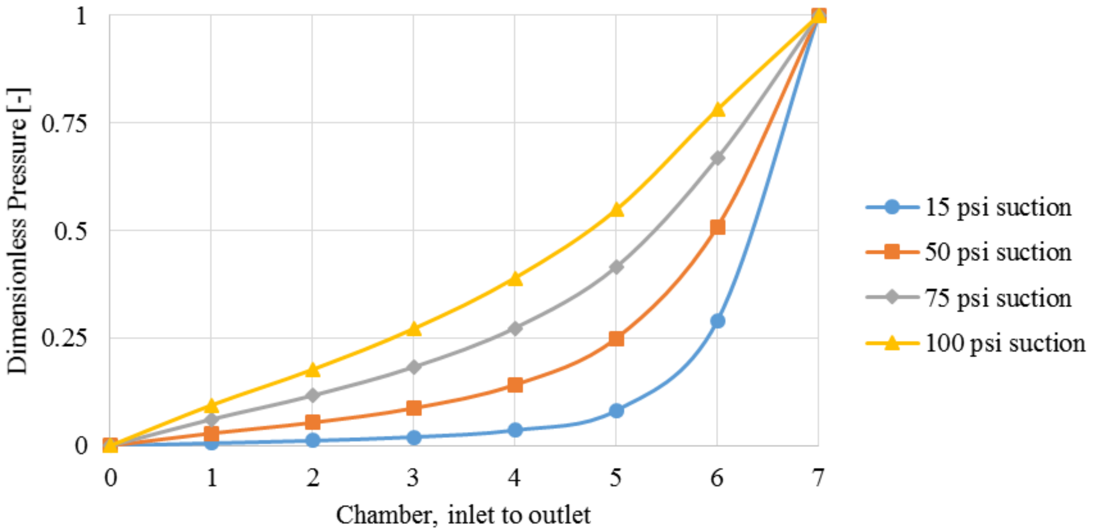

**Figure 4.10.** Pressure distribution for 1350 RPM, 95% GVF, 50 psi dP, and varying suction pressure

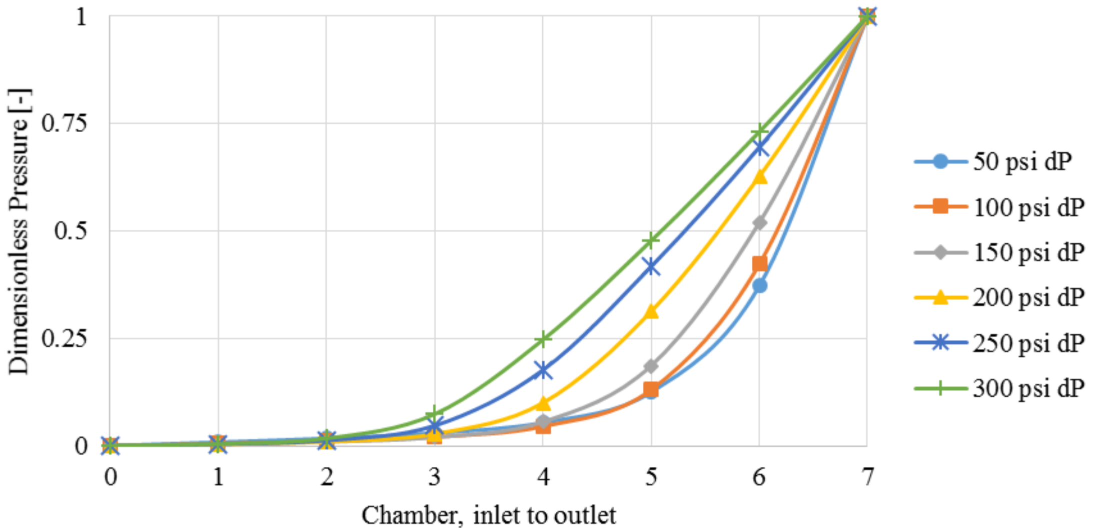

**Figure 4.11.** Pressure distribution for 15 psi suction pressure, 1350 RPM, 85% GVF, and varying differential pressure

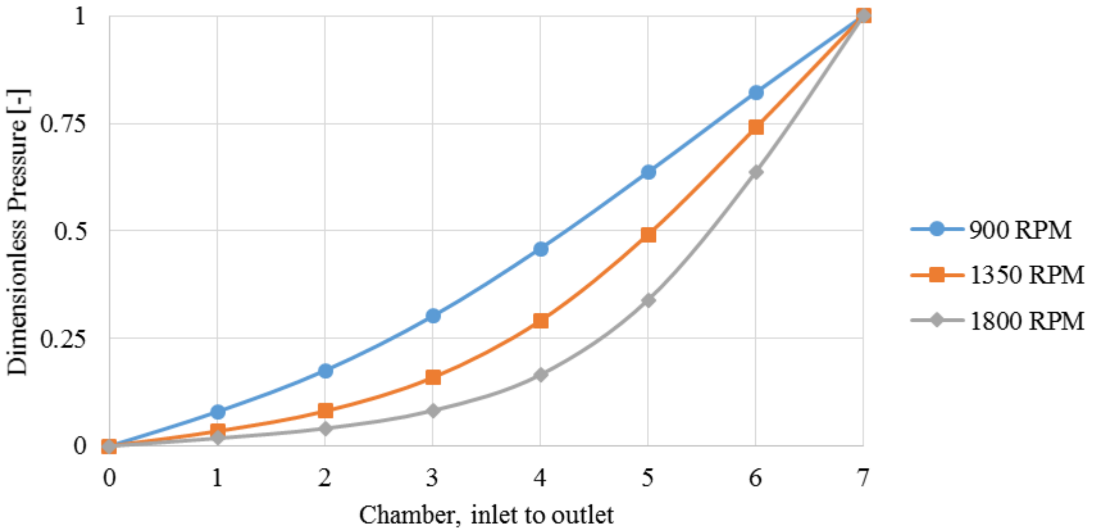

**Figure 4.12.** Pressure distribution for 15 psi suction pressure, 47% GVF, 50 psi dP, and varying pump speed

lower absolute pressures, which means the overall mixture is more compressible. At low differential pressures, the pressure driving force is smaller, so there is less leakage flow. Without a large differential pressure to drive leakage flow, the chambers remain at low pressures similar to the suction pressure. The pressure in a chamber rises much more quickly only once its neighbor reaches the discharge, and the pressure difference increases the leakage flowrate. Thus at lower pump heads, the pressure distributions are more concave. At higher pump speeds, the residence time for chambers in the pump decreases, so there is less time for the pressures of neighboring chambers to equalize via the leakage flow.

Only the leakage flowrate from the first isolated chamber back to the suction is used when calculating the volumetric efficiency. Concave pressure distributions have relatively small pressure rises near the suction side, and consequently the pressure-driven backflow will be low.  TSPs generally operate with better volumetric efficiency for conditions that lead to steep pressure distributions.  Therefore, TSPs generally have better performance for higher GVF fluids, lower suction pressures, lower pump heads, and higher pump speeds.  These effects are discussed more thoroughly in the next section.

## 4.3. Volumetric Efficiency Prediction

This section discusses how each of the operating conditions—differential pressure, GVF, pump speed, and suction pressure—affect the volumetric efficiency.  In general, the volumetric efficiency increases for the following conditions:

- High RPM
- High GVF
- Low differential pressure
- Low suction pressure

Figure 4.13 shows the general trends from the model, averaged over varying suction pressures.  In this section, only specific samples of data are presented, but data for all of the cases can be found in the Appendix.  The effects of specific flow phenomena, such as critical flows, are discussed in later sections.

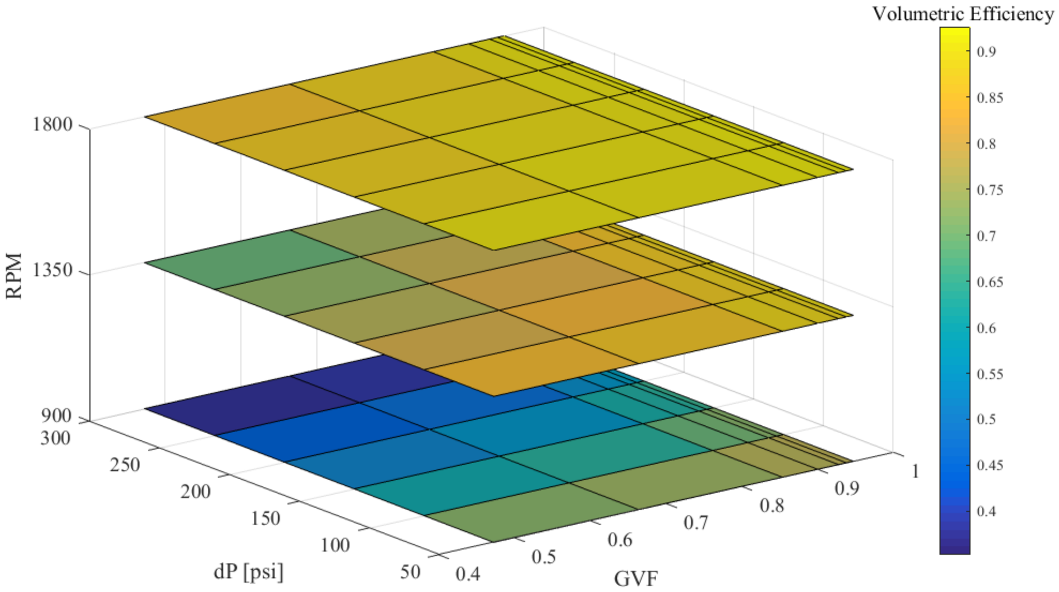

**Figure 4.13.** Volumetric efficiency (averaged across different suction pressures) as a function of RPM, differential pressure, and GVF

### 4.3.1. *Effect of Differential Pressure on Performance*

The volumetric efficiency of TSPs decreases as the pump head increases. Figure 4.14 shows the volumetric efficiency as a function of differential pressure averaged across all cases. As discussed in Section 4.2, TSPs pumping at higher differential pressures tend to have more linear pressure distributions as well as larger absolute pressure differences, both of which lead to increased backflow to the suction and, consequently, lower efficiency. This behavior is demonstrated by the negative slope in the figure. Further, the model shows good agreement with the experimental data on an averaged basis.

The impact of varying pressure heads on performance is not independent of the other parameters. At 1800 RPM, the differential pressure has little effect on the volumetric efficiency. Even at high heads, the efficiency remains relatively high. However, at 900 RPM, the pump performance drastically reduces for large differential pressures. Figures 4.15, 4.16, 4.17, and 4.18 show how the differential pressure affects the volumetric efficiency for varying pump speeds, suction pressures, and gas volume fractions. The negative slopes indicate the drop in efficiency that results if the head rises. In order to run at high differential pressures efficiently, the pump must operate at high speeds.

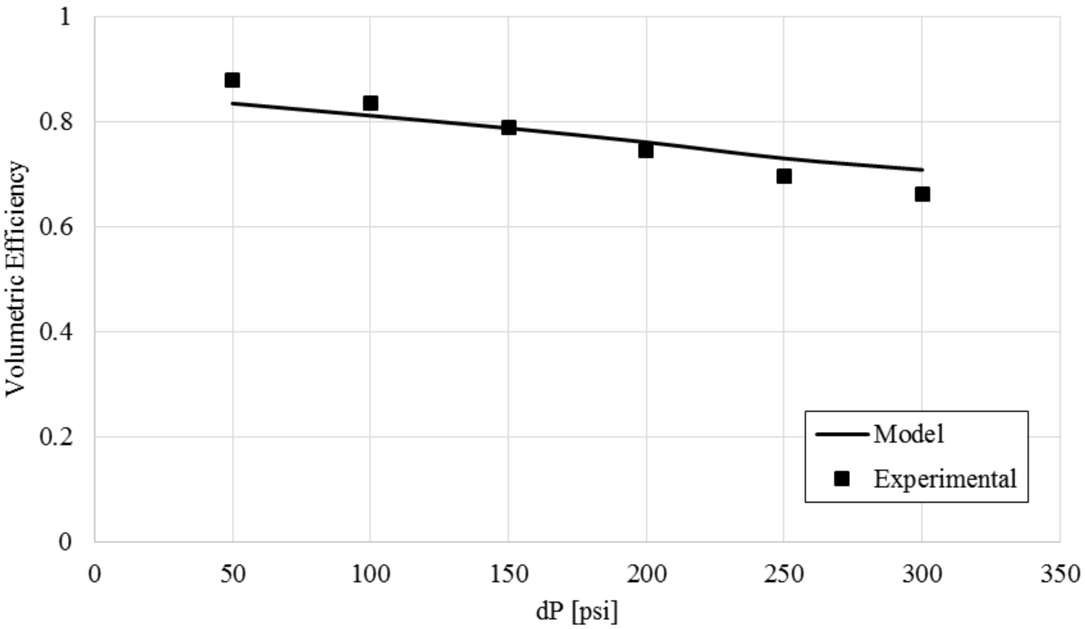

**Figure 4.14.** Pump performance curve averaged across all cases

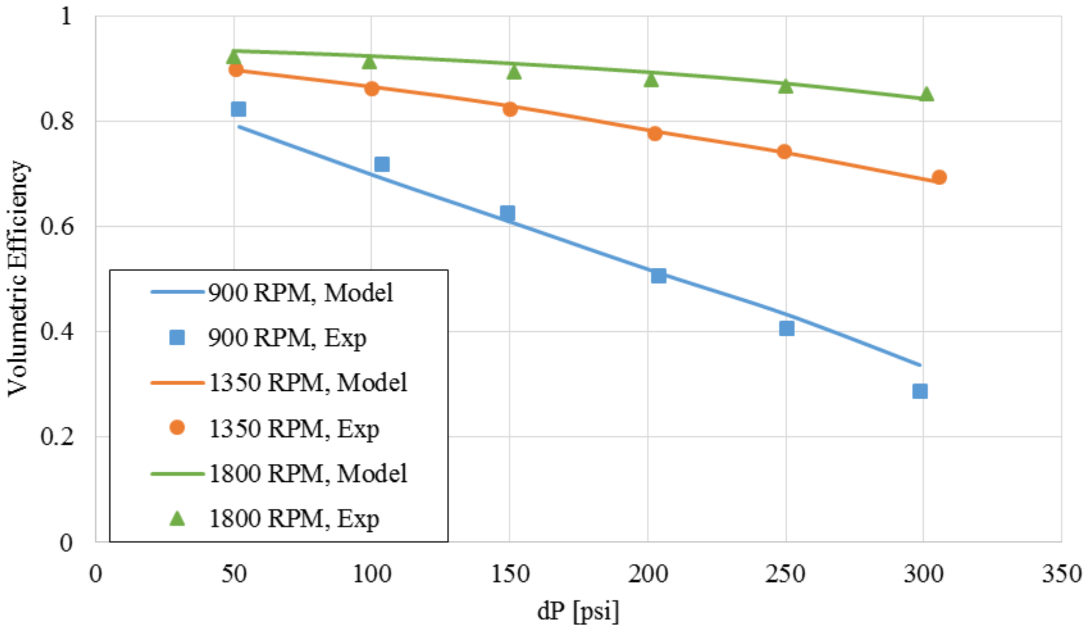

**Figure 4.15.** Pump performance curve for 15 psi suction, 47% GVF, and varying RPM.

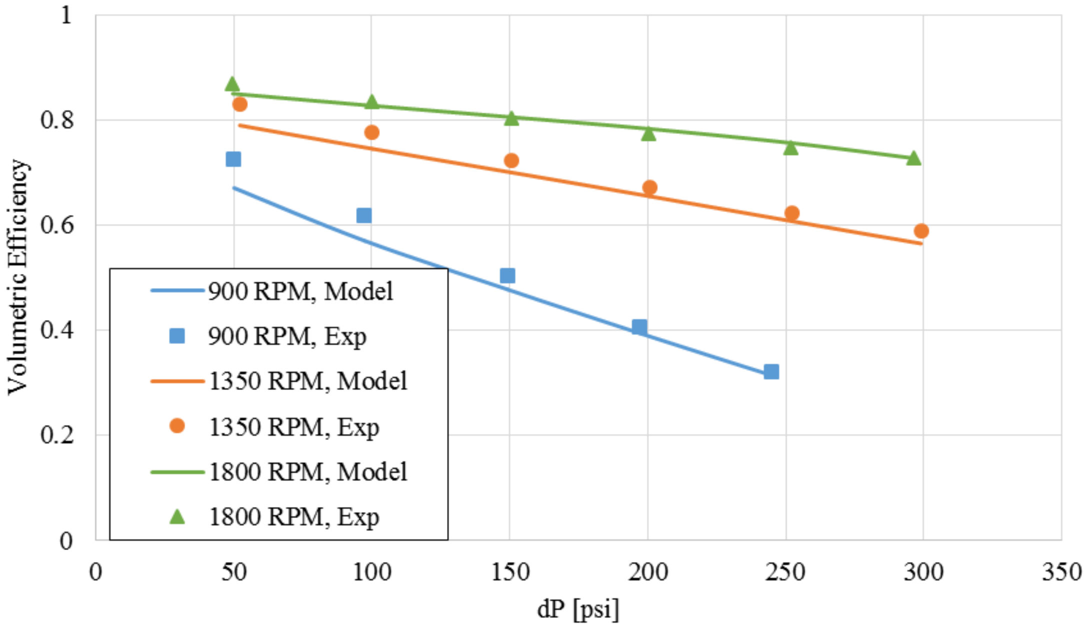

**Figure 4.16.** Pump performance curve for 100 psi suction, 47% GVF, and varying RPM.

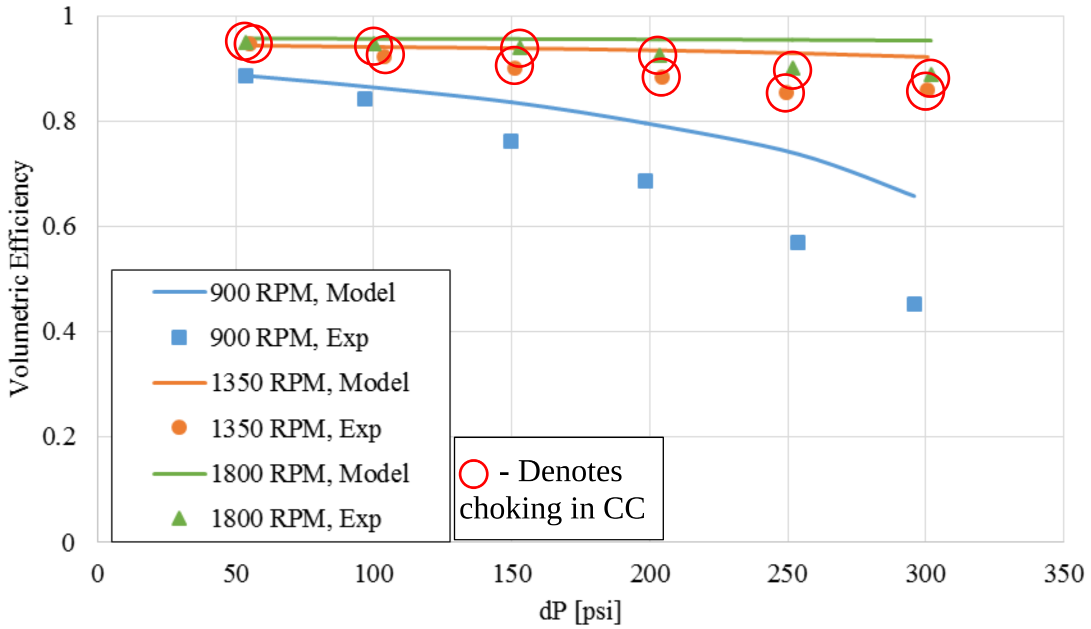

**Figure 4.17.** Pump performance curve for 15 psi suction, 95% GVF, and varying RPM. A red star indicates that choked flow occurs in the circumferential clearance.

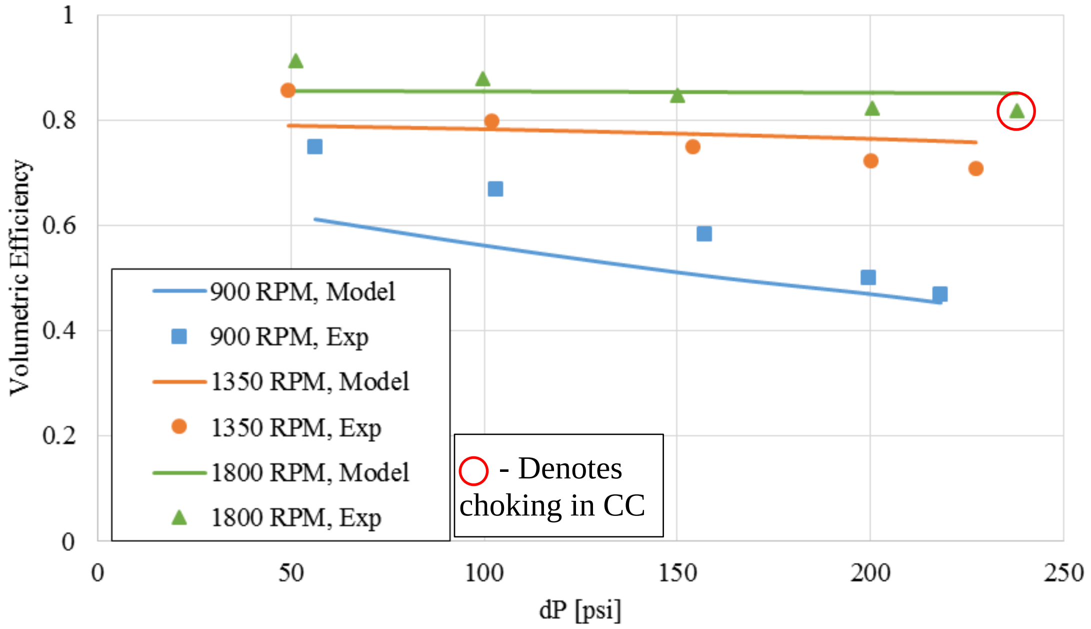

**Figure 4.18.** Pump performance curve for 100 psi suction, 95% GVF, and varying RPM.

Based on the graphs, if pump speed is held constant, changes in the suction pressure or GVF have a relatively minor effect on the slope. Comparing the cases of 47% GVF (Figure 4.15 and Figure 4.16) to 95% GVF (Figure 4.17 and Figure 4.18) at a constant 900 RPM, the graphs show that slopes of the lines are slightly less negative for 95% GVF. Therefore, increases in the head has a smaller negative impact on the efficiency at higher gas volume fractions. However, changes in suction pressure do not seem to affect the slope significantly.

Among these most recent examples, the model predicts choked flow for the cases shown in Figure 4.17 and Figure 4.18. Choking is most likely to occur for high RPM, high GVF, low suction pressure, and high differential pressure. These cases tend to already have high efficiency based on their pressure distributions, so there is not much apparent change in the efficiencies seen in the graphs. The impact of critical flows is discussed in more detail in Section 4.4.

In summary, operating a TSP at high head drastically reduces the performance only if the pump is operating at a low speed. Otherwise, rises in the head only have a small or moderate impact on the pump’s efficiency. Low gas volume fractions will lower the efficiency further. This is partly due to lower compressibility of the mixture, which causes a more linear pressure distribution. At high pressure heads, choked flow is more likely to occur, which marginally improves the volumetric efficiency, but this effect is minor.

### 4.3.2. *Effect of GVF on Performance*

The gas volume fraction affects the volumetric efficiency but to a lesser extent than pump speed or differential pressure. Figures 4.19, 4.20, and 4.21 show efficiency curves for 50 psi suction pressure and varying GVF and RPM. The efficiency is lowest for low GVFs. Based on the experimental data, the efficiency is highest around 85-90% GVF if all other parameters are held constant. Higher than this, the efficiency decreases slightly. This is consistent with the theory from Vetter et al. [3] that the fluid becomes a homogenized foam around 85% GVF. During this regime, the foam does not seal the clearances as well as a liquid-dominated mixture, and the pressure distribution becomes more linear. Although the error is not large, the present model does not capture this effect.

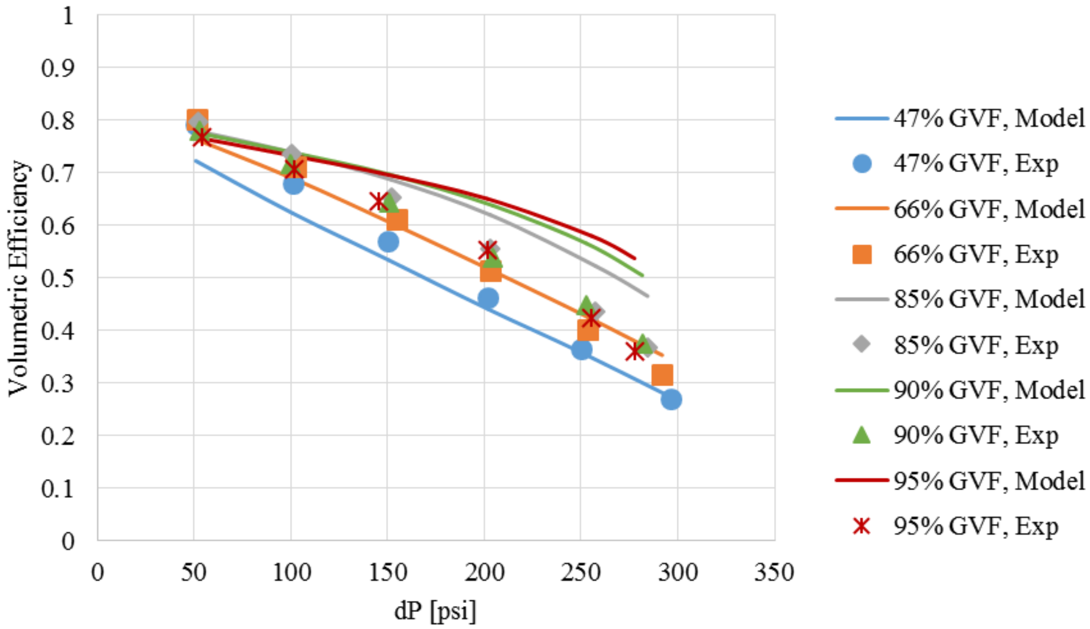

**Figure 4.19.** Pump performance for 50 psi suction and 900 RPM at varying GVFs

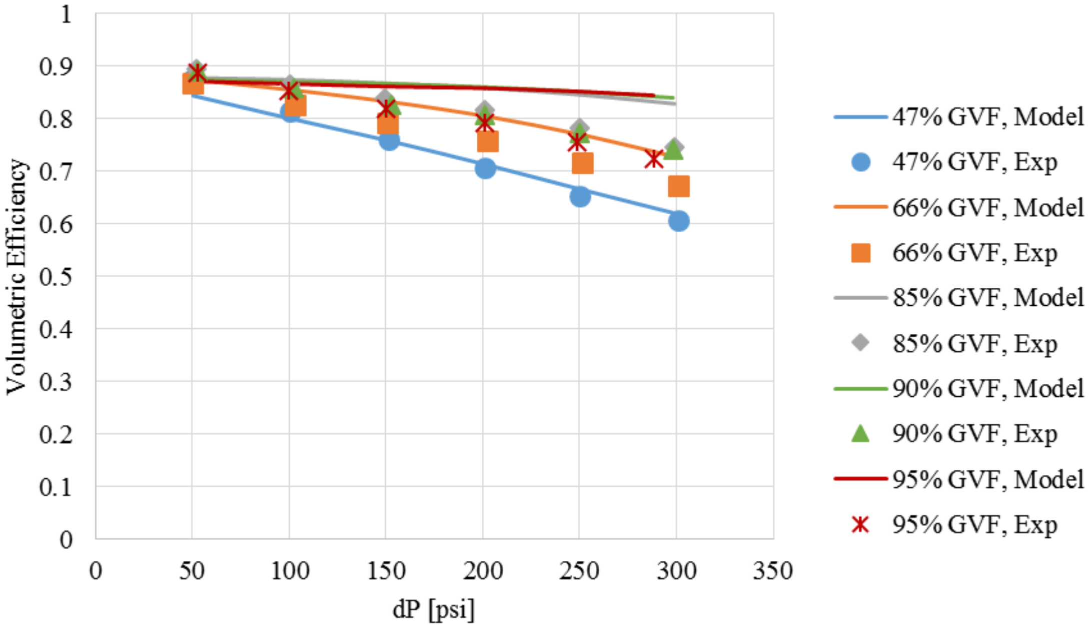

**Figure 4.20.** Pump performance for 50 psi suction and 1350 RPM at varying GVFs

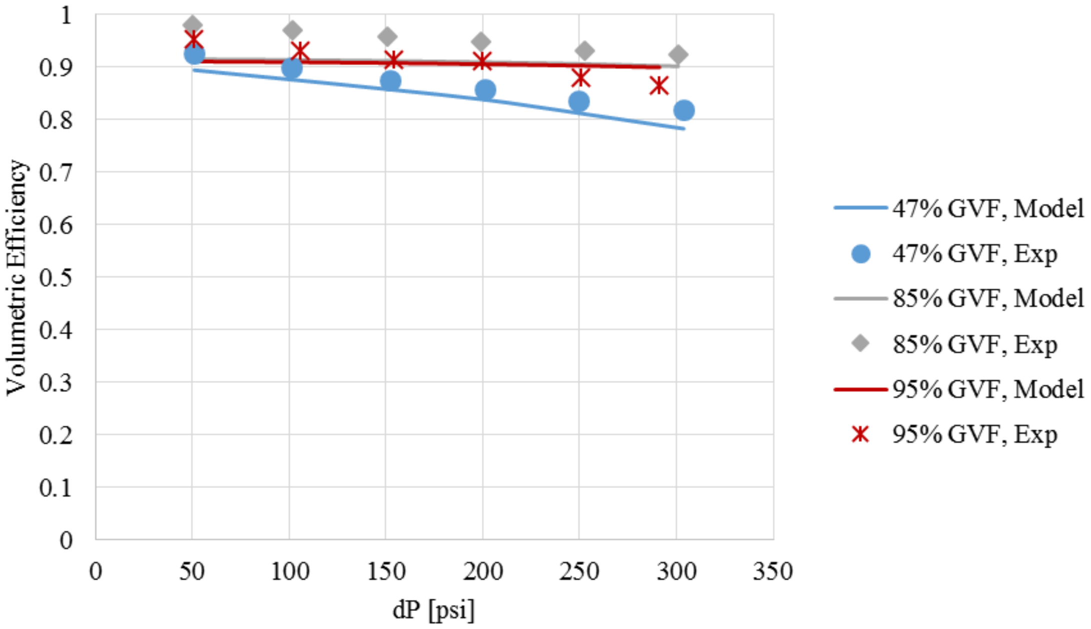

**Figure 4.21.** Pump performance for 50 psi suction and 1800 RPM at varying GVFs

At the 900 and 1350 RPMs, there is a noticeable discrepancy between the predicted efficiencies and the experimental data. For the 85-95% GVF cases, the model overestimates the efficiency significantly. This is directly related to the gas infiltration correlation used in the model, as shown previously in Figure 3.7. The developed correlation is not perfect and could be improved. The data shows that, for chamber GVFs near 85-95%, the estimated GVF that enters the clearance is too low. At high GVFs, the model should predict higher levels of gas that enters the clearance, which would increase the leakage flowrates.

Although high GVF in a clearance increases leakage through that clearance, high GVF at the pump inlet causes an overall increase in the pump's performance. This fact may be somewhat counterintuitive, but it can be explained by the pressure distribution. For pure liquid operation, there is an entirely linear pressure distribution. For each chamber, the leakage flow in equals the leakage flow out. For high GVF operation, each chamber has higher leakage flow in than leakage flow out. This accumulation of mass within the chamber as it is conveyed axially is dependent on the mixture's compressibility. The pressure distribution is concave up as the pressure rises in a conveyed chamber: the largest pressure gradients occur near the discharge, and the smallest pressure gradients occur near the suction. Since the pressure-driving force is smaller at the suction, there will be lower rates of backflow.

At low heads, pump performance remains nearly the same regardless of changes in the gas volume fraction. At high heads, the efficiency fluctuates more as the GVF changes. When there is a larger differential pressure, the compressibility of the fluid becomes more important to the pump's performance. In the graphs shown, the slopes are more negative for lower GVFs.

### *4.3.3. Effect of Pump Speed on Performance*

Higher pump speeds drastically improve performance. At high speeds, the chamber lifetime, $\Delta t_{life}$, is small. There is little time for leakage flow and pressure rises to occur for the chambers near the suction side. As shown previously in Figure 4.12, the pressure distribution at 1800 RPM is very flat initially. Without any pressure gradient between the first chamber and the suction, the only mode of leakage is Couette flow.

Figures 4.22 - 4.25 show how the pump speed affects the performance. At high differential pressures, the drop in performance between 1800 RPM and 1350 RPM is significantly smaller than the drop in performance between 1350 RPM and 900 RPM. This is related to the fact that the chamber lifetime increases by one-third from 1800 RPM to 1350 RPM but by one-half from 1350 RPM to 900 RPM. The residence time within the chambers is directly related to the total backflow. The pump speed is one of the most important factors for efficient performance.

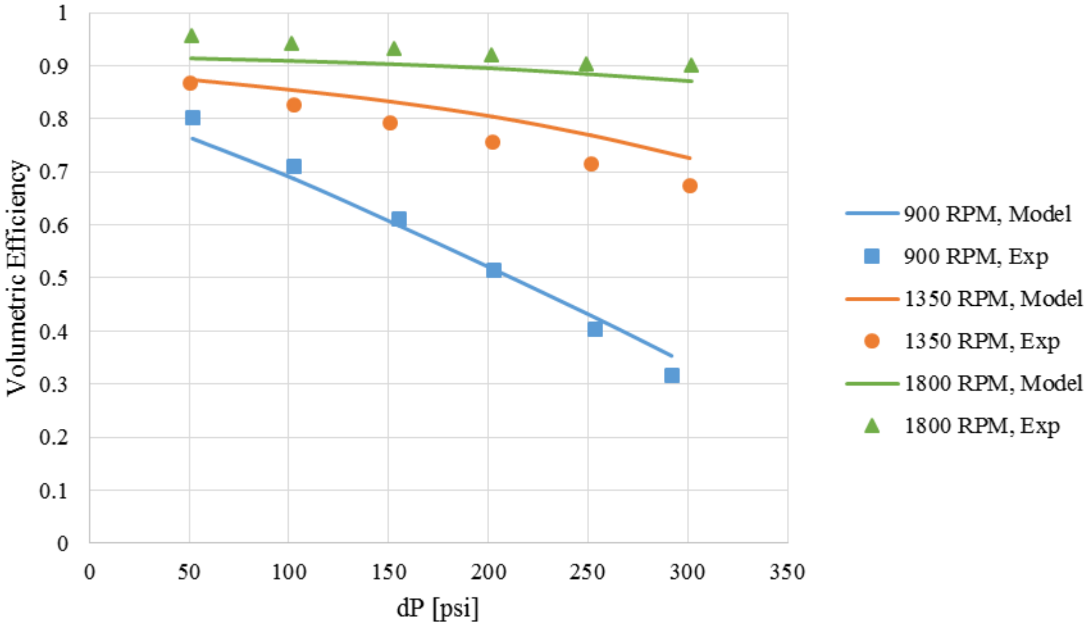

**Figure 4.22.** Pump performance for 50 psi suction and 66% GVF at varying pump speeds

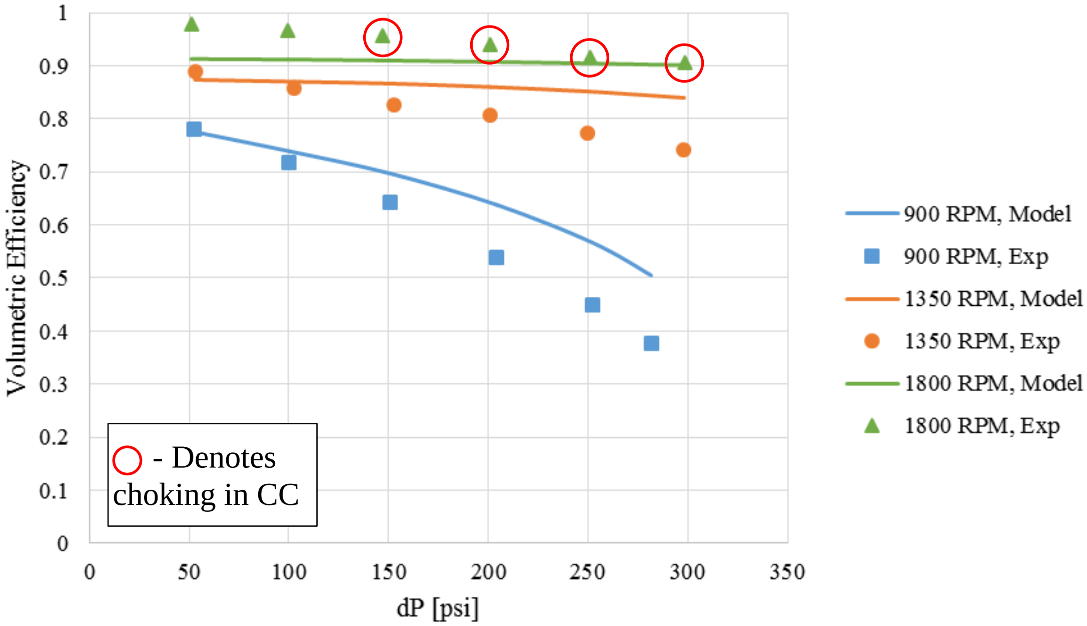

**Figure 4.23.** Pump performance for 50 psi suction and 90% GVF at varying pump speeds

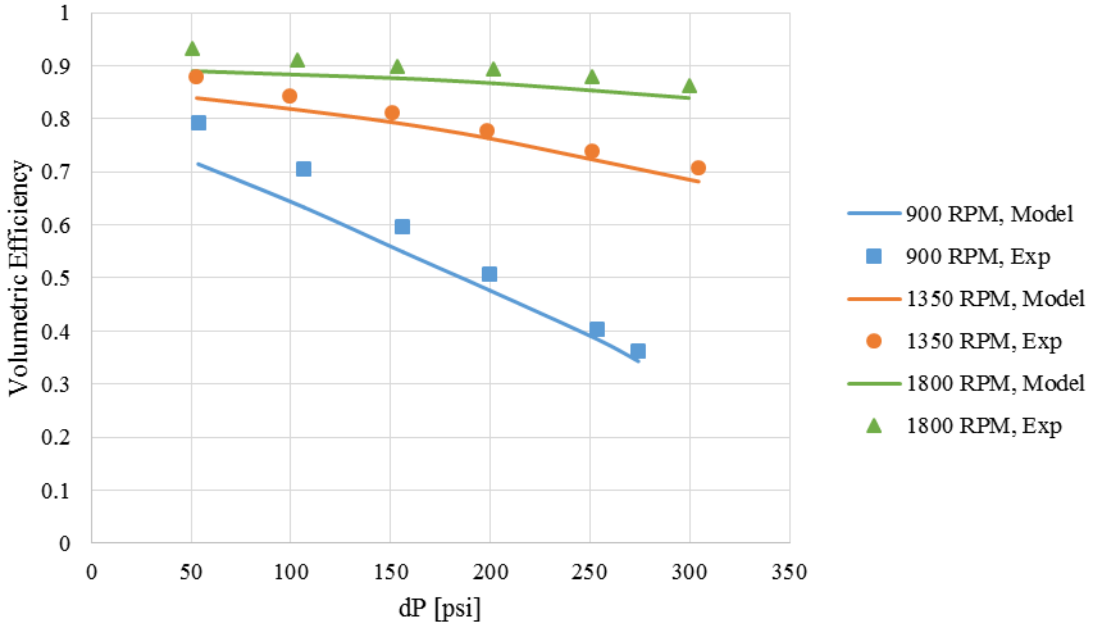

**Figure 4.24.** Pump performance for 75 psi suction and 66% GVF at varying pump speeds

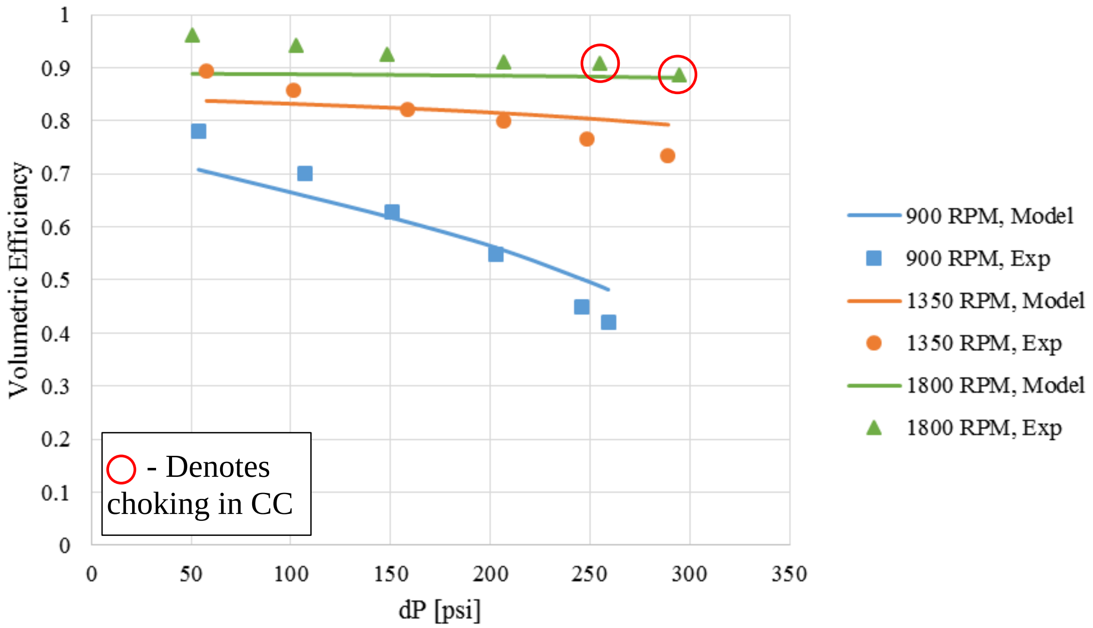

**Figure 4.25.** Pump performance for 75 psi suction and 90% GVF at varying pump speeds

### *4.3.4. Effect of Suction Pressure on Performance*

The suction pressure influences the absolute pressure within the chambers. This affects the compressibility of the gas phase, and, as explained in Section 4.2, higher suction pressures cause the pressure distribution to be more linear. Subsequently, operation at high suction pressures leads to lower efficiency. Figure 4.26 and Figure 4.27 demonstrate these trends. As the suction pressure changes, there does not seem to be a significant change in the shape or slope of the efficiency curve. In these cases, the model shows good agreement with the data.

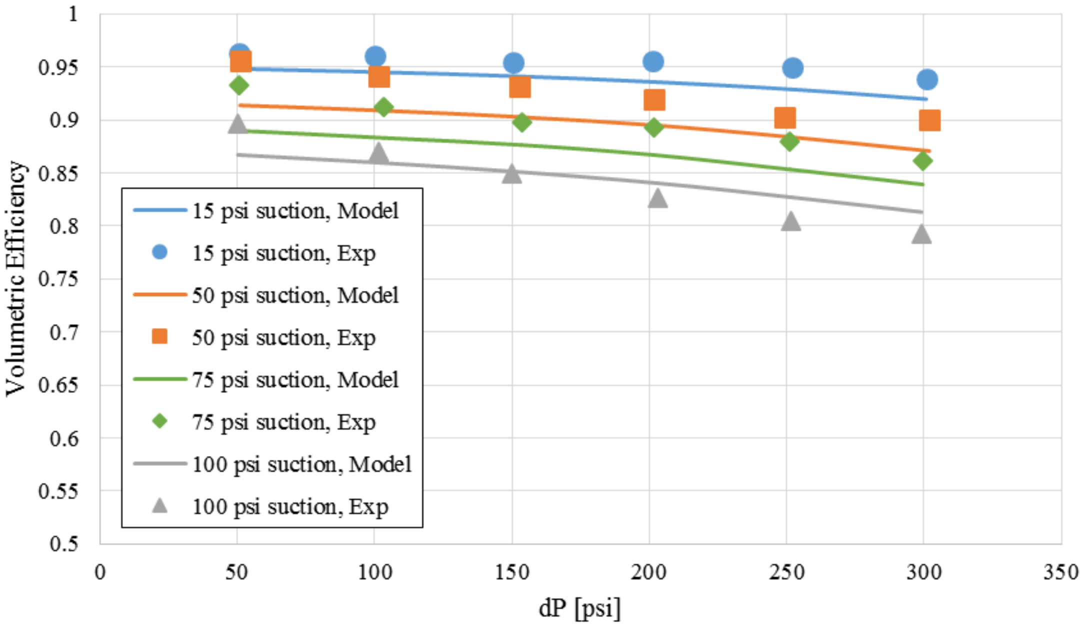

**Figure 4.26.** Pump performance for 1800 RPM and 66% GVF at varying suction pressures

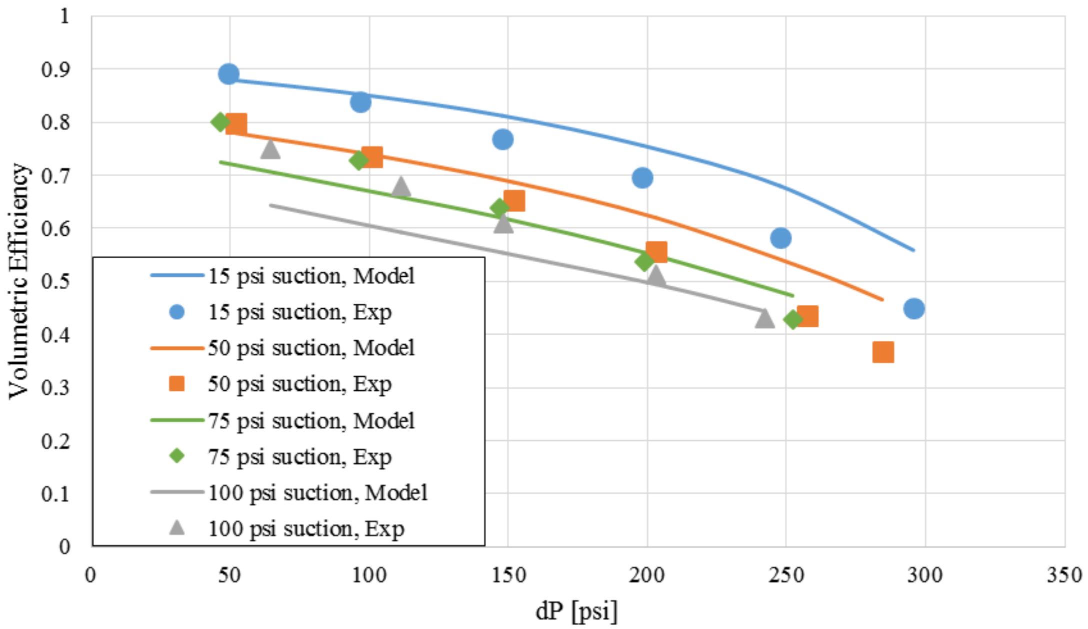

**Figure 4.27.** Pump performance for 900 RPM and 85% GVF at varying suction pressures

## 4.4. Critical Flows

Critical flows occur when there is a large pressure difference between two consecutive chambers. This is most common at high pump heads, high speeds, high GVFs, and low suction pressures. These factors, with the exception of high differential pressures, all improve the performance of the pump by causing a steep pressure gradient near the discharge and a small pressure gradient near the suction. Therefore, choked flows are very likely to occur near the discharge for conditions where the TSP runs very efficiently.

Choked flow through any of the clearances is possible, but it nearly always occurs through the root clearance. In 99% of the test cases, the flow through at least one of the root clearances chokes. This is due to the converging-diverging shape of the gap.

As the fluid accelerates through the root clearance, the pressure drops and reaches the low critical pressure. In contrast, leakage flow through the circumferential and flank clearances choke in 18% and 13% of the test cases, respectively. Specifically, all of these cases with choked flows have pressure distributions with large concavity. The presence of choking in the leakage flow improves the performance of the pump by limiting the backflow between the chambers.

There are a few common trends that occur. A linear pressure distribution will tend to cause choking within the root clearances and no choking within the circumferential and flank clearances. Conversely, a concave pressure distribution will tend to cause choking within the CC and FC but less choking within the root clearances. Figure 4.28 shows the Mach numbers for a few cases. In this figure, the root clearance has a Mach number of 1 throughout each clearance for every case except for 50-100 psi dP. On the other hand, the maximum Mach number for the circumferential and flank clearances remains low, except for the case of 300 psi dP when it is high near the suction and low near the discharge. The reason why this occurs can be understood by looking at the pressure distribution, shown in Figure 4.29, the GVF in each chamber, shown in Figure 4.30, and the speed of sound in each clearance, shown in Figure 4.31. The root clearance, due to its converging-diverging shape, only needs a relatively small pressure gradient to reach critical conditions. When the distribution is linear, then the leakage flow will most likely choke in every one of the root clearances. However, as the pressure gradient becomes more concave, then the root clearance is less likely to choke near the suction side.

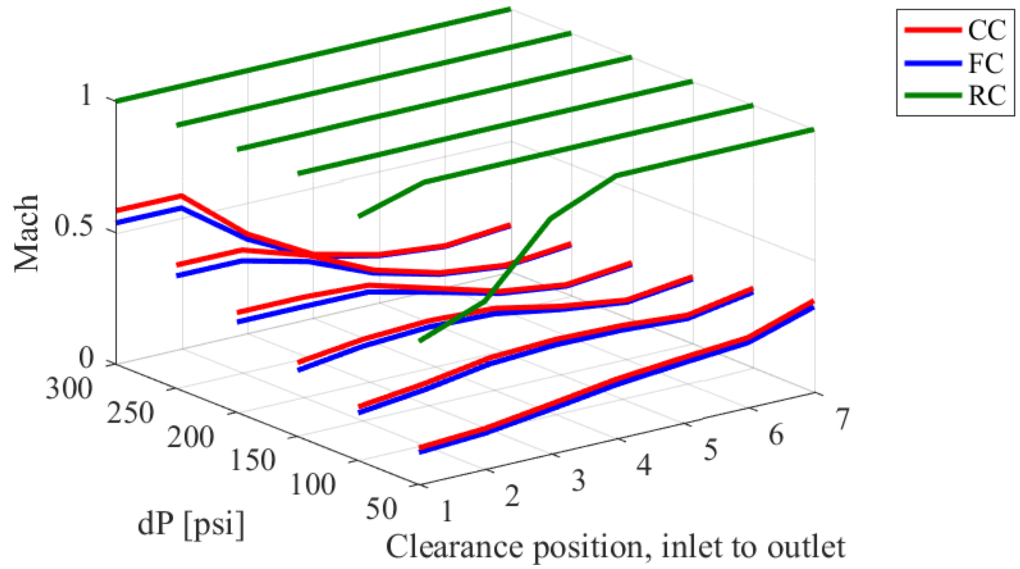

**Figure 4.28.** Maximum Mach numbers reached in each clearance for 15 psi suction, 1350 RPM, and 47% GVF

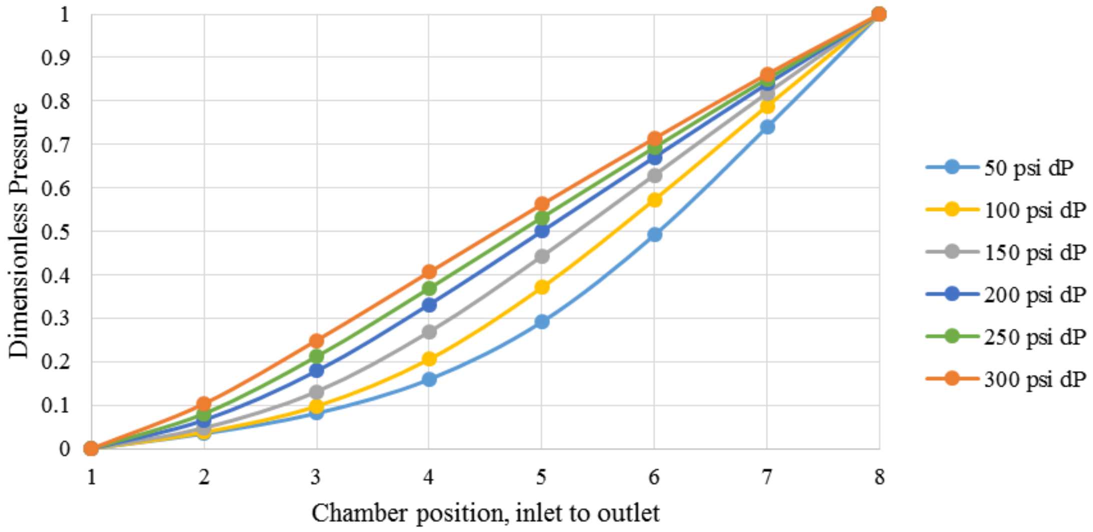

**Figure 4.29.** Pressure distribution for 15 psi suction, 1350 RPM, and 47% GVF

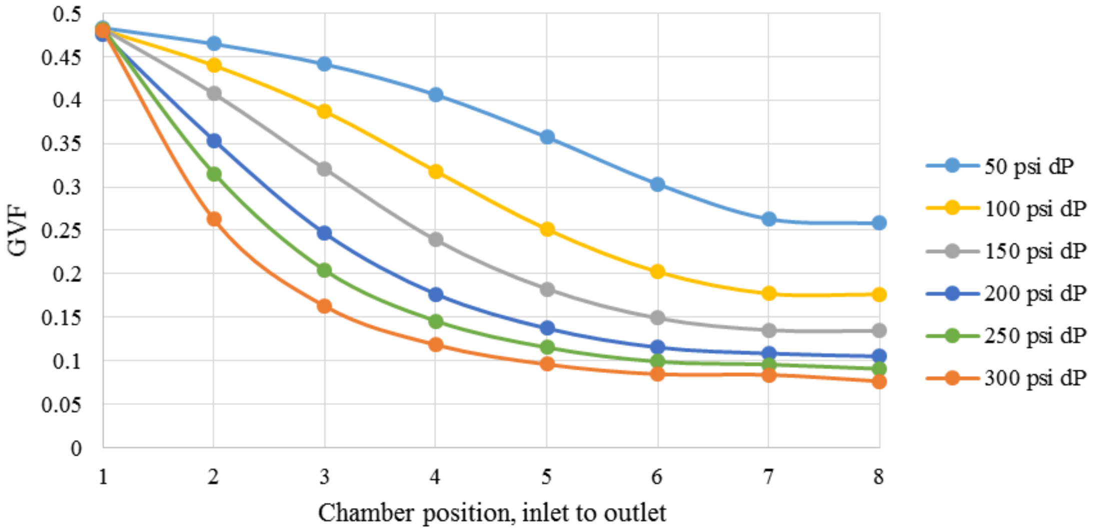

**Figure 4.30.** GVF distribution for 15 psi suction, 1350 RPM, and 47% GVF

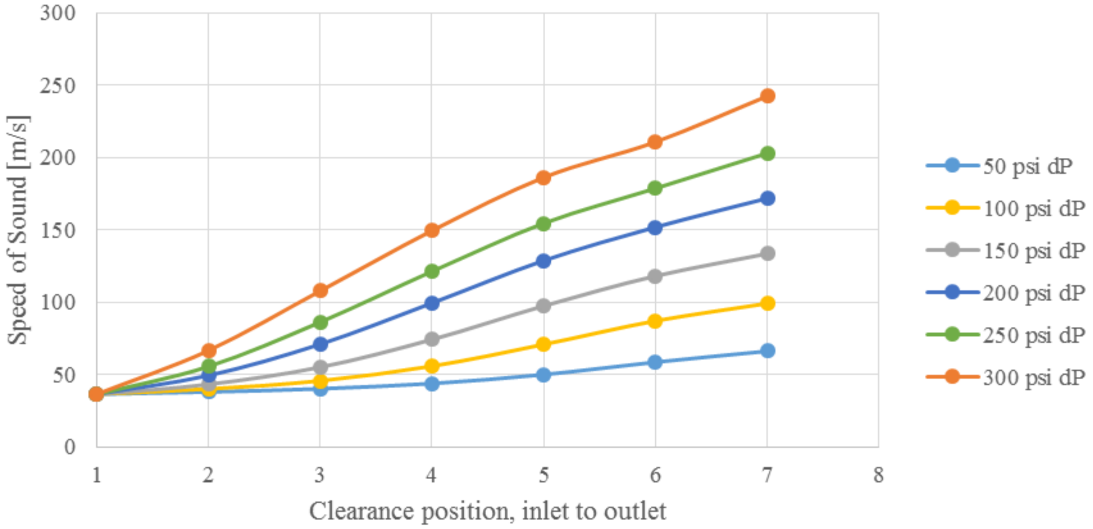

**Figure 4.31.** Speed of Sound in the circumferential clearance for 15 psi suction, 1350 RPM, and 47% GVF

For the circumferential and flank clearances, there are actually a few cases where the Mach number will be high near the pump inlet and decrease along the axial direction. Specifically, this occurs when the pressure distribution is linear. For this pressure distribution, the velocity through each clearance is relatively similar. However, as is usual, the GVF decreases from suction to discharge because of the pressure rise. The GVF has a large effect on the speed of sound of the mixture. As shown in Figure 4.31, the speed of sound increases in the axial direction as GVF decreases. Therefore, the phenomena exists such that the Mach number of leakage in the CC and FC is high at the inlet and decreases closer to the discharge.

However, the critical conditions for the CC and FC are more relevant to the pump's performance. This occurs when there is a very large pressure gradient, and very large pressure gradients would only exist near the discharge. Figure 4.32 shows the maximum Mach number reached in each clearance for the case of 75 psi suction, 1800 RPM, and 90% GVF. Figure 4.33 shows the corresponding pressure distribution. The circumferential clearance reaches choking conditions for 200-300 psi dP. Although the shape of the pressure distribution is nearly the same for most of the cases in the figure, the absolute pressure gradient is not large enough in the cases with lower differential pressure.

However overall, the effects of critical flow seem to be minor. Choking within the circumferential and flank clearances occurs most commonly during optimal operating conditions. The presence of choked flow further improves the efficiency, but the effect will be relatively insignificant.

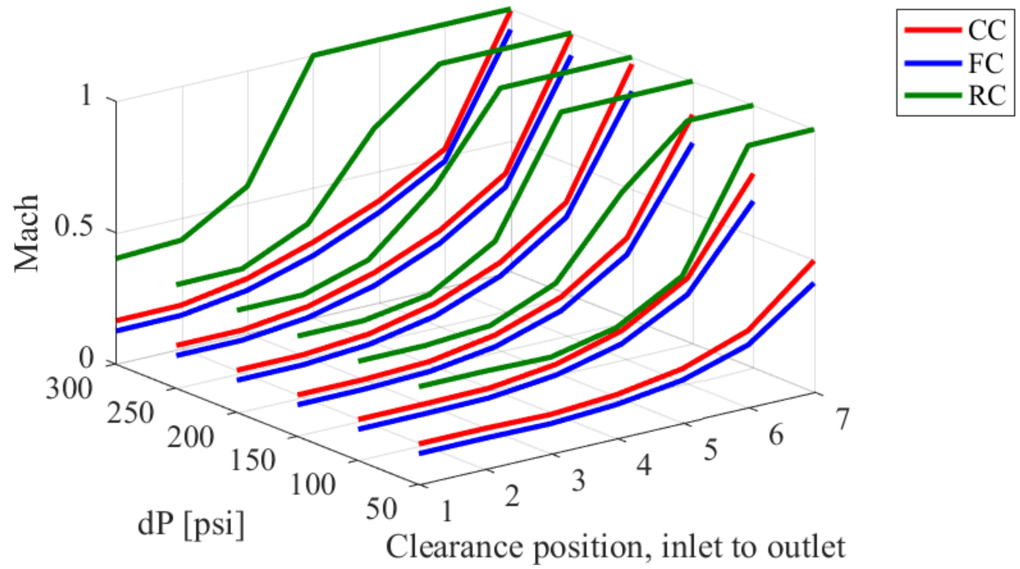

**Figure 4.32.** Maximum Mach numbers reached in each clearance for 75 psi suction, 1800 RPM, and 90% GVF

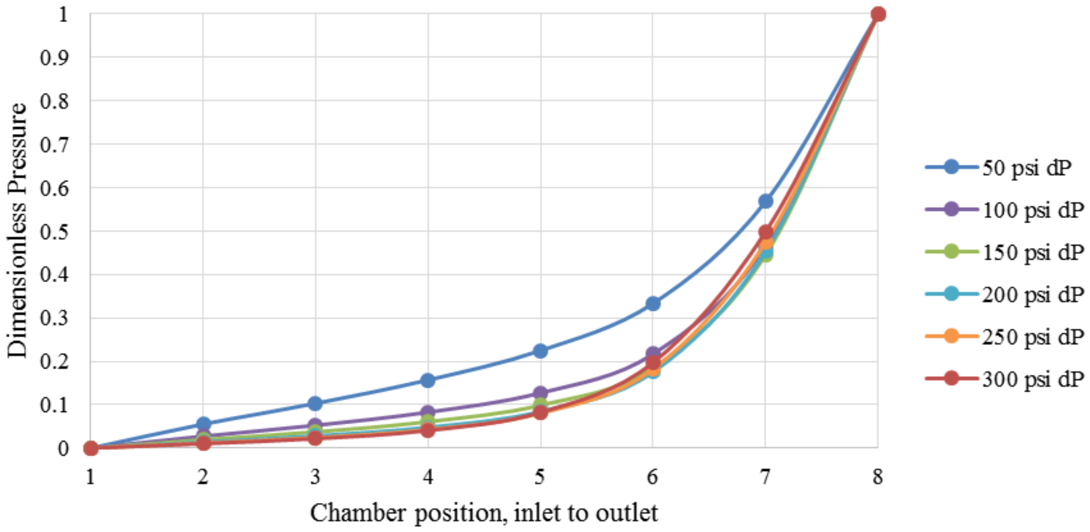

**Figure 4.33.** Pressure distribution for 75 psi suction, 1800 RPM, and 90% GVF

## 4.5. Eccentricity Effects

The decrease in efficiency due to the eccentricity effects is most prominent when operating with high pressure heads. The hydraulic imbalance in the radial direction is larger, and consequently the spindle deflection is greater. The total cross-sectional area of the circumferential gap increases when the spindle is off-centered. The rotor bending would not affect the flank clearance, but it would decrease the size of the root clearance. The pressures near the root clearances are low since fluid accelerates through the converging-diverging gap, and the pressures in the chambers on the opposite side of the rotors are relatively higher. Therefore, the net hydraulic forces push the rotors together. However, this aspect of the rotor deflection is neglected since the proportion of leakage that occurs through the root clearance is very small. The increase in leakage flowrate due to the change in geometry is also compounded by the high differential pressure that further increases the leakage flowrates.

The eccentricity is only dependent on the differential pressure. Because the pump that is focused in this study is double-ended with discharge in the middle, the highest value for the ratio of eccentricity will occur near the discharge, as shown in Figure 4.34. In addition, the largest pressure gradient commonly occurs near the discharge, so there is relatively more leakage at the last clearance. As the ratio of eccentricity increases, the leakage flowrate increases according to Equations (3.48) and (3.49) depending on whether the flow is laminar or turbulent. These equations are graphed out in Figure 4.35. Combining the two previous figures results in Figure 4.36.

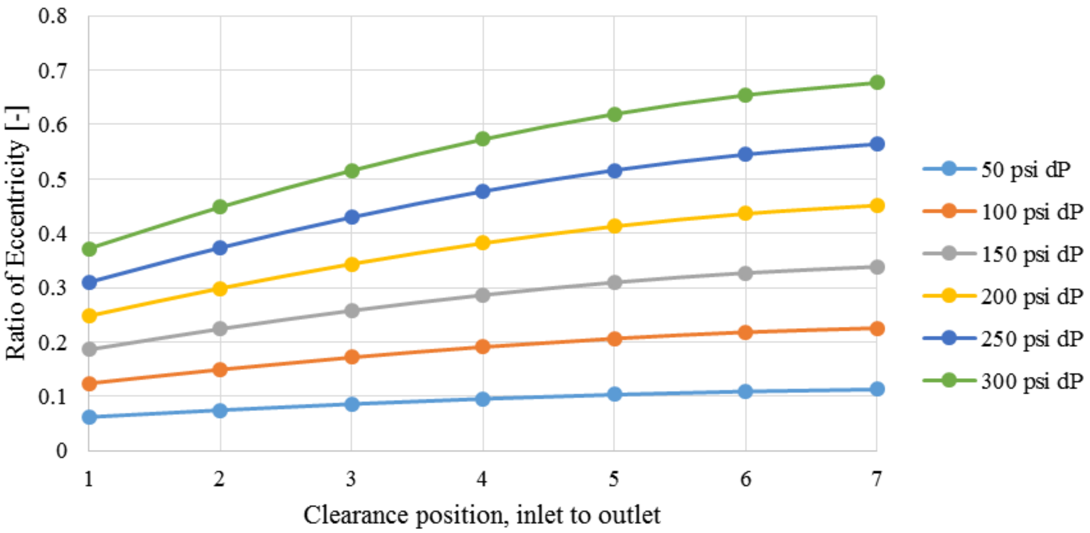

**Figure 4.34.** Ratio of eccentricity at each clearance position for varying differential pressures

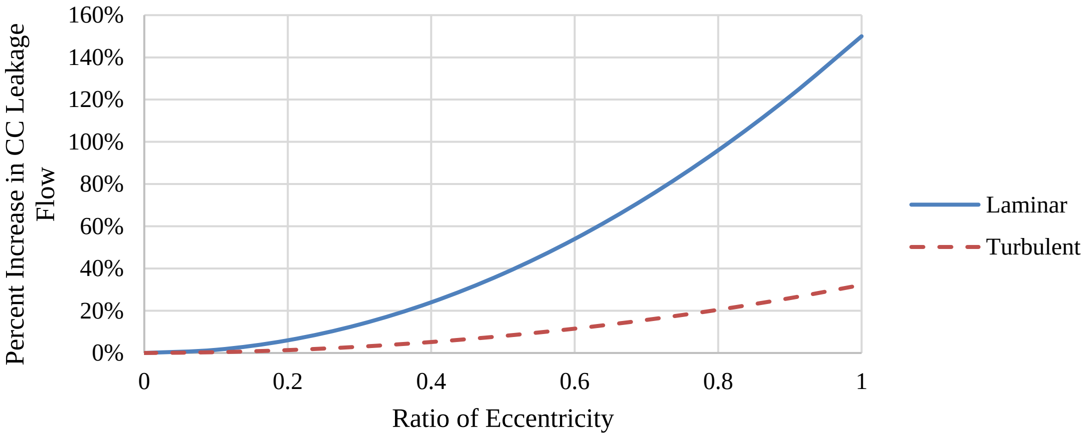

**Figure 4.35.** Increase in circumferential leakage flowrate vs. ratio of eccentricity

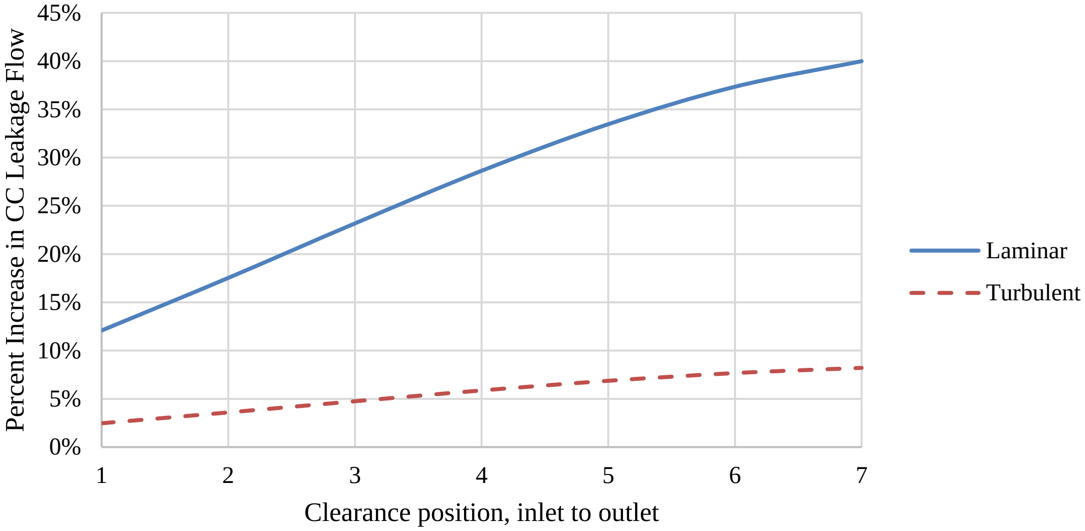

**Figure 4.36.** Increase in circumferential leakage flowrate vs. axial direction for 300 psi differential pressure

For the purposes of calculating volumetric efficiency, the leakage flow through the first clearance is the most important. This leakage flow is generally turbulent, but it is laminar in almost 25% of the cases. The flow is more likely to be laminar when there is only a small pressure gradient across the first lock. This condition coincides with a concave pressure distribution and high volumetric efficiency. Explicitly, the leakage flow through the first circumferential clearance is more likely to be laminar when there is low suction pressure, low differential pressure, high GVF, and high RPM. Although laminar regime increases the relative leakage due to rotor deflection, overall the effect is generally small because the presence of laminar flow means that the velocity, and thus leakage flowrates, are already low.

Figures 4.37–4.40 show the effects of rotor deflection on the volumetric

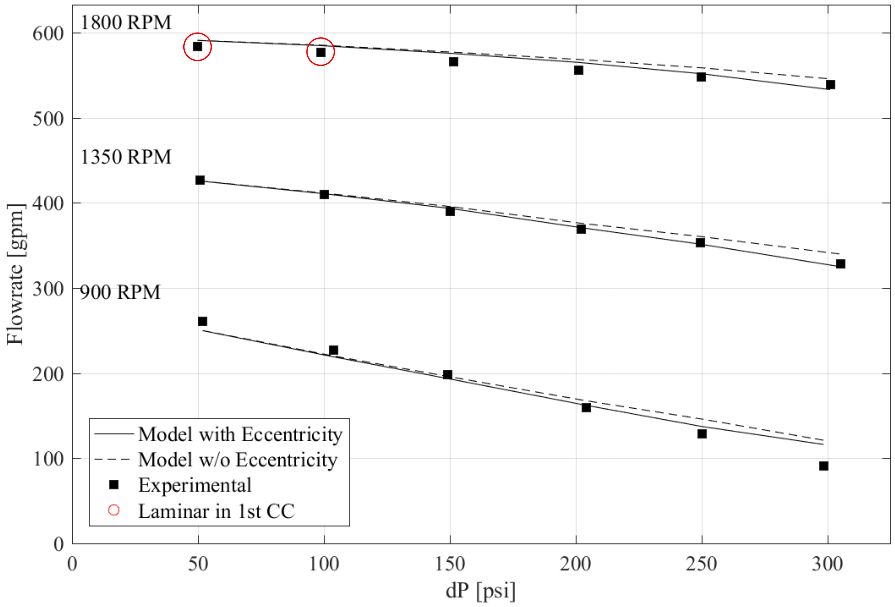

**Figure 4.37.** Effects of eccentricity on performance curves for 15 psi suction pressure and 47% GVF

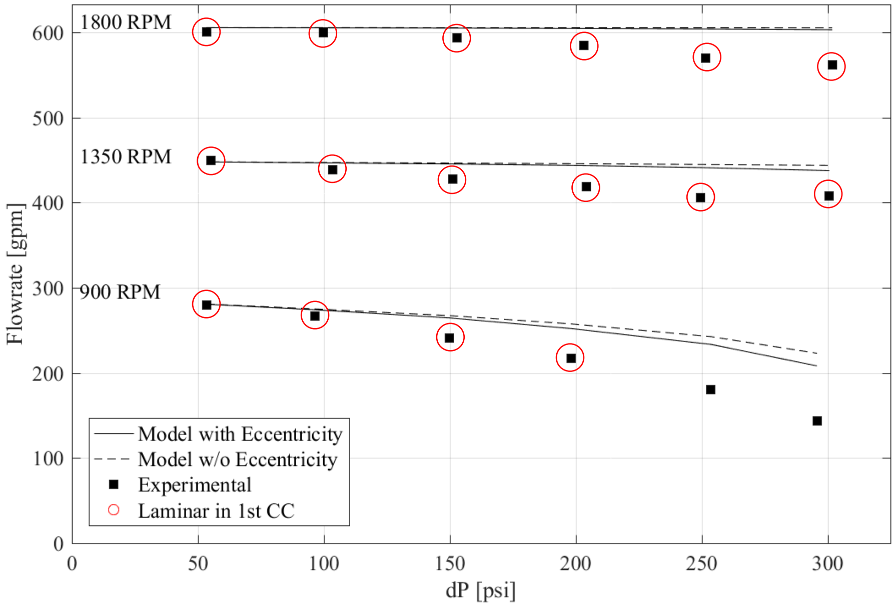

**Figure 4.38.** Effects of eccentricity on performance curves for 15 psi suction pressure and 95% GVF

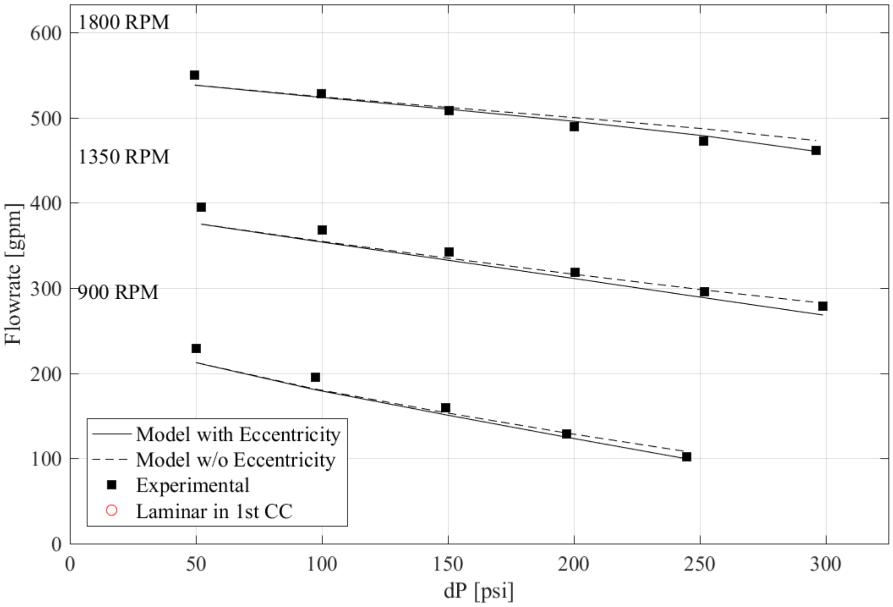

**Figure 4.39.** Effects of eccentricity on performance curves for 100 psi suction pressure and 47% GVF

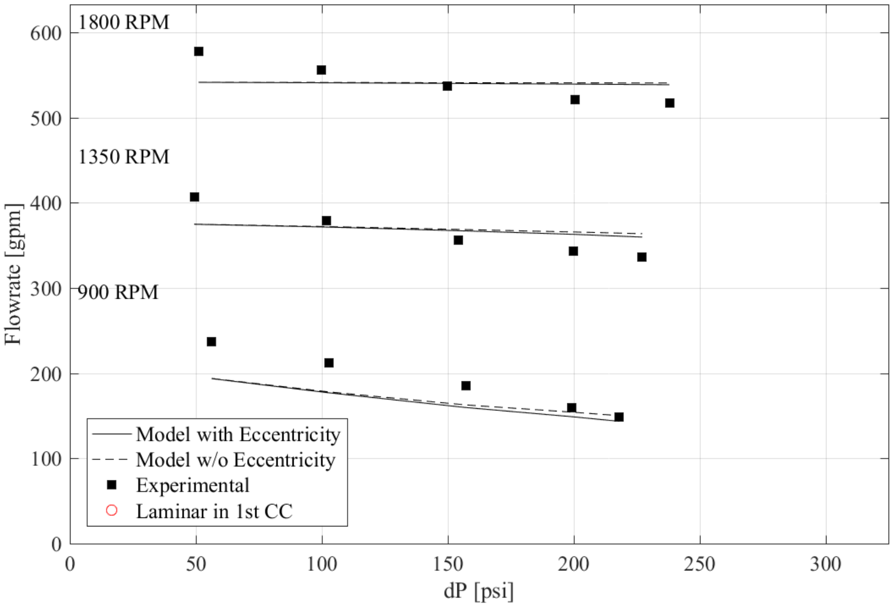

**Figure 4.40.** Effects of eccentricity on performance curves for 100 psi suction pressure and 95% GVF

flowrate predictions.  Red circles denote that the leakage flow through the first circumferential clearance is laminar.  Overall, the eccentricity effects are relatively small, but incorporating them into the model improves the predictions.  On average, the incorporation of the rotor deflection decreases the predicted volumetric efficiency by 1%.  The conditions where the effect is largest is shown in Figure 4.38, for 15 psi suction pressure, 300 psi differential pressure, 900 RPM, and 95% GVF.  For this case, the present model predicts a 5% lower efficiency compared to if the model does not factor in eccentricity.  This change of 5% efficiency translates to a decrease in relative error of 10.7% by factoring in eccentricity.  Although in most cases, eccentricity effects are not significant, there are a few conditions, such as this one, where including them in the model is important.

Laminar leakage flow is most common at 15 psi suction pressure, and it does not occur for the cases where the suction pressure is 75 psi or greater.  As shown in the examples in Figure 4.37 and Figure 4.38, the flow regime does not seem to have a significant influence on the eccentricity effects.  Although there is a higher relative increase in leakage flow for laminar flow, the effect on efficiency is not significant because the leakage flowrates are lower for those conditions than for the conditions where the flow is turbulent.

## 4.6. Circumferential, Flank, and Root Clearance Analysis

The pressure-driven component of the leakage flow is highly dependent on the pressure distribution.  As discussed in Section 4.2, each of the input parameters have a significant effect on the distribution. More concave pressure distributions will lead to lower pressure-driven leakage flowrates at the pump inlet and larger pressure-driven leakage flowrates near the discharge. Near the discharge, the pressure gradient may be large enough to cause choked flow.

While every parameter affects the pressure-driven flow, the Couette flow is only dependent on the pump speed. The Couette flow component is generally smaller than the pressure-driven component. The circumferential clearance flow contributes the most to the total leakage flowrate, and it is dominated by the pressure-driven flow. The flank leakage is smaller and more dependent on the Couette flow. The leakage through the radial clearance also depends on Couette flow.

Ultimately, the determining factor of how the proportions of leakage flowrates relate to each other is the pressure distribution. Examples of linear, moderately concave, and sharply concave pressure distributions are shown in Figures 4.41, 4.42, and 4.43. In general, the flow through the circumferential is largest, and it is more dominant near the discharge where there tends to be a larger pressure gradient. Flow through the flank clearance accounts for around 15-20%. On average, the proportion of leakage through the flank clearance is greatest near the suction because it is less dependent on the pressure gradient relative to the circumferential leakage flow. Flow through the root clearance accounts for less than 5%. Due to small throat in the channel, the flow is choked in the majority of situations.

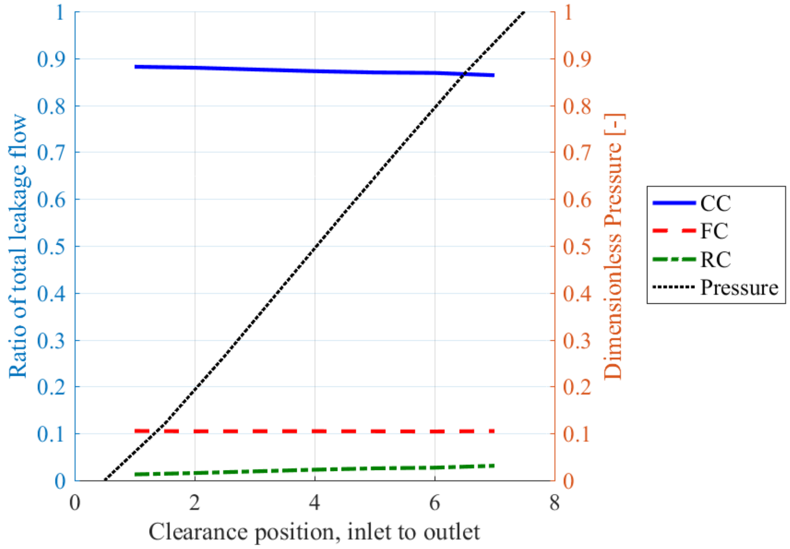

**Figure 4.41.** Proportion of leakage through each clearance for 15 psi suction, 900 RPM, 66% GVF, and 248 psi dP

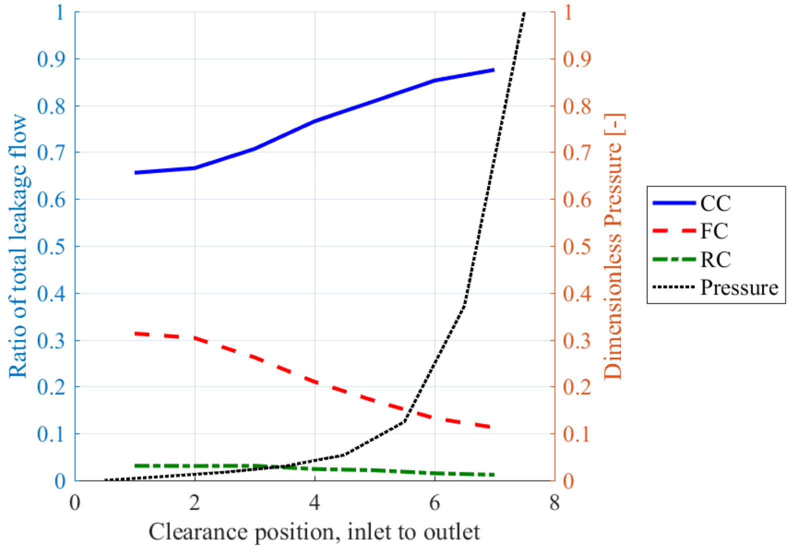

**Figure 4.42.** Proportion of leakage through each clearance for 15 psi suction, 1350 RPM, 85% GVF, and 53 psi dP

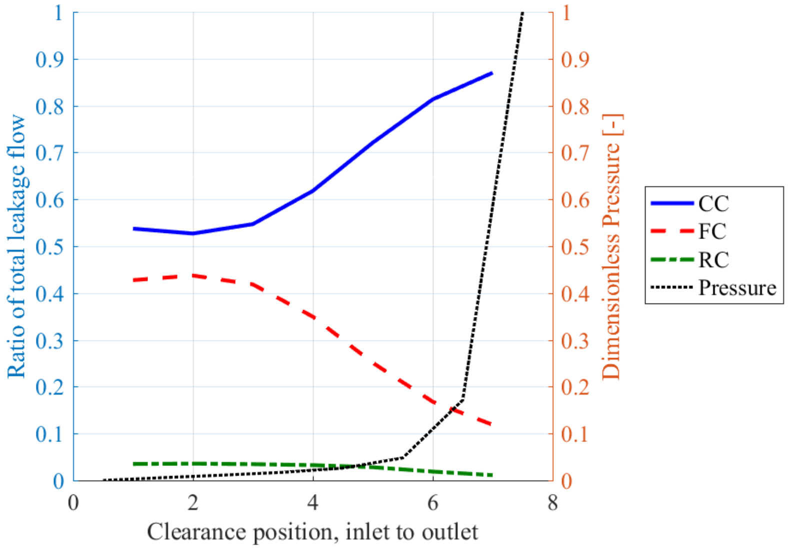

**Figure 4.43.** Proportion of leakage through each clearance for 15 psi suction, 1800 RPM, 93% GVF, and 50 psi dP

For an extremely concave pressure distribution as shown in Figure 4.43, the contribution from the circumferential clearance is nearly equal to the contribution from the flank clearance. This is because the pressure gradient is really small near the inlet, and the Couette flow component dominates. For the circumferential clearance, the contribution from Couette flow is negligible because the walls move nearly perpendicularly to the direction of the leakage flow. On the other hand, the movement of the flank clearance walls have a larger effect because they travel in the same direction as the leakage flow. At the discharge end, there is a large pressure gradient, and the circumferential leakage flow dominates once again.

The effects that the input parameters have on the proportions of leakage through each clearance is directly related to the pressure distribution. Therefore, the following conditions can increase the relative importance of the flank clearance:

- Low suction pressure
- High pump speed
- High GVF
- Low differential pressure

The combination of these conditions occurs in the previous example from Figure 4.43. The conditions also slightly increase the relative proportion of leakage going through the root clearance, but it remains extremely small due to choking.

# 5. CONCLUSION

In this research, an analytical model has been developed to predict the performance of multiphase twin screw pumps. The key features incorporated into the model are two-phase compressible flow, the presence of critical flows, and eccentric spindle rotation due to hydraulic imbalance. The model was validated with experimental data from a Colfax MR-200 twin screw pump. The model shows good agreement in most of the test cases. However, the model is slightly less accurate at low, off-design pump speeds.

Four important parameters that affect the pump operation are suction pressure, pump speed, GVF, and differential pressure. In general, the volumetric efficiency increases with any of the following:

- Decrease in suction pressure
- Increase in pump speed
- Increase in GVF
- Decrease in differential pressure

The performance of TSPs is strongly dependent on the pressure distribution across the pump. Cases where the pressure distribution is linear tend to have lower volumetric efficiency compared to cases where most of the pressure rise occurs across the last few screw teeth near the discharge.

The model was used as a tool to identify flow behavior and phenomena during TSP operation. Choked flow, which improves volumetric efficiency, commonly occurs within the root clearance due to its converging-diverging shape. It happens less frequently for the circumferential and flank clearances, and when it does, the TSP is already operating under efficient conditions. The effect of eccentric rotation decreases the efficiency of TSPs, especially at high differential pressures. This effect leads to decreases in performance by less than 5%. The ratio of leakage flow through each of the clearances is dependent on the pressure profile. On average, 80%, 18%, and 2% of the leakage goes through the circumferential, flank, and root clearances, respectively. For linear pressure distributions, proportionally more leakage goes through circumferential clearance. For very concave pressure distributions, the proportion of leakage through the flank clearance increases, but the circumferential clearance remains dominant. Leakage through the root clearance always is small due to choked flow. In conclusion, the present model showed good reliability with experimental data, and it was useful for discovering relationships among operating conditions and pump performance.

The present model tries to predict TSP performance in an analytical, accurate, and robust way, but there are still many areas for future research. TSP operation at low pump speeds has not been tested extensively. Many aspects of the flow behavior change at lower speeds, such as the rates of gas infiltration into the clearances. While operators would not usually use a twin screw pump at lower speeds due to the drastic drop in performance, research in this area can provide valuable insight in the flow behavior. Specifically, more universal correlations should be developed to predict the level of gas infiltration that occurs with varying chamber GVF and pump speed. There may also be other factors that affect this, such as the suction pressure, differential pressure, and compressibility and density of the mixture.

# REFERENCES

[1] U.S. Energy Information Administration, 2016, "International Energy Outlook 2016," Washington, DC.

[2] Morrison, G., Pirouspanah, S., Kirkland, K., Scott, S. L., and Barrios, L. J., 2014, "Performance Evaluation of a Multiphase Electric Submersible Pump," Offshore Technology Conference, Houston, TX.

[3] Vetter, G., Wirth, W., Körner, H., and Pregler, S., "Multiphase Pumping with Twin-Screw Pumps--Understand and Model Hydrodynamics and Hydroabrasive Wear," Proc. International Pump Users Symposium, pp. 153-170.

[4] Gonzalez, R., and Guevara, E., 1995, "Economic Field Development in Venezuela Heavy Oil Fields Using Multiphase Pumping Technology," International Heavy Oil Symposium, Society of Petroleum Engineers, Calgary, Alberta, Canada, pp. 195-201.

[5] Liu, P., 2016, "Performance Evaluation and Modeling of Twin Screw Pumps," Doctor of Philosophy Dissertation, Texas A&M University, College Station, TX.

[6] Patil, A., 2013, "Performance Evaluation and CFD Simulation of Multiphase Twin-Screw Pumps," Doctor of Philosophy Dissertation, Texas A&M University.

[7] Räbiger, K., 2009, "Fluid Dynamic and Thermodynamic Behaviour of Multiphase Screw Pumps Handling Gas-Liquid Mixtures with Very High Gas Volume Fractions," Doctor of Philosophy Dissertation, University of Glamorgan.

[8] Vetter, G., and Wincek, M., 1993, "Performance Prediction of Twin Screw Pumps for Two-Phase Gas/Liquid Flow," Pumping Machinery, FED-154, pp. 331-340.

[9] Prang, A. J., and Cooper, P., "Enhanced Multiphase Flow Predictions in Twin-Screw Pumps," Proc. International Pump Users Symposium, pp. 69-76.

[10] Nakashima, C. Y., Oliveira Jr., S., and Caetano, E. F., "Thermo-Hydraulic Model of a Twin-Screw Multiphase Pump," Proc. International Mechanical Engineering Congress and Exposition, ASME, pp. 251-260.

[11] Muhammad, A. R. A., 2013, "Rotordynamics of Twin Screw Pumps," Doctor of Philosophy Dissertation, Texas A&M University.

[12] Hirs, G. G., 1973, "A Bulk-Flow Theory for Turbulence in Lubricant Films," Journal of Lubrication Technology, p. 9.

[13] Brennen, C. E., 2005, Fundamentals of Multiphase Flows, Cambridge University Press.

[14] Young, F. M., 1993, "Generalized One-Dimensional, Steady, Compressible Flow," AIAA Journal, 31(1), pp. 204-208.

[15] Munson, B. R., Okiishi, T. H., Huebsch, W. W., and Rothmayer, A. P., 2013, Fundamentals of Fluid Mechanics, Wiley.

# APPENDIX

## A.1. Volumetric Efficiency vs. Differential Pressure Graphs

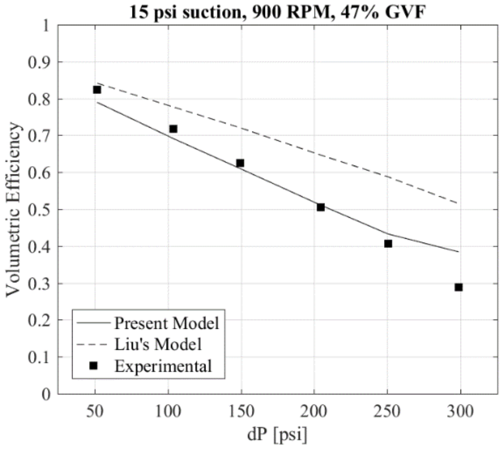
15 psi suction, 900 RPM, 47% GVF

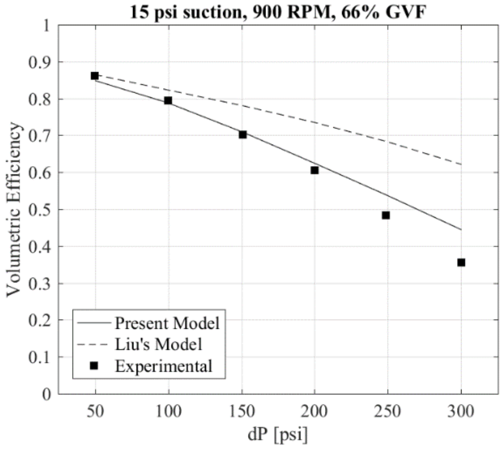
15 psi suction, 900 RPM, 66% GVF

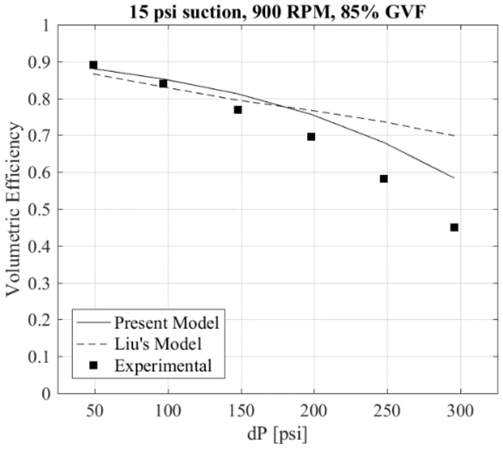
15 psi suction, 900 RPM, 85% GVF

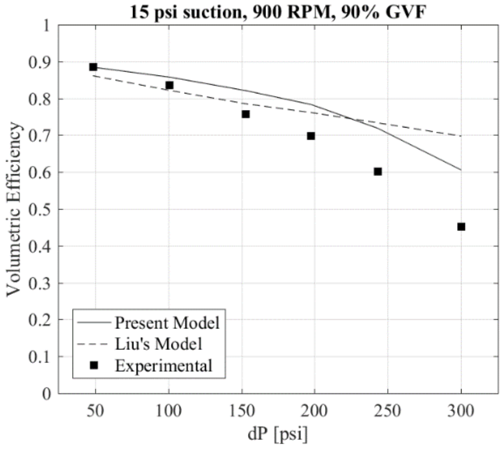
15 psi suction, 900 RPM, 90% GVF

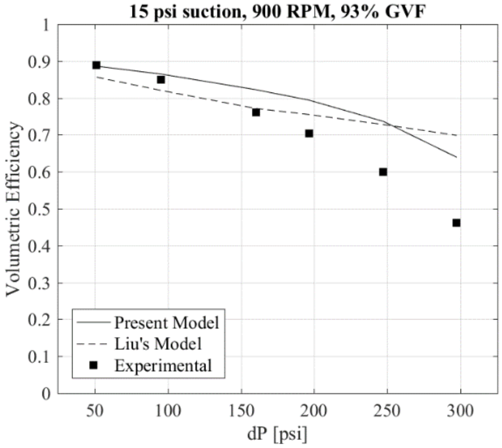
15 psi suction, 900 RPM, 93% GVF

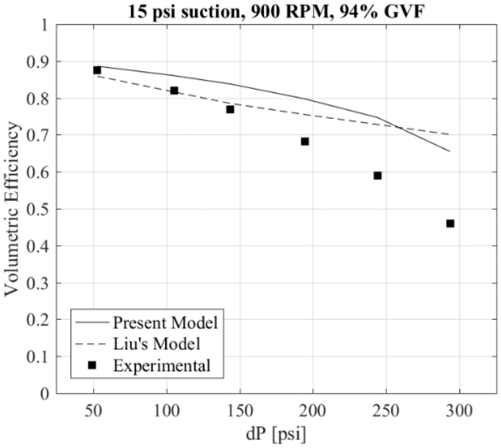
15 psi suction, 900 RPM, 94% GVF

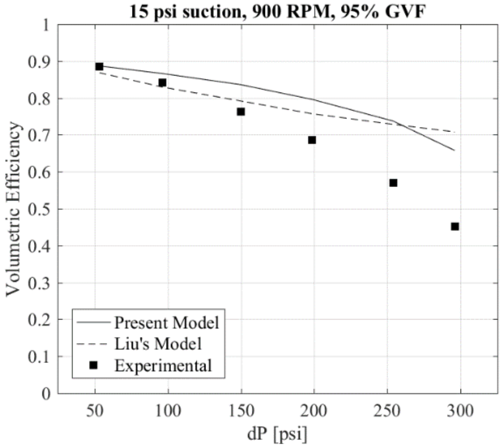
15 psi suction, 900 RPM, 95% GVF

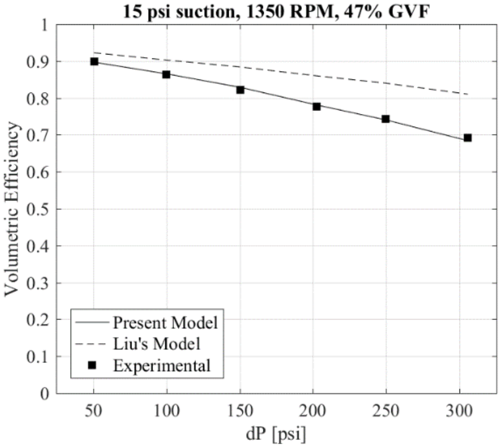
15 psi suction, 1350 RPM, 47% GVF

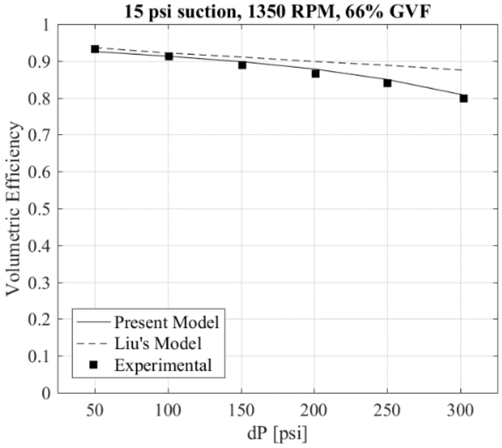
15 psi suction, 1350 RPM, 66% GVF

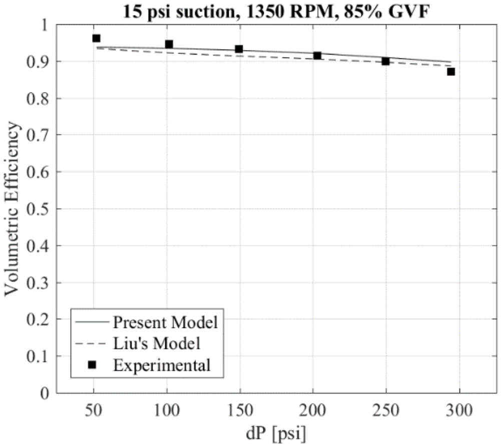
15 psi suction, 1350 RPM, 85% GVF

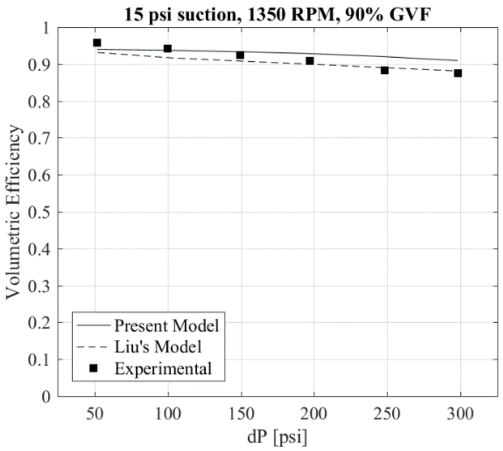
15 psi suction, 1350 RPM, 90% GVF
Volumetric Efficiency
0 0.1 0.2 0.3 0.4 0.5 0.6 0.7 0.8 0.9 1
50 100 150 200 250 300
dP [psi]
Present Model
Liu's Model
Experimental

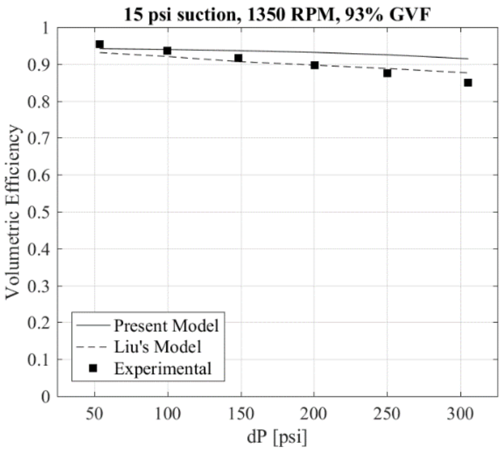
15 psi suction, 1350 RPM, 93% GVF
Volumetric Efficiency
0 0.1 0.2 0.3 0.4 0.5 0.6 0.7 0.8 0.9 1
50 100 150 200 250 300
dP [psi]
Present Model
Liu's Model
Experimental

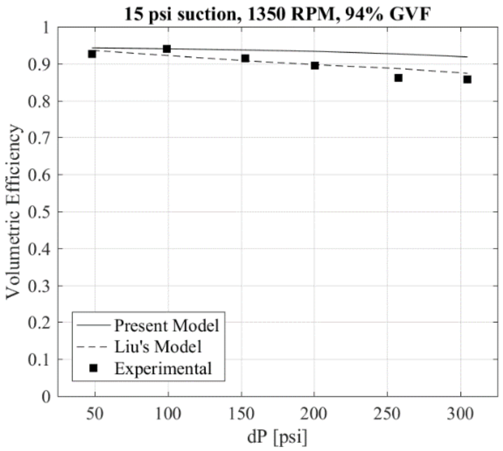
15 psi suction, 1350 RPM, 94% GVF
Volumetric Efficiency
0 0.1 0.2 0.3 0.4 0.5 0.6 0.7 0.8 0.9 1
50 100 150 200 250 300
dP [psi]
Present Model
Liu's Model
Experimental

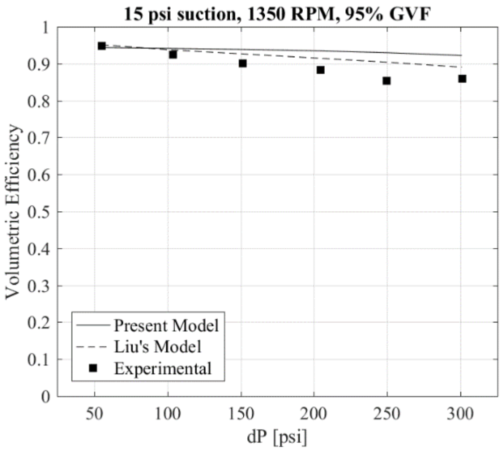
15 psi suction, 1350 RPM, 95% GVF
Volumetric Efficiency
0 0.1 0.2 0.3 0.4 0.5 0.6 0.7 0.8 0.9 1
50 100 150 200 250 300
dP [psi]
Present Model
Liu's Model
Experimental

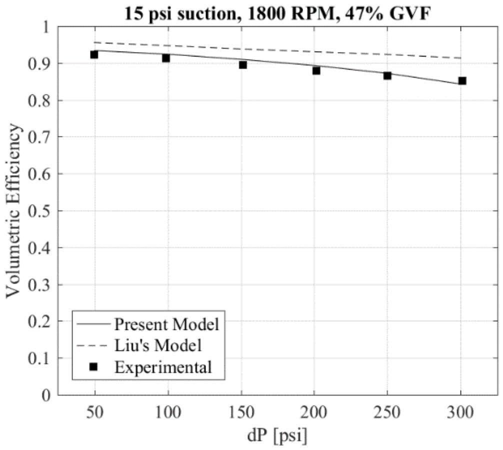
15 psi suction, 1800 RPM, 47% GVF
Volumetric Efficiency
0 0.1 0.2 0.3 0.4 0.5 0.6 0.7 0.8 0.9 1
50 100 150 200 250 300
dP [psi]
Present Model
Liu's Model
Experimental

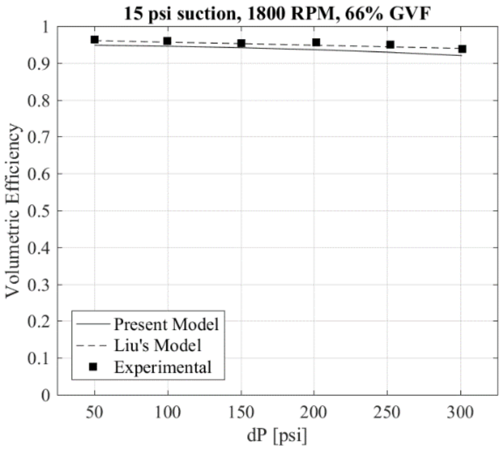
15 psi suction, 1800 RPM, 66% GVF
Volumetric Efficiency
0 0.1 0.2 0.3 0.4 0.5 0.6 0.7 0.8 0.9 1
50 100 150 200 250 300
dP [psi]
Present Model
Liu's Model
Experimental

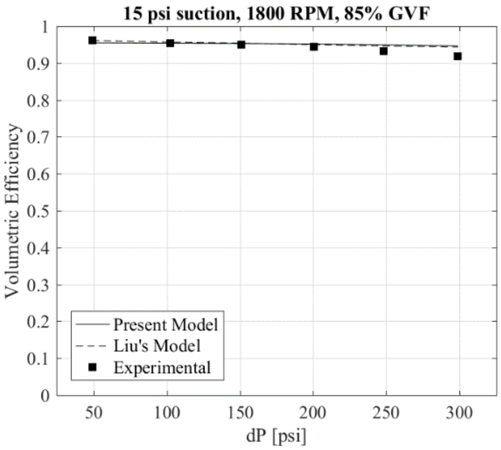
15 psi suction, 1800 RPM, 85% GVF

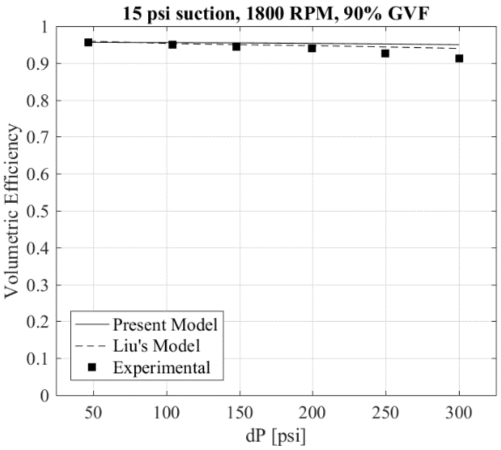
15 psi suction, 1800 RPM, 90% GVF

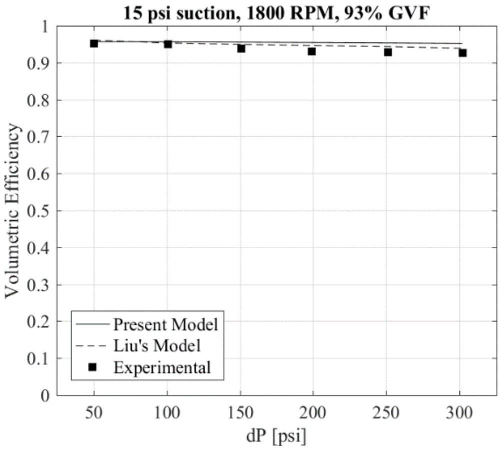
15 psi suction, 1800 RPM, 93% GVF

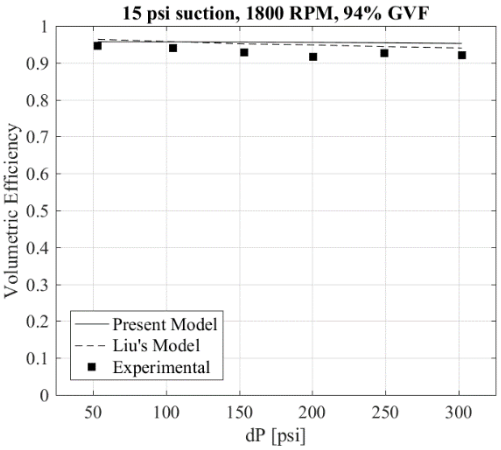
15 psi suction, 1800 RPM, 94% GVF

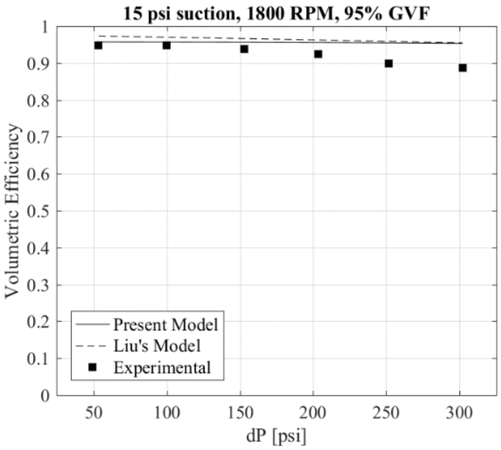
15 psi suction, 1800 RPM, 95% GVF

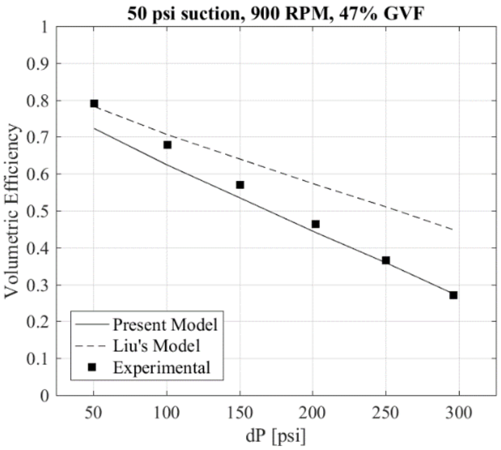
50 psi suction, 900 RPM, 47% GVF

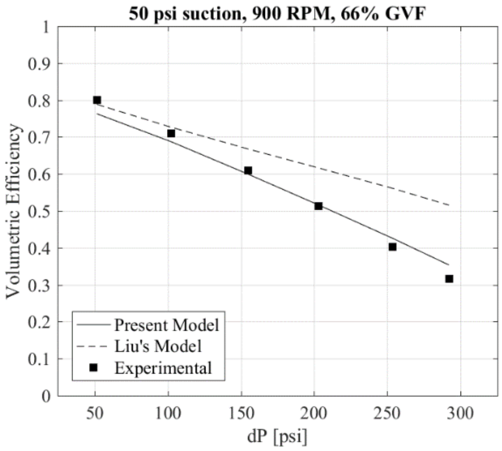
50 psi suction, 900 RPM, 66% GVF
Volumetric Efficiency
dP [psi]
0
0.1
0.2
0.3
0.4
0.5
0.6
0.7
0.8
0.9
1
50
100
150
200
250
300
Present Model
Liu's Model
Experimental

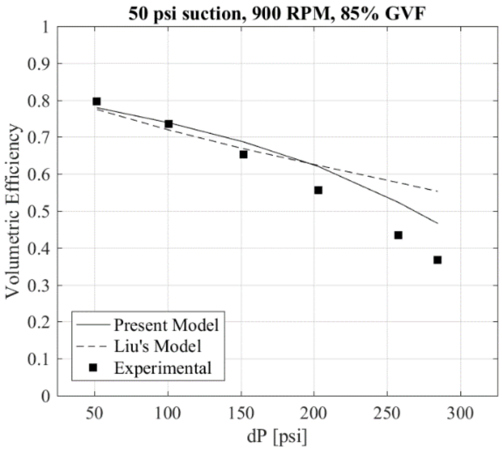
50 psi suction, 900 RPM, 85% GVF
Volumetric Efficiency
dP [psi]
0
0.1
0.2
0.3
0.4
0.5
0.6
0.7
0.8
0.9
1
50
100
150
200
250
300
Present Model
Liu's Model
Experimental

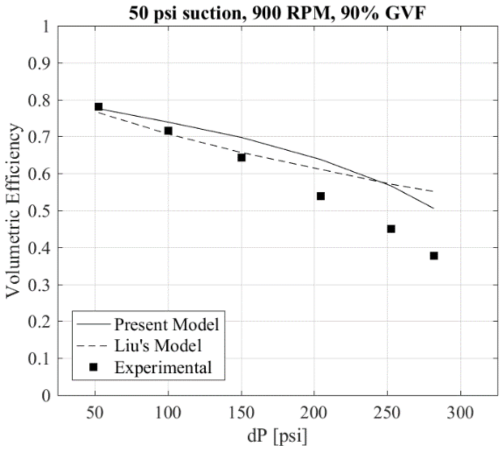
50 psi suction, 900 RPM, 90% GVF
Volumetric Efficiency
dP [psi]
0
0.1
0.2
0.3
0.4
0.5
0.6
0.7
0.8
0.9
1
50
100
150
200
250
300
Present Model
Liu's Model
Experimental

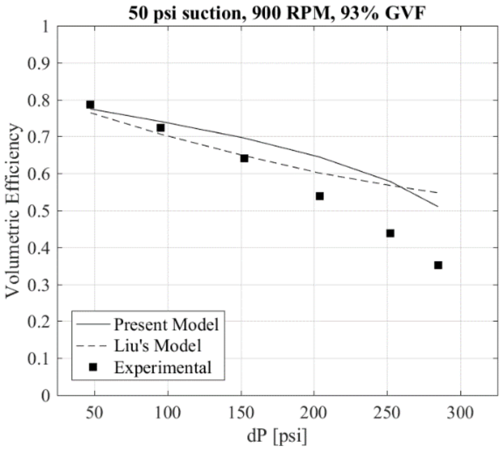
50 psi suction, 900 RPM, 93% GVF
Volumetric Efficiency
dP [psi]
0
0.1
0.2
0.3
0.4
0.5
0.6
0.7
0.8
0.9
1
50
100
150
200
250
300
Present Model
Liu's Model
Experimental

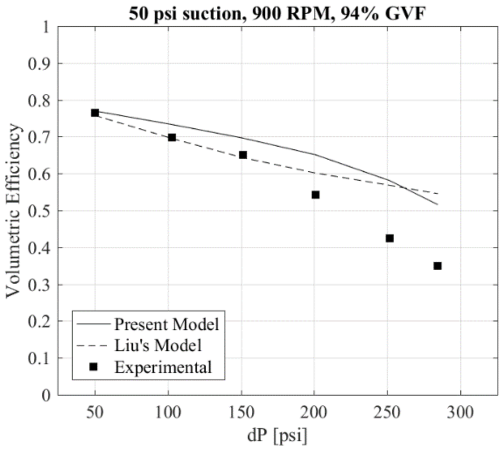
50 psi suction, 900 RPM, 94% GVF
Volumetric Efficiency
dP [psi]
0
0.1
0.2
0.3
0.4
0.5
0.6
0.7
0.8
0.9
1
50
100
150
200
250
300
Present Model
Liu's Model
Experimental

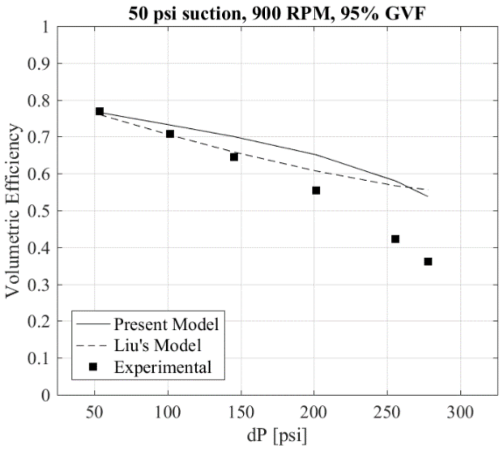
50 psi suction, 900 RPM, 95% GVF
Volumetric Efficiency
dP [psi]
0
0.1
0.2
0.3
0.4
0.5
0.6
0.7
0.8
0.9
1
50
100
150
200
250
300
Present Model
Liu's Model
Experimental

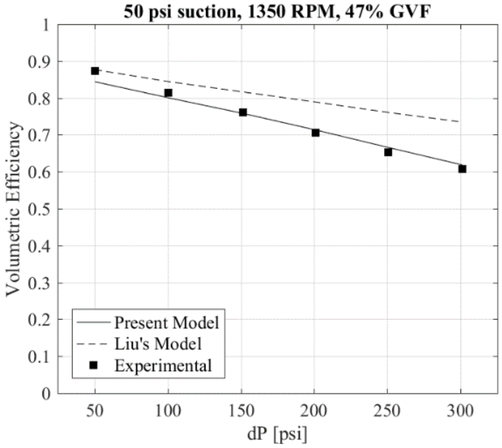
50 psi suction, 1350 RPM, 47% GVF

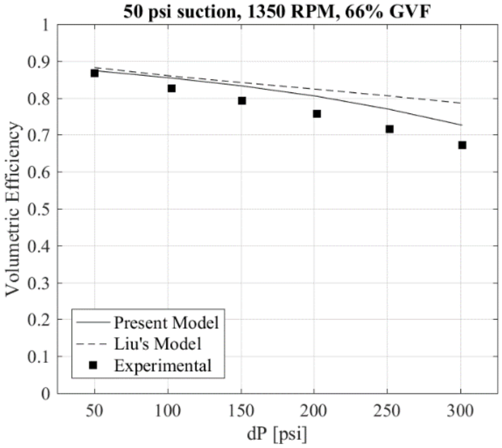
50 psi suction, 1350 RPM, 66% GVF

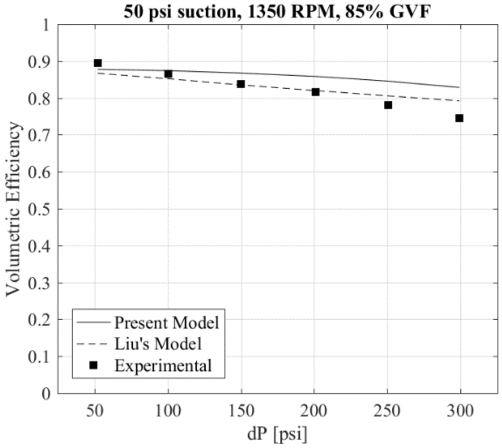
50 psi suction, 1350 RPM, 85% GVF

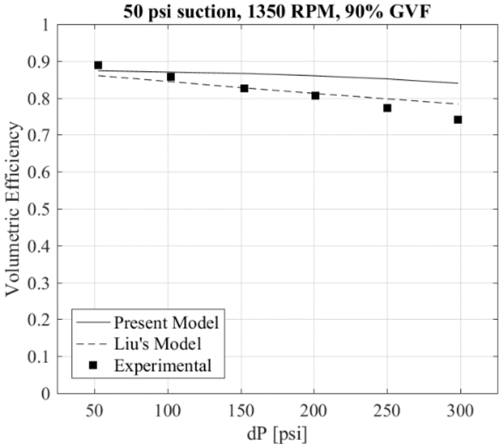
50 psi suction, 1350 RPM, 90% GVF

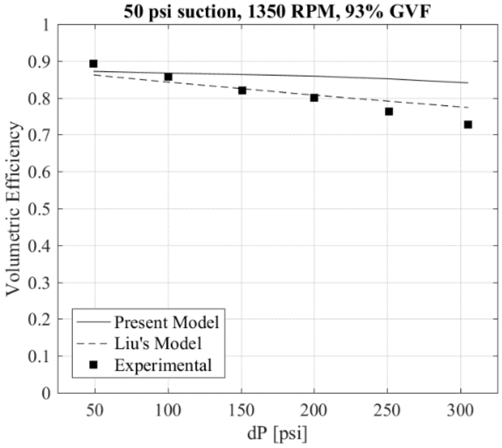
50 psi suction, 1350 RPM, 93% GVF

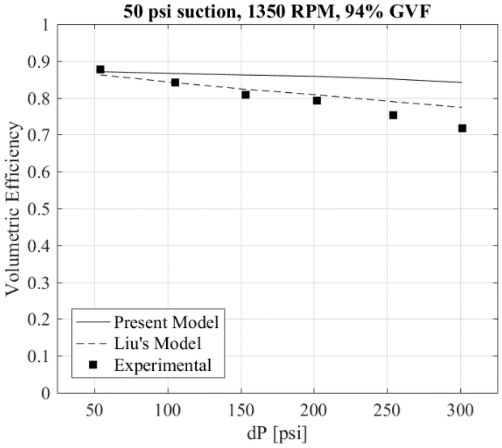
50 psi suction, 1350 RPM, 94% GVF

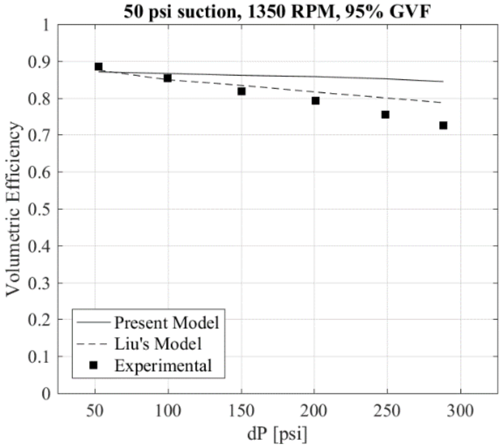
50 psi suction, 1350 RPM, 95% GVF

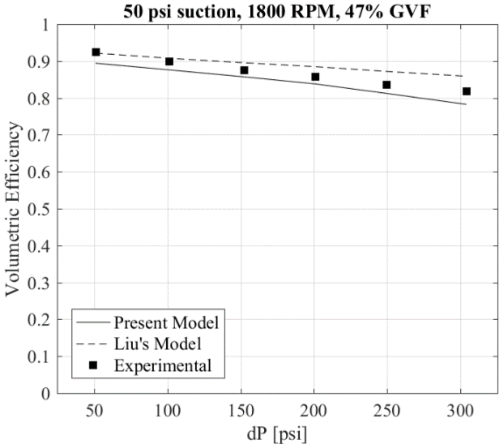
50 psi suction, 1800 RPM, 47% GVF

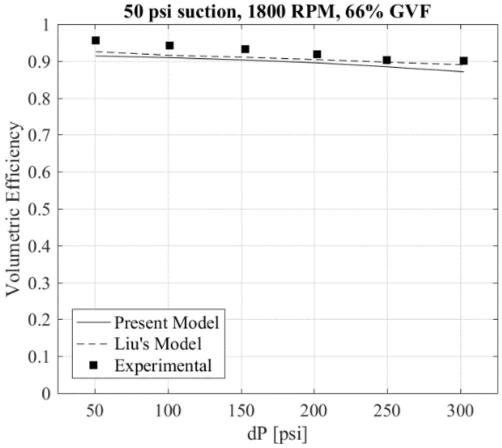
50 psi suction, 1800 RPM, 66% GVF

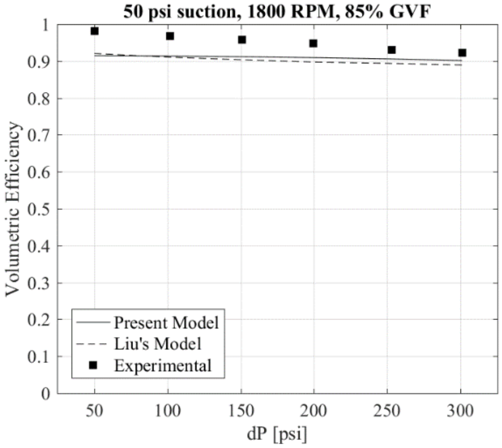
50 psi suction, 1800 RPM, 85% GVF

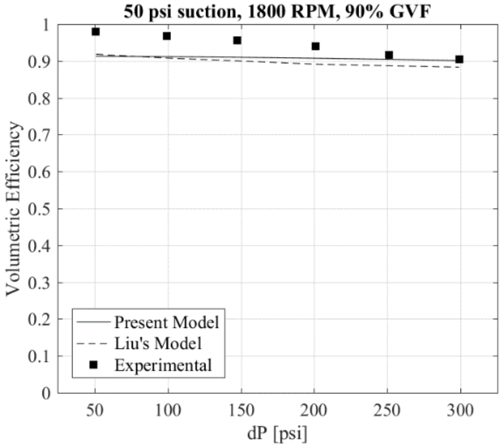
50 psi suction, 1800 RPM, 90% GVF

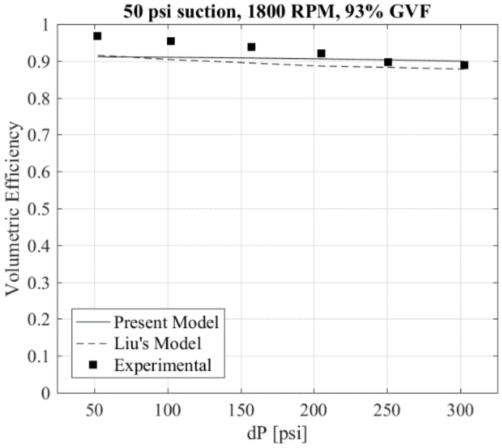
50 psi suction, 1800 RPM, 93% GVF

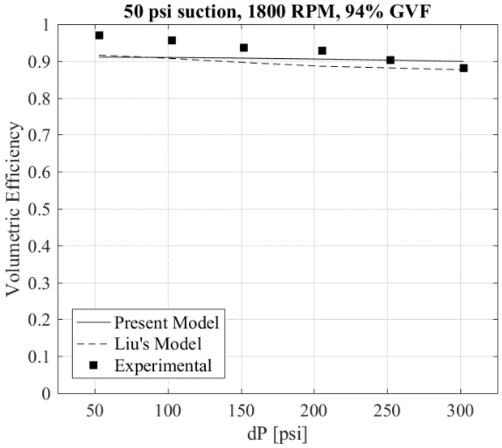
50 psi suction, 1800 RPM, 94% GVF

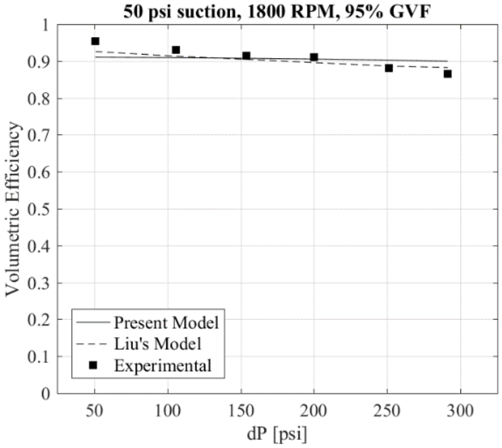
50 psi suction, 1800 RPM, 95% GVF

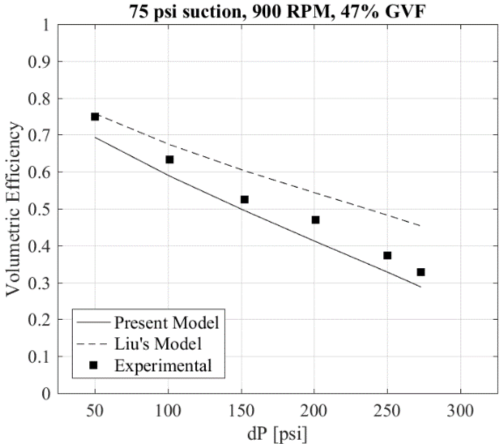
75 psi suction, 900 RPM, 47% GVF

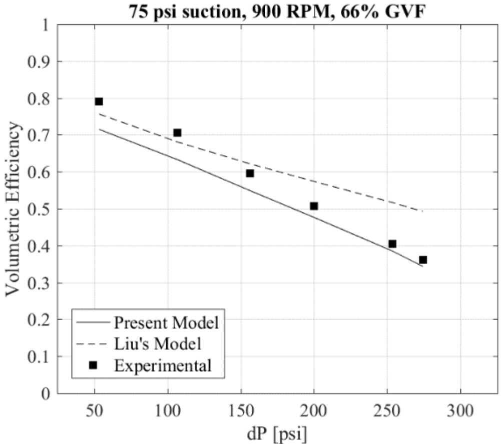
75 psi suction, 900 RPM, 66% GVF

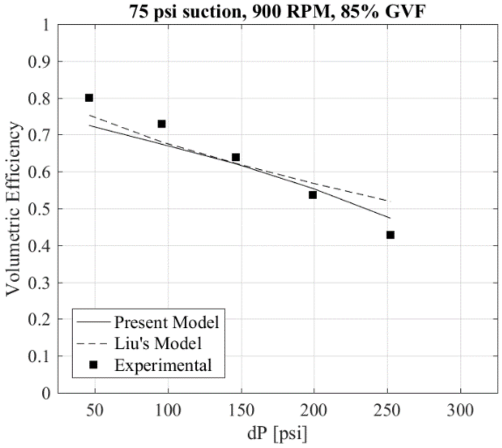
75 psi suction, 900 RPM, 85% GVF

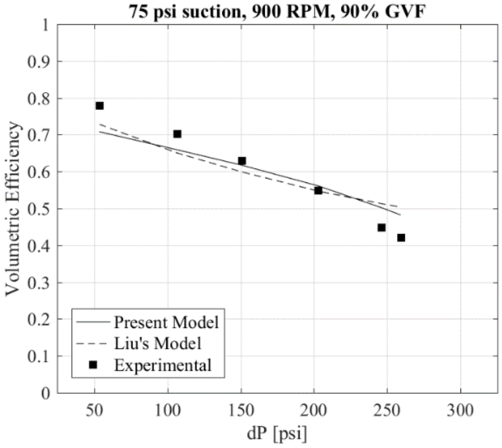
75 psi suction, 900 RPM, 90% GVF

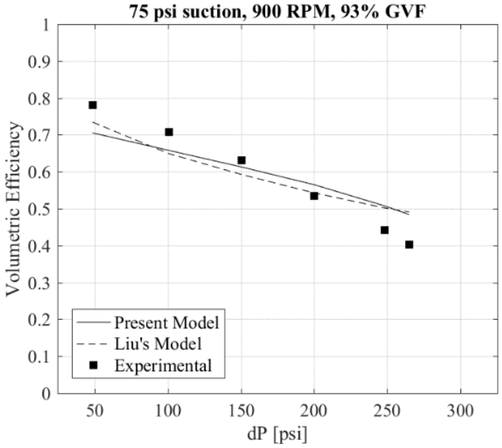
75 psi suction, 900 RPM, 93% GVF

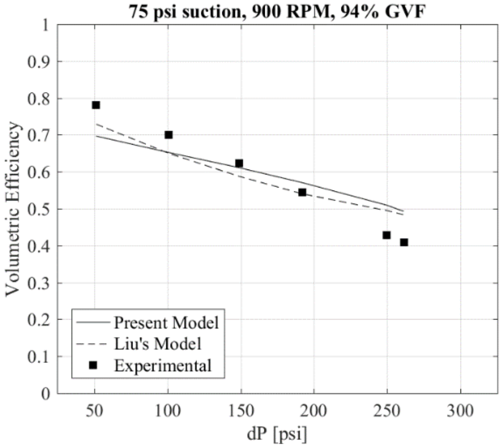
75 psi suction, 900 RPM, 94% GVF

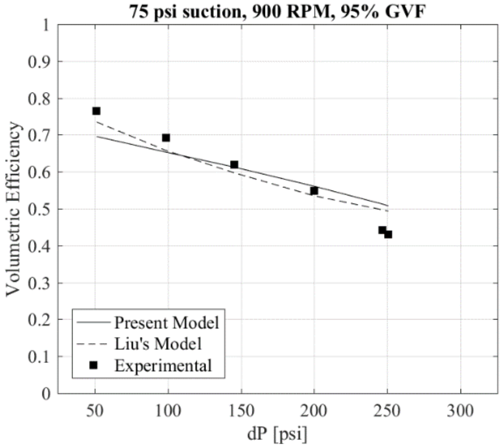
75 psi suction, 900 RPM, 95% GVF

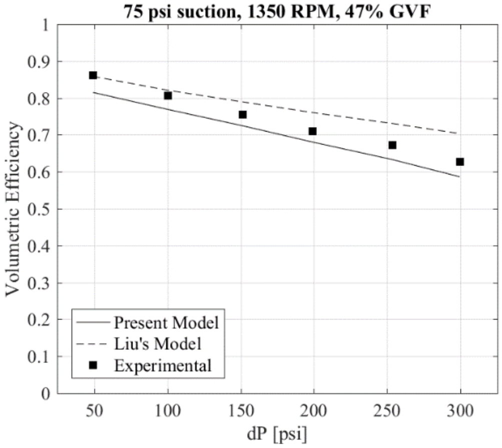
75 psi suction, 1350 RPM, 47% GVF

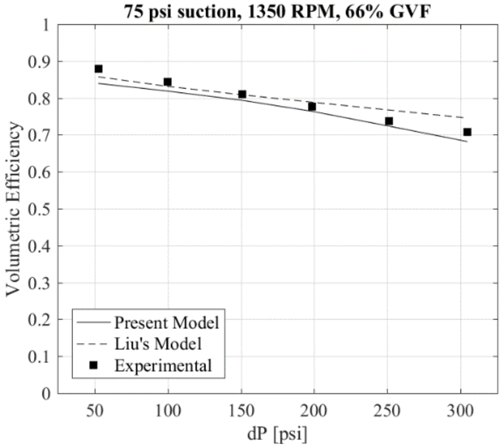
75 psi suction, 1350 RPM, 66% GVF

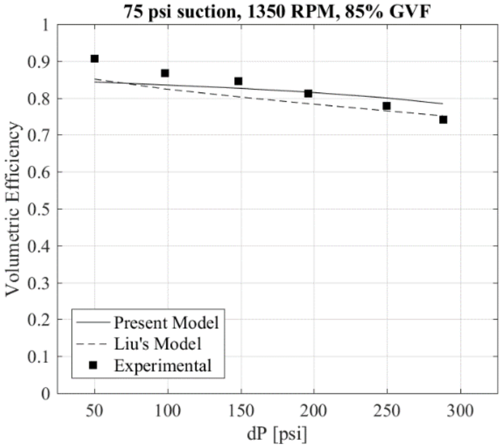
75 psi suction, 1350 RPM, 85% GVF

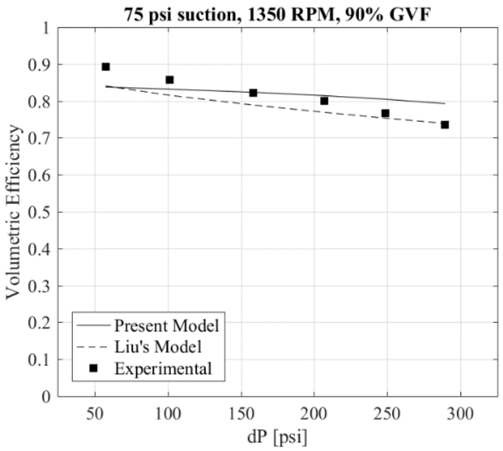
75 psi suction, 1350 RPM, 90% GVF
Volumetric Efficiency
0
0.1
0.2
0.3
0.4
0.5
0.6
0.7
0.8
0.9
1
50
100
150
200
250
300
dP [psi]
Present Model
Liu's Model
Experimental

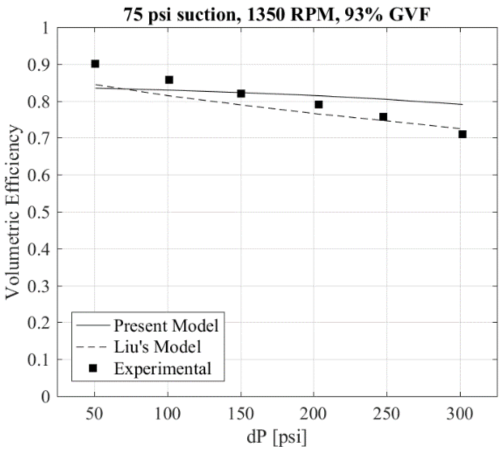
75 psi suction, 1350 RPM, 93% GVF
Volumetric Efficiency
0
0.1
0.2
0.3
0.4
0.5
0.6
0.7
0.8
0.9
1
50
100
150
200
250
300
dP [psi]
Present Model
Liu's Model
Experimental

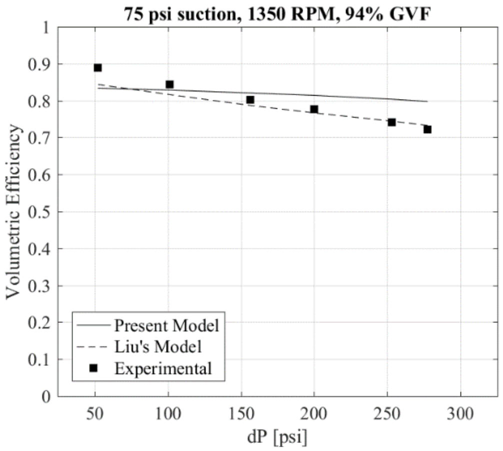
75 psi suction, 1350 RPM, 94% GVF
Volumetric Efficiency
0
0.1
0.2
0.3
0.4
0.5
0.6
0.7
0.8
0.9
1
50
100
150
200
250
300
dP [psi]
Present Model
Liu's Model
Experimental

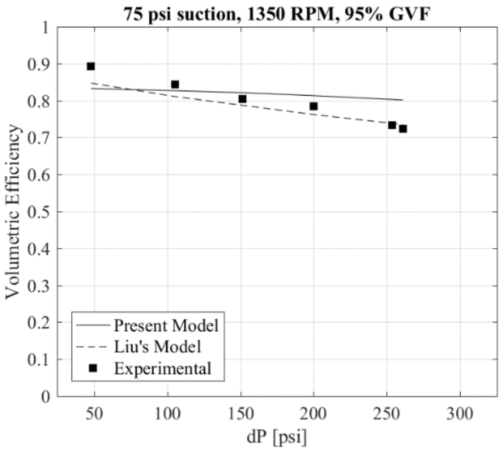
75 psi suction, 1350 RPM, 95% GVF
Volumetric Efficiency
0
0.1
0.2
0.3
0.4
0.5
0.6
0.7
0.8
0.9
1
50
100
150
200
250
300
dP [psi]
Present Model
Liu's Model
Experimental

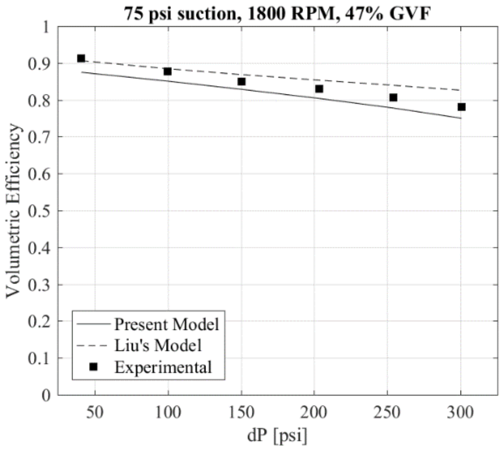
75 psi suction, 1800 RPM, 47% GVF
Volumetric Efficiency
0
0.1
0.2
0.3
0.4
0.5
0.6
0.7
0.8
0.9
1
50
100
150
200
250
300
dP [psi]
Present Model
Liu's Model
Experimental

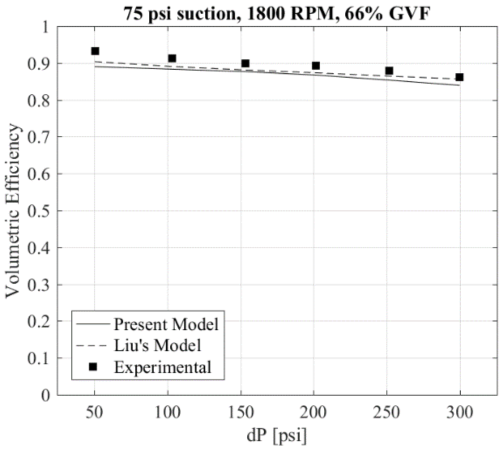
75 psi suction, 1800 RPM, 66% GVF
Volumetric Efficiency
0
0.1
0.2
0.3
0.4
0.5
0.6
0.7
0.8
0.9
1
50
100
150
200
250
300
dP [psi]
Present Model
Liu's Model
Experimental

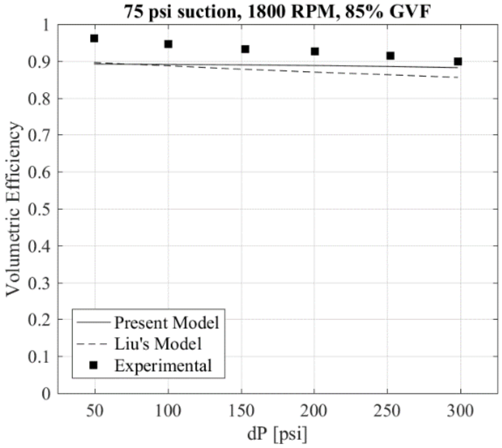
75 psi suction, 1800 RPM, 85% GVF

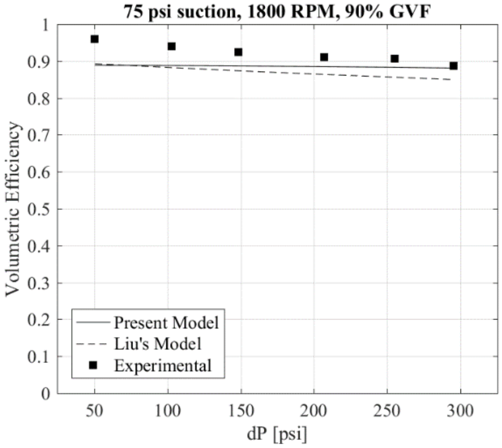
75 psi suction, 1800 RPM, 90% GVF

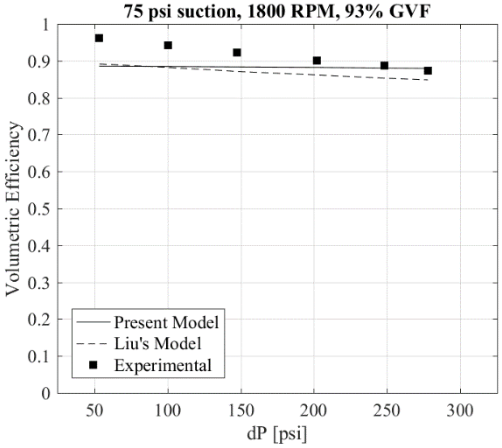
75 psi suction, 1800 RPM, 93% GVF

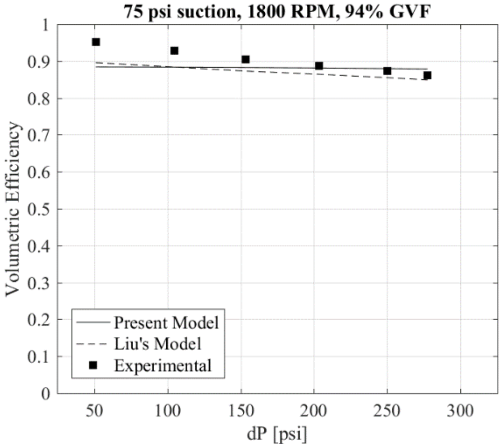
75 psi suction, 1800 RPM, 94% GVF

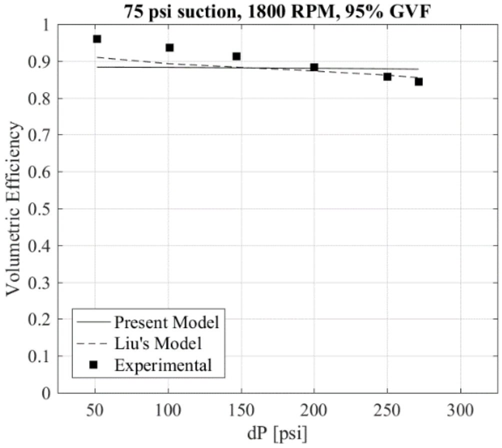
75 psi suction, 1800 RPM, 95% GVF

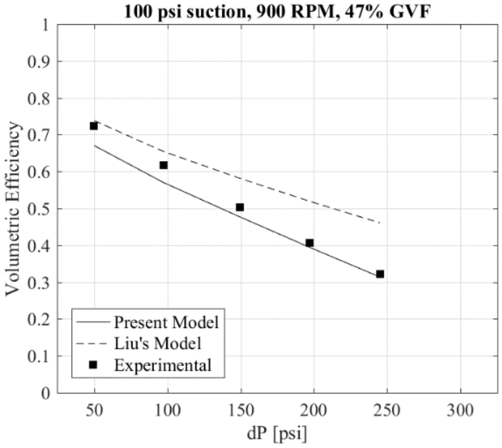
100 psi suction, 900 RPM, 47% GVF

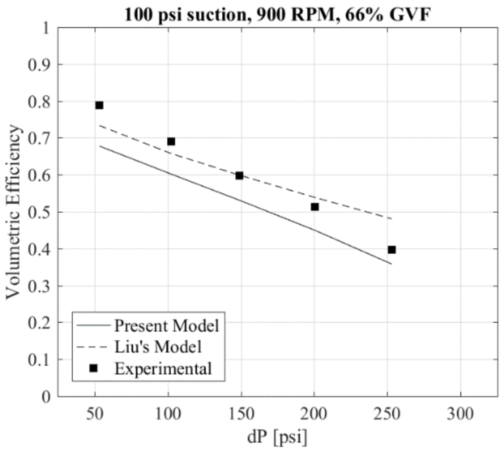
100 psi suction, 900 RPM, 66% GVF
Volumetric Efficiency
dP [psi]
0
0.1
0.2
0.3
0.4
0.5
0.6
0.7
0.8
0.9
1
50
100
150
200
250
300
Present Model
Liu's Model
Experimental

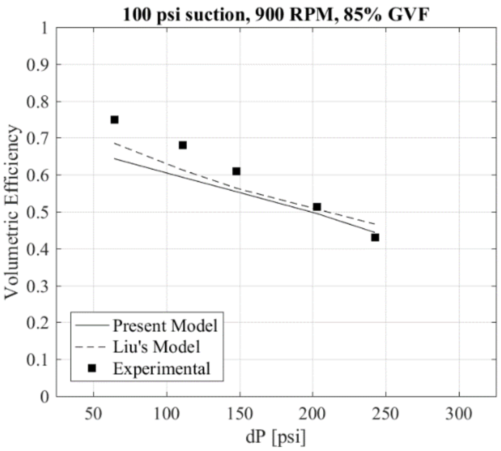
100 psi suction, 900 RPM, 85% GVF
Volumetric Efficiency
dP [psi]
0
0.1
0.2
0.3
0.4
0.5
0.6
0.7
0.8
0.9
1
50
100
150
200
250
300
Present Model
Liu's Model
Experimental

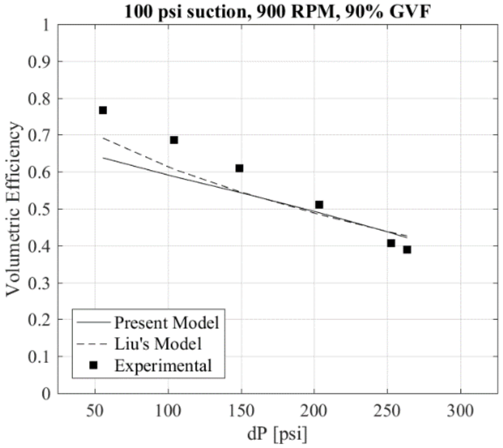
100 psi suction, 900 RPM, 90% GVF
Volumetric Efficiency
dP [psi]
0
0.1
0.2
0.3
0.4
0.5
0.6
0.7
0.8
0.9
1
50
100
150
200
250
300
Present Model
Liu's Model
Experimental

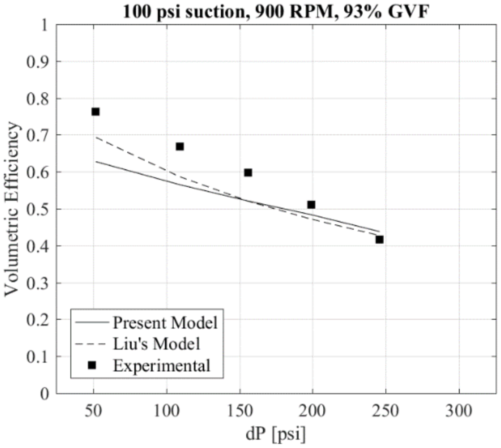
100 psi suction, 900 RPM, 93% GVF
Volumetric Efficiency
dP [psi]
0
0.1
0.2
0.3
0.4
0.5
0.6
0.7
0.8
0.9
1
50
100
150
200
250
300
Present Model
Liu's Model
Experimental

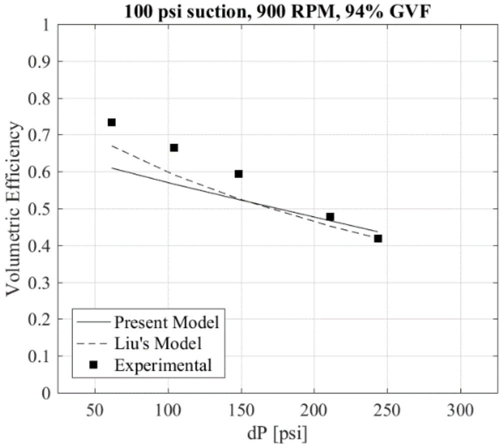
100 psi suction, 900 RPM, 94% GVF
Volumetric Efficiency
dP [psi]
0
0.1
0.2
0.3
0.4
0.5
0.6
0.7
0.8
0.9
1
50
100
150
200
250
300
Present Model
Liu's Model
Experimental

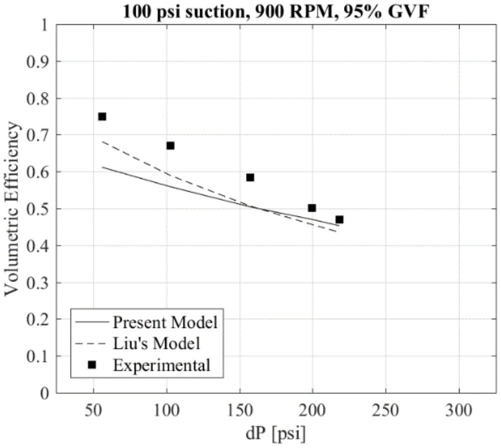
100 psi suction, 900 RPM, 95% GVF
Volumetric Efficiency
dP [psi]
0
0.1
0.2
0.3
0.4
0.5
0.6
0.7
0.8
0.9
1
50
100
150
200
250
300
Present Model
Liu's Model
Experimental

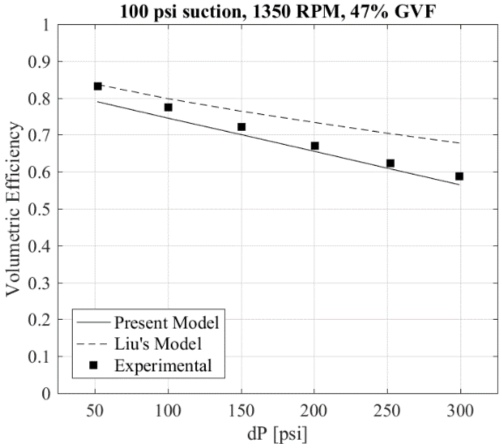
100 psi suction, 1350 RPM, 47% GVF

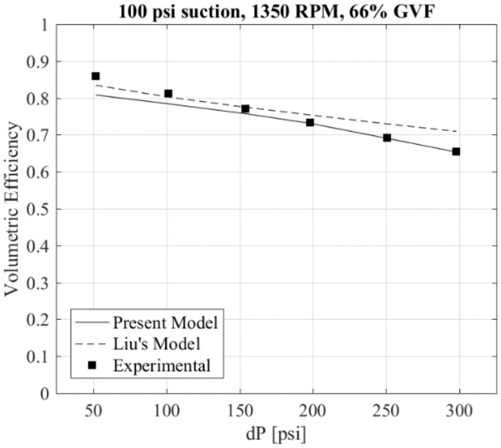
100 psi suction, 1350 RPM, 66% GVF

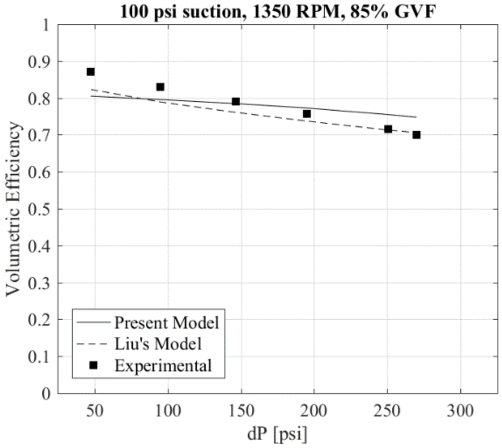
100 psi suction, 1350 RPM, 85% GVF

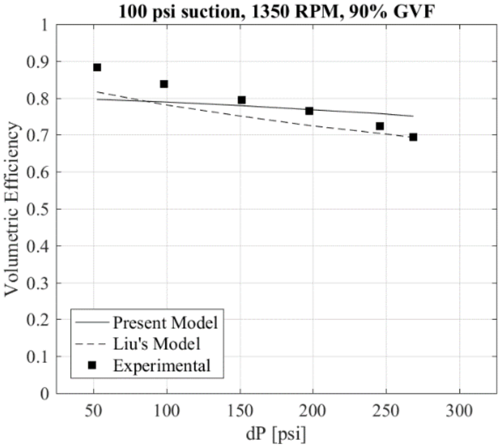
100 psi suction, 1350 RPM, 90% GVF

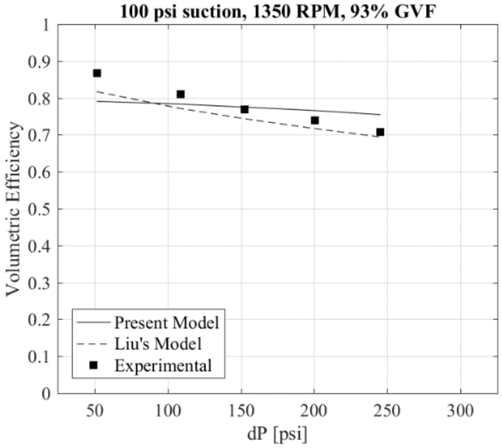
100 psi suction, 1350 RPM, 93% GVF

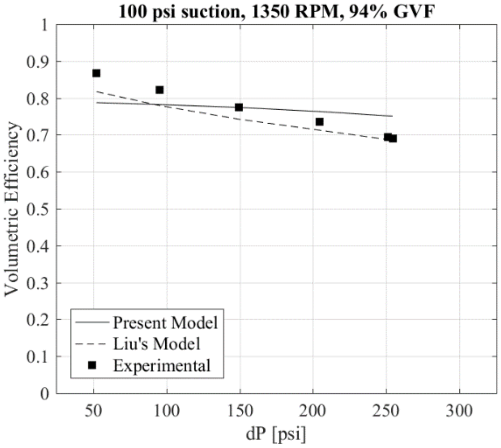
100 psi suction, 1350 RPM, 94% GVF

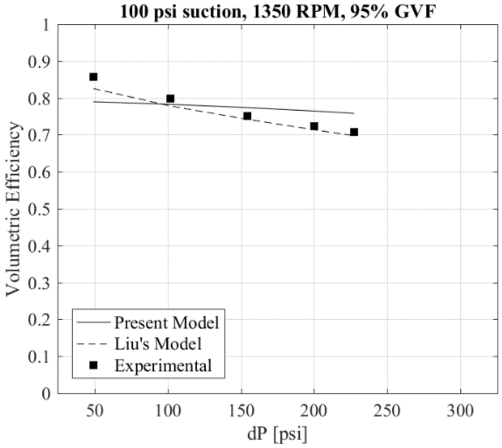
100 psi suction, 1350 RPM, 95% GVF

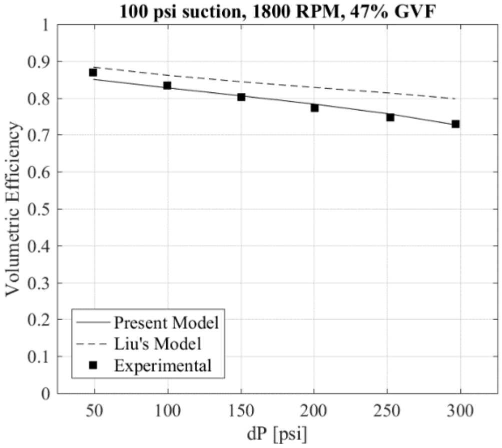
100 psi suction, 1800 RPM, 47% GVF

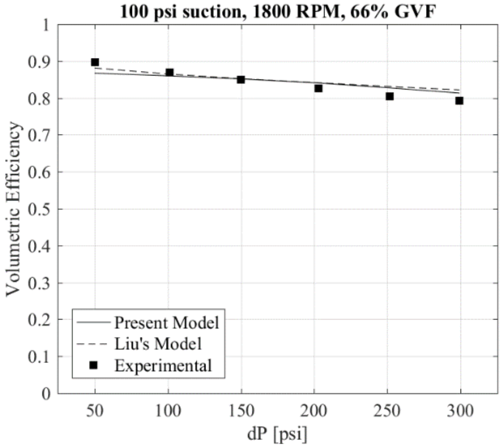
100 psi suction, 1800 RPM, 66% GVF

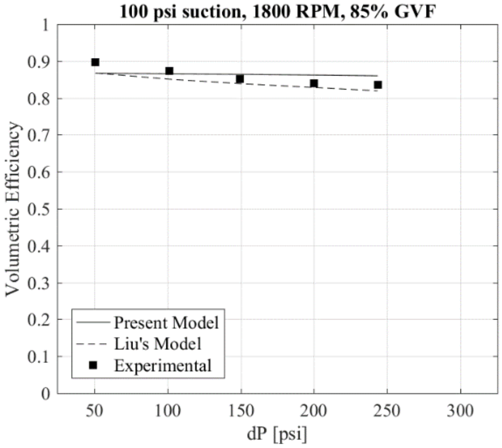
100 psi suction, 1800 RPM, 85% GVF

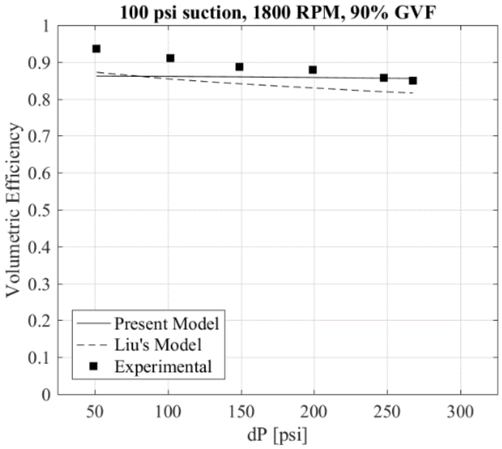

100 psi suction, 1800 RPM, 90% GVF

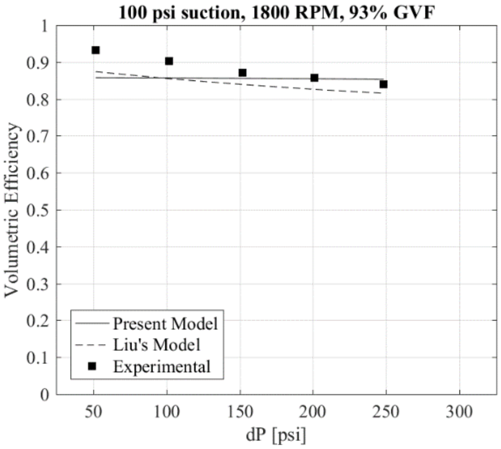

100 psi suction, 1800 RPM, 93% GVF

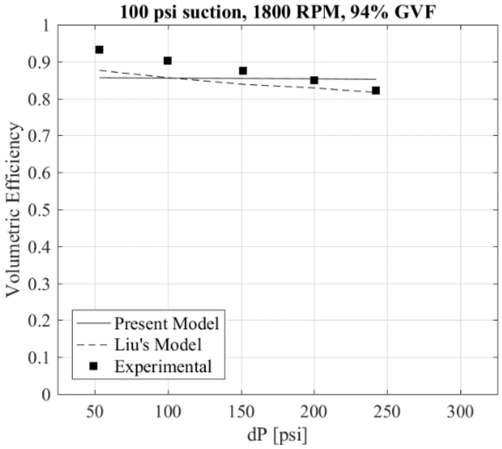

100 psi suction, 1800 RPM, 94% GVF

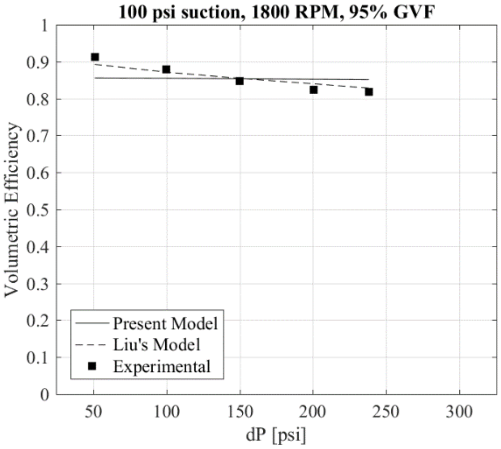

100 psi suction, 1800 RPM, 95% GVF

## A.2. Mach Number Graphs

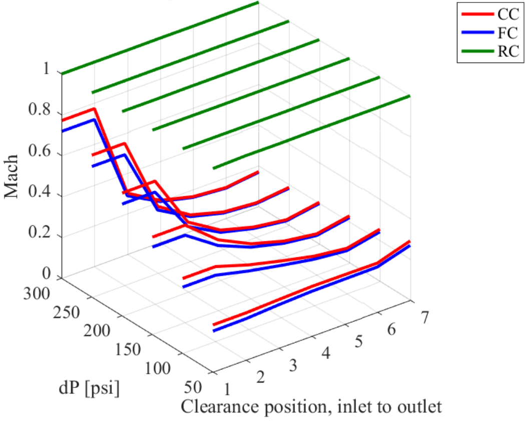
Mach in RC, 15 psi suction, 900 RPM, 47% GVF

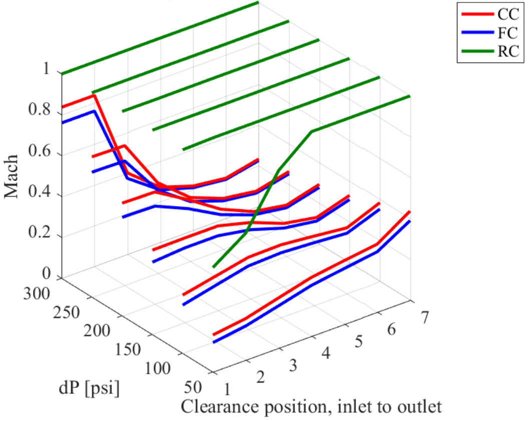
Mach in RC, 15 psi suction, 900 RPM, 66% GVF

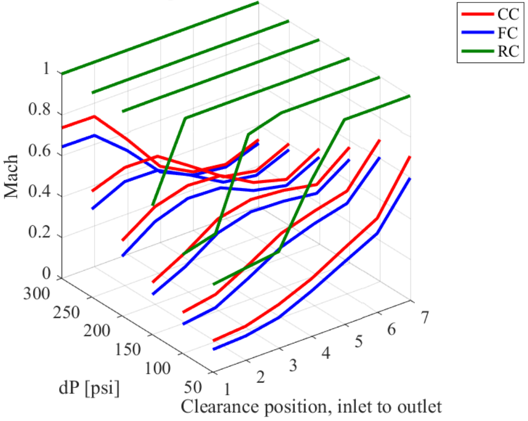
Mach in RC, 15 psi suction, 900 RPM, 85% GVF

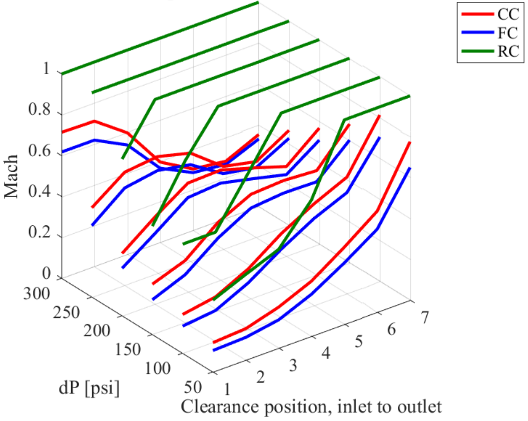
Mach in RC, 15 psi suction, 900 RPM, 90% GVF

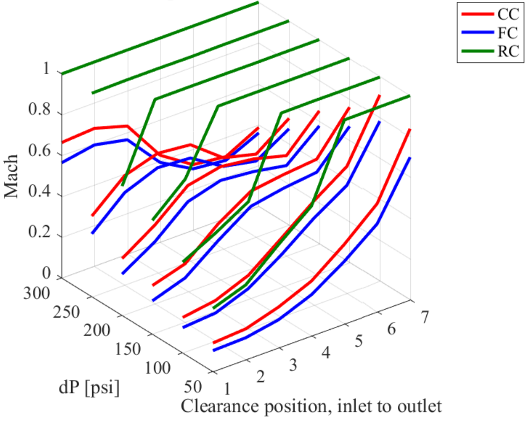
Mach in RC, 15 psi suction, 900 RPM, 93% GVF

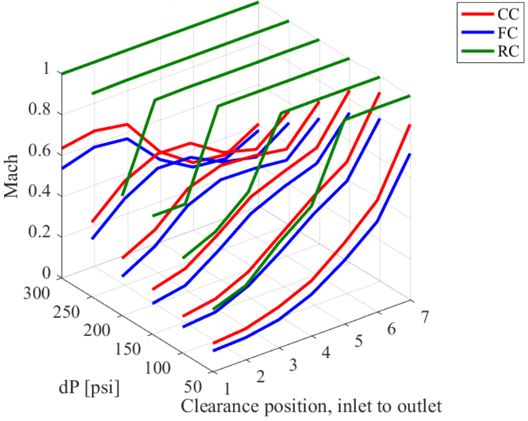
Mach in RC, 15 psi suction, 900 RPM, 94% GVF

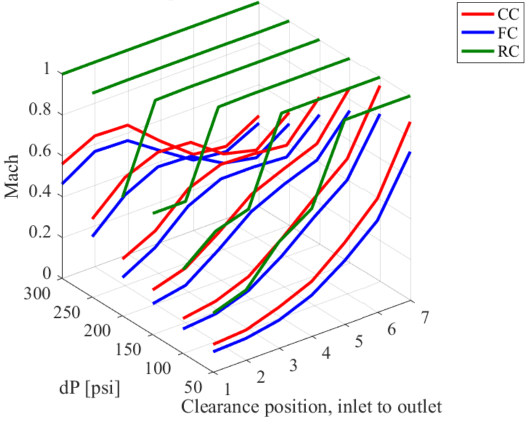
Mach in RC, 15 psi suction, 900 RPM, 95% GVF

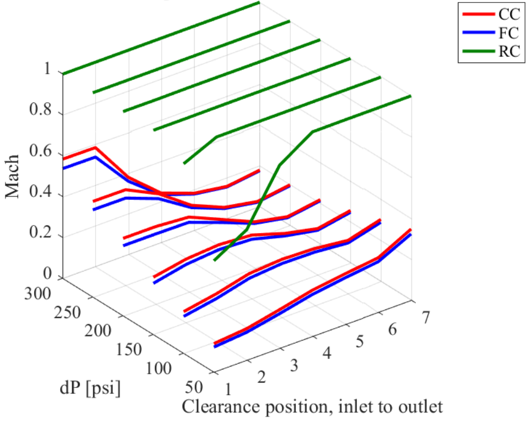
Mach in RC, 15 psi suction, 1350 RPM, 47% GVF

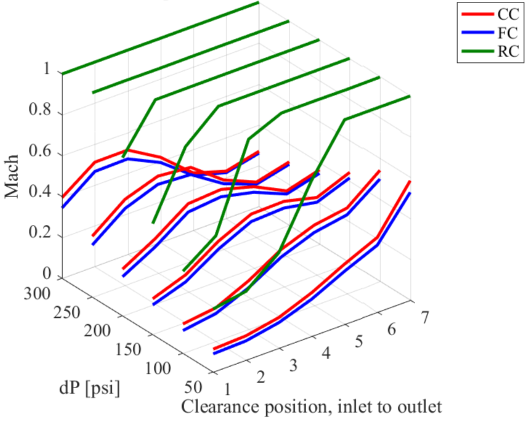
Mach in RC, 15 psi suction, 1350 RPM, 66% GVF

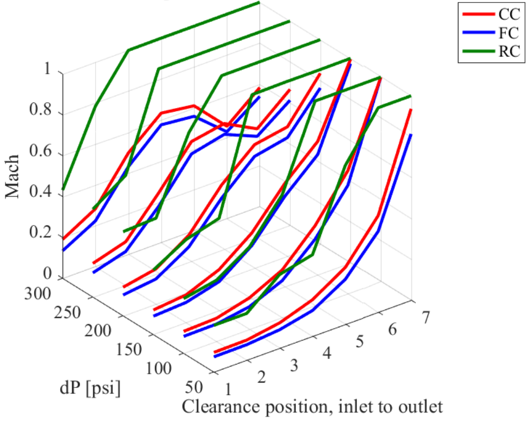
Mach in RC, 15 psi suction, 1350 RPM, 85% GVF

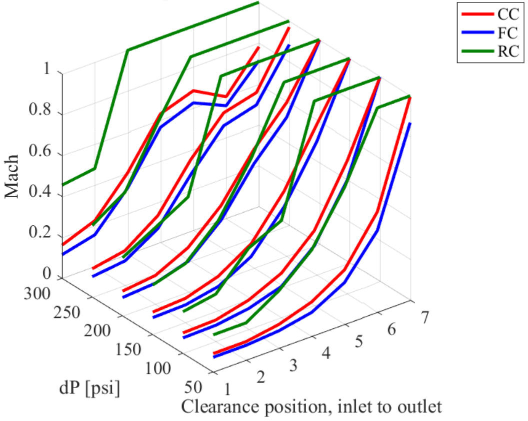
Mach in RC, 15 psi suction, 1350 RPM, 90% GVF

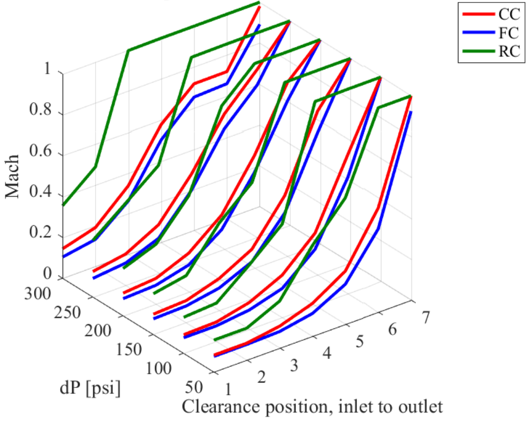
Mach in RC, 15 psi suction, 1350 RPM, 93% GVF

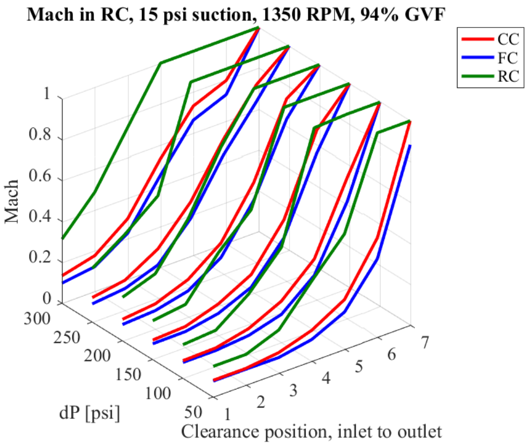
Mach in RC, 15 psi suction, 1350 RPM, 94% GVF

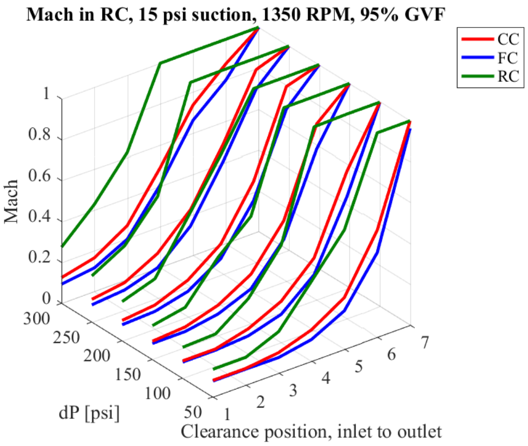
Mach in RC, 15 psi suction, 1350 RPM, 95% GVF

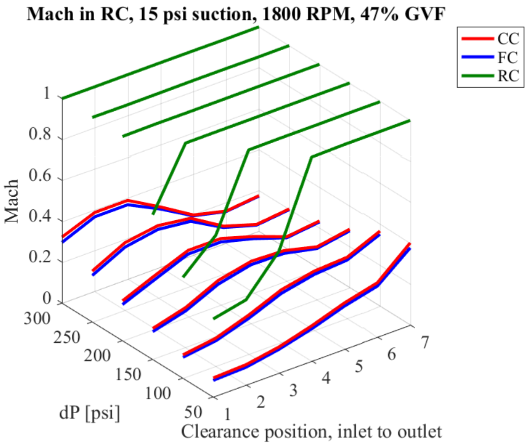
Mach in RC, 15 psi suction, 1800 RPM, 47% GVF

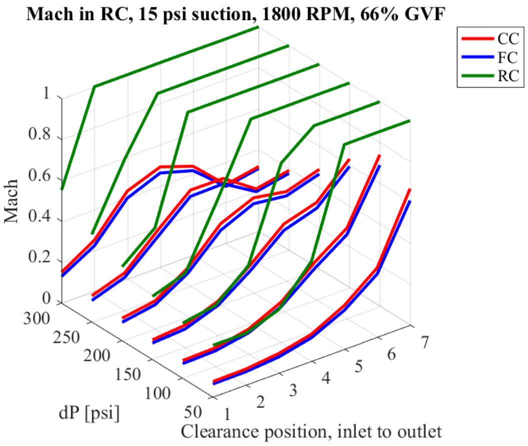
Mach in RC, 15 psi suction, 1800 RPM, 66% GVF

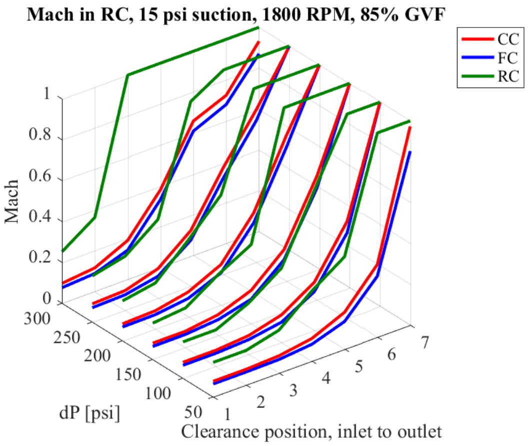
Mach in RC, 15 psi suction, 1800 RPM, 85% GVF

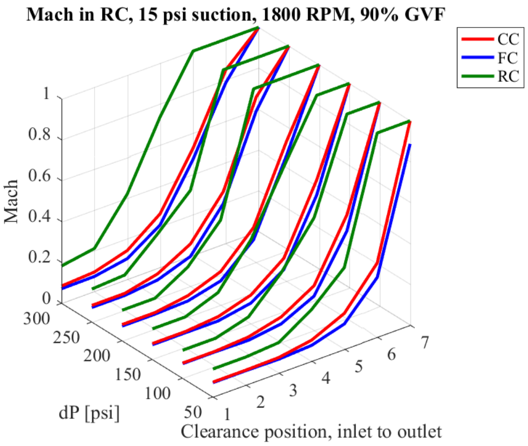
Mach in RC, 15 psi suction, 1800 RPM, 90% GVF

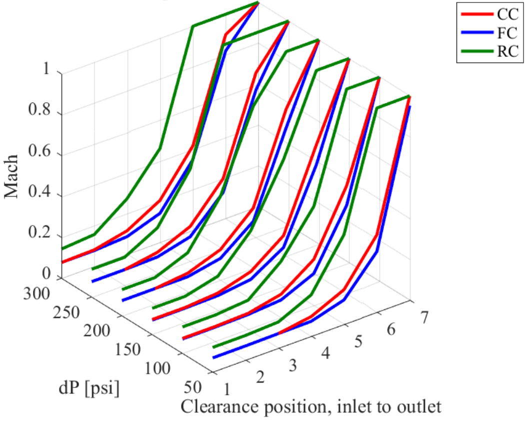

Mach in RC, 15 psi suction, 1800 RPM, 93% GVF

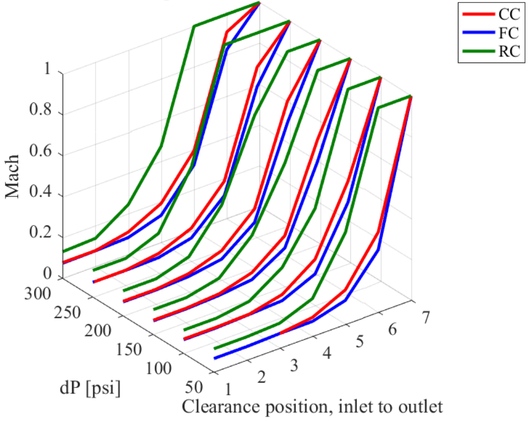

Mach in RC, 15 psi suction, 1800 RPM, 94% GVF

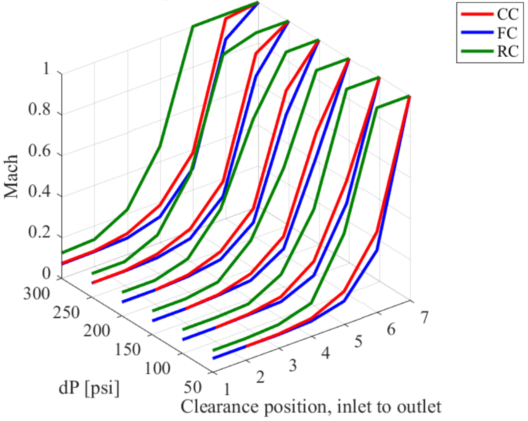

Mach in RC, 15 psi suction, 1800 RPM, 95% GVF

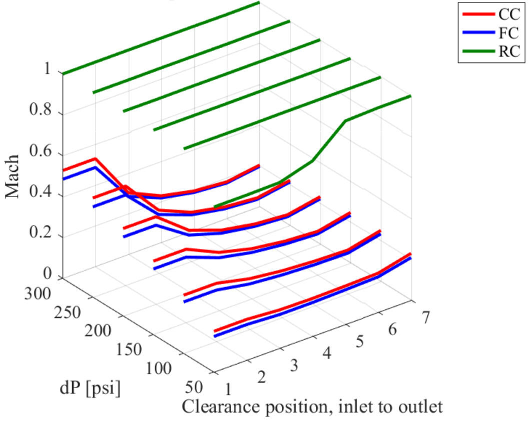

Mach in RC, 50 psi suction, 900 RPM, 47% GVF

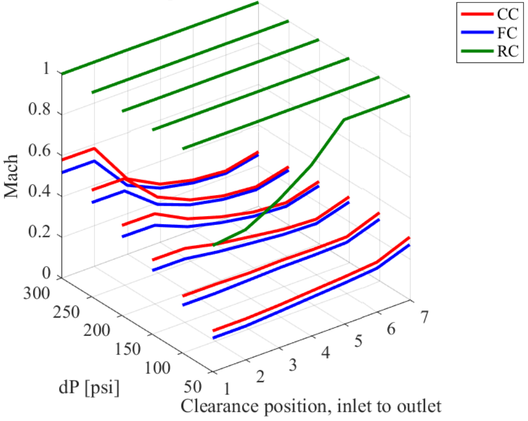

Mach in RC, 50 psi suction, 900 RPM, 66% GVF

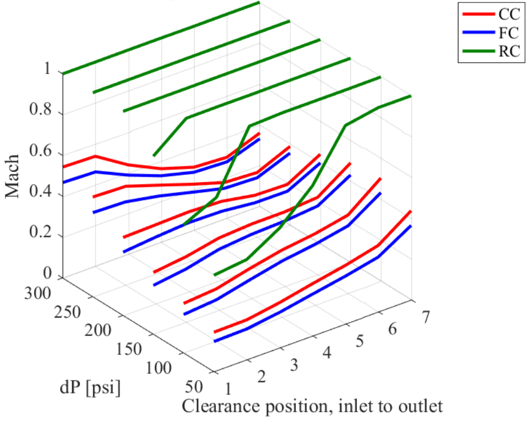

Mach in RC, 50 psi suction, 900 RPM, 85% GVF

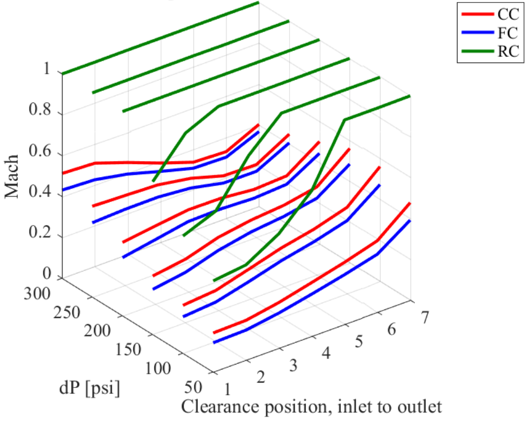
Mach in RC, 50 psi suction, 900 RPM, 90% GVF

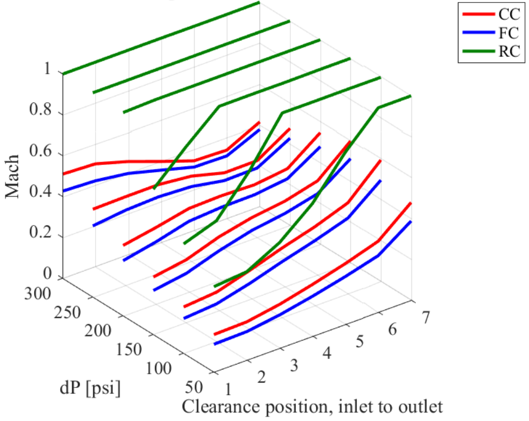
Mach in RC, 50 psi suction, 900 RPM, 93% GVF

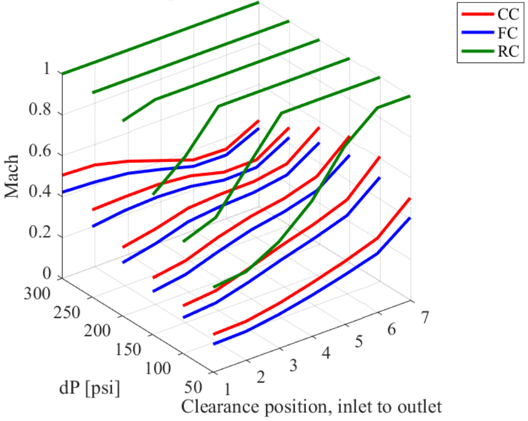
Mach in RC, 50 psi suction, 900 RPM, 94% GVF

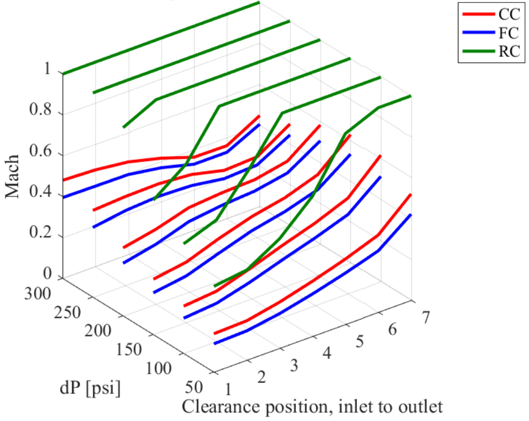
Mach in RC, 50 psi suction, 900 RPM, 95% GVF

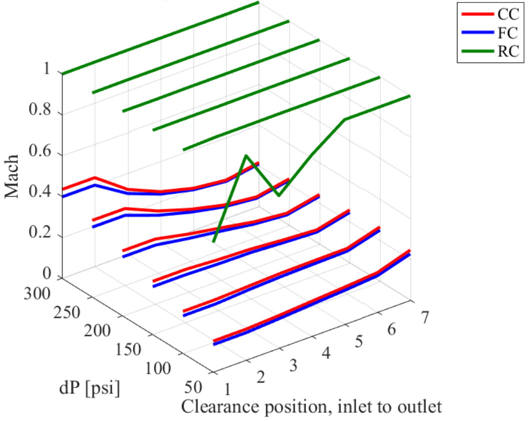
Mach in RC, 50 psi suction, 1350 RPM, 47% GVF

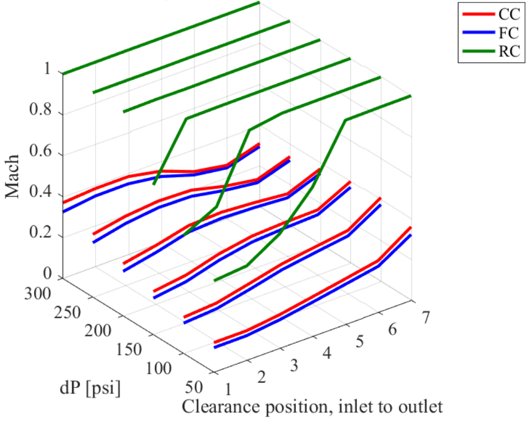
Mach in RC, 50 psi suction, 1350 RPM, 66% GVF

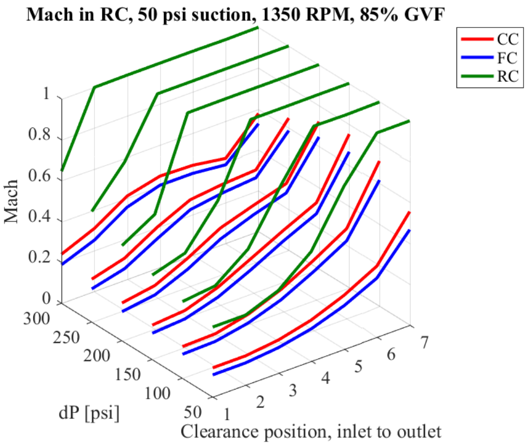
Mach in RC, 50 psi suction, 1350 RPM, 85% GVF

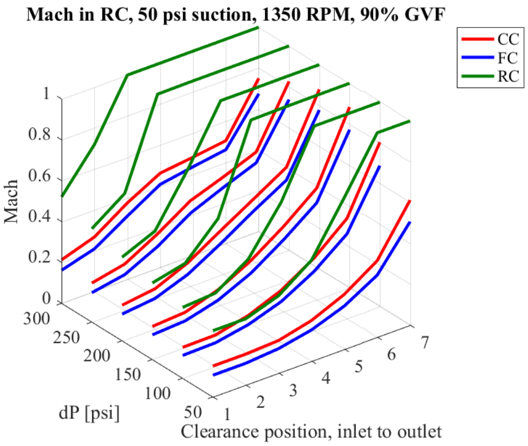
Mach in RC, 50 psi suction, 1350 RPM, 90% GVF

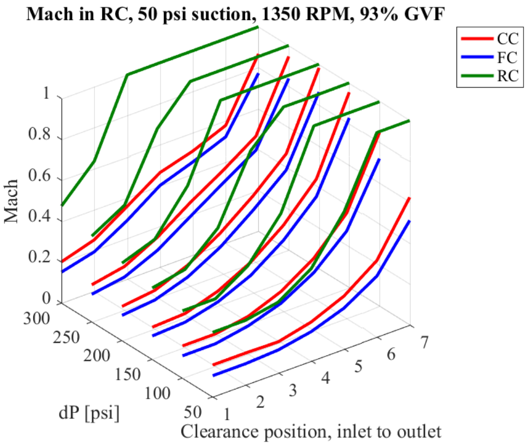
Mach in RC, 50 psi suction, 1350 RPM, 93% GVF

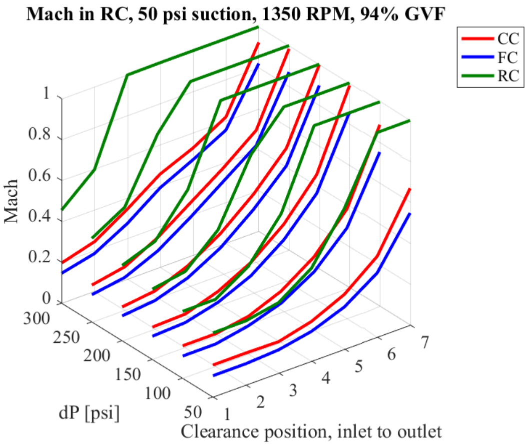
Mach in RC, 50 psi suction, 1350 RPM, 94% GVF

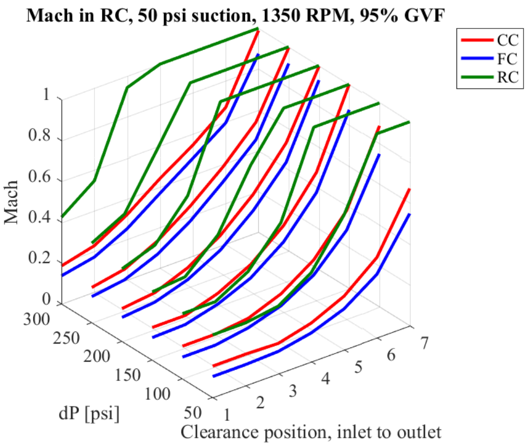
Mach in RC, 50 psi suction, 1350 RPM, 95% GVF

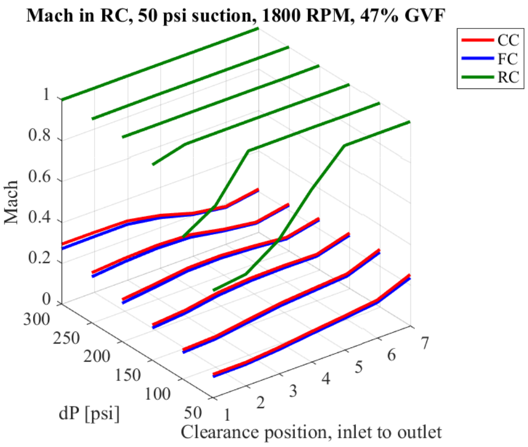
Mach in RC, 50 psi suction, 1800 RPM, 47% GVF

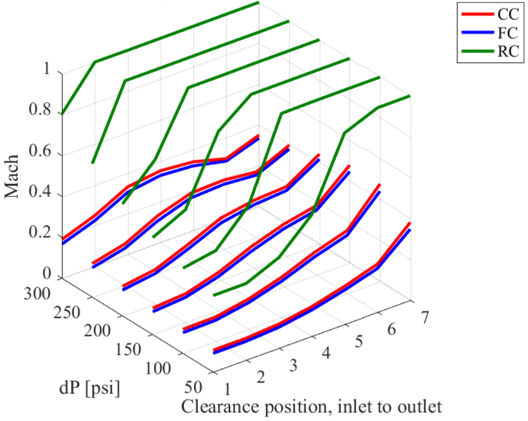

Mach in RC, 50 psi suction, 1800 RPM, 66% GVF

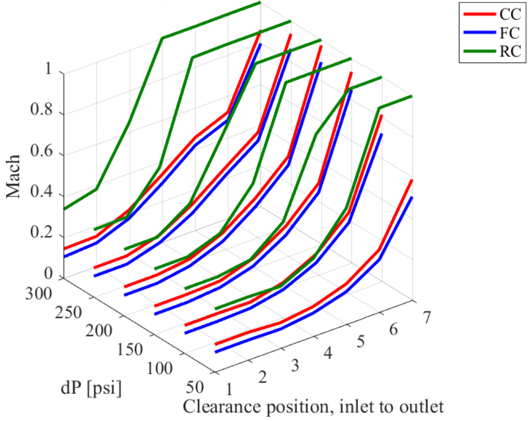

Mach in RC, 50 psi suction, 1800 RPM, 85% GVF

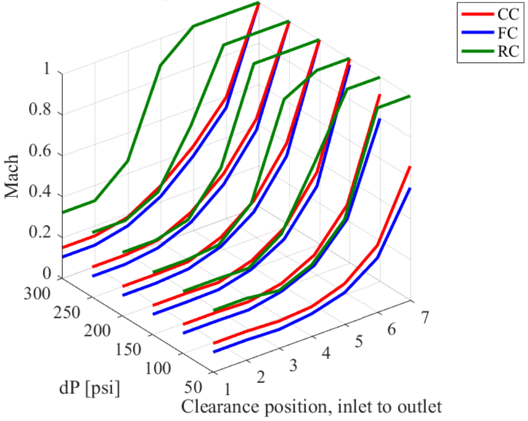

Mach in RC, 50 psi suction, 1800 RPM, 90% GVF

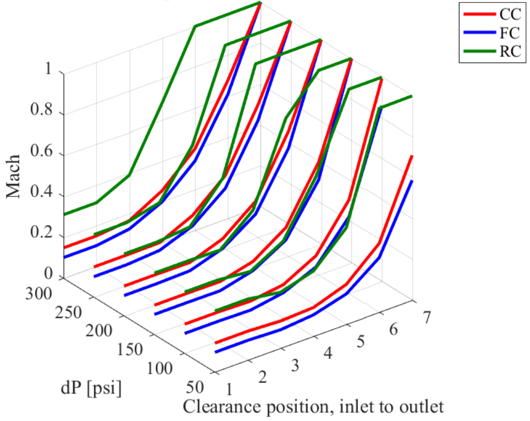

Mach in RC, 50 psi suction, 1800 RPM, 93% GVF

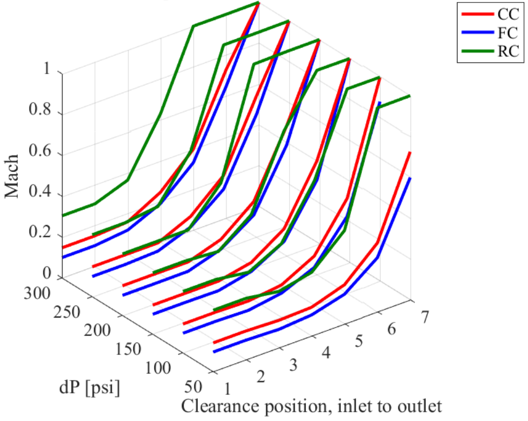

Mach in RC, 50 psi suction, 1800 RPM, 94% GVF

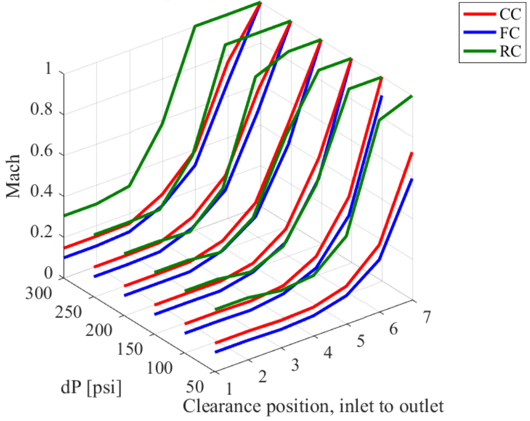

Mach in RC, 50 psi suction, 1800 RPM, 95% GVF

Mach in RC, 75 psi suction, 900 RPM, 47% GVF

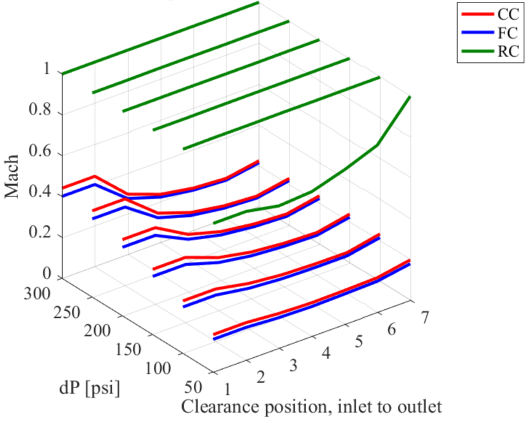

Mach in RC, 75 psi suction, 900 RPM, 66% GVF

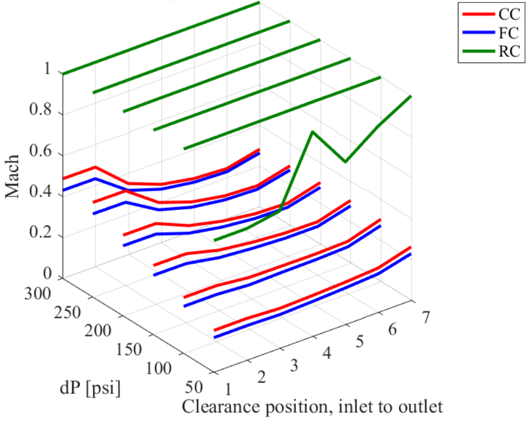

Mach in RC, 75 psi suction, 900 RPM, 85% GVF

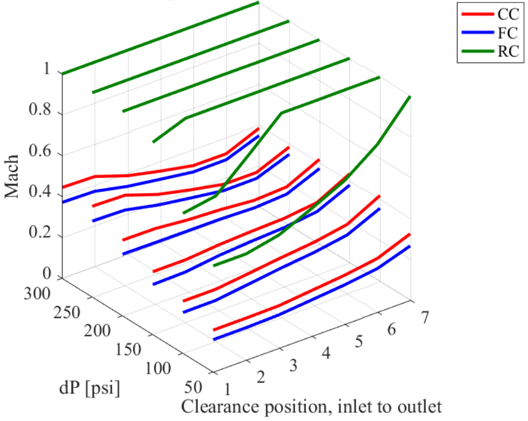

Mach in RC, 75 psi suction, 900 RPM, 90% GVF

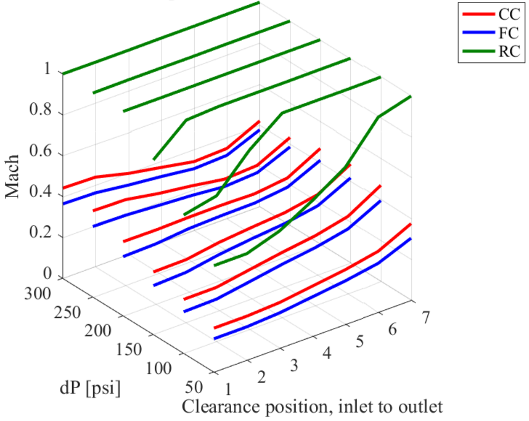

Mach in RC, 75 psi suction, 900 RPM, 93% GVF

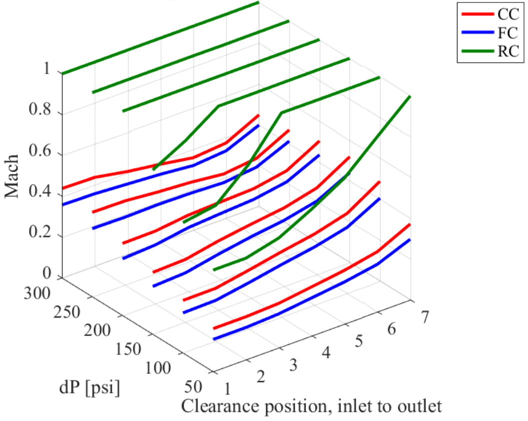

Mach in RC, 75 psi suction, 900 RPM, 94% GVF

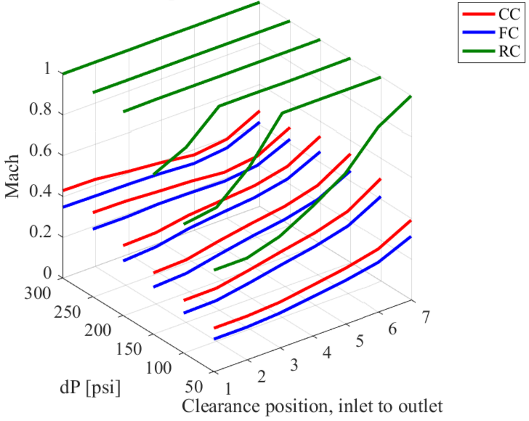

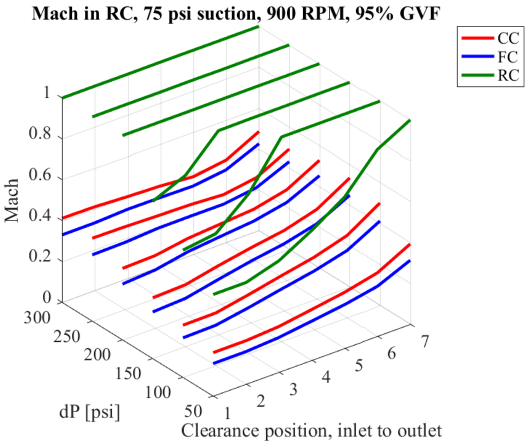
Mach in RC, 75 psi suction, 900 RPM, 95% GVF

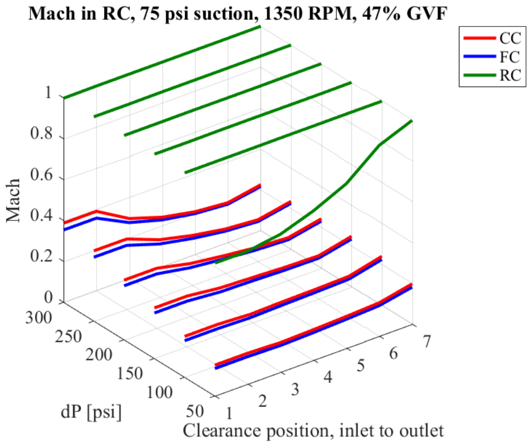
Mach in RC, 75 psi suction, 1350 RPM, 47% GVF

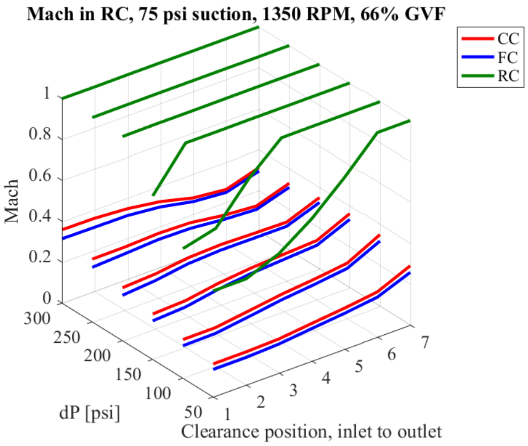
Mach in RC, 75 psi suction, 1350 RPM, 66% GVF

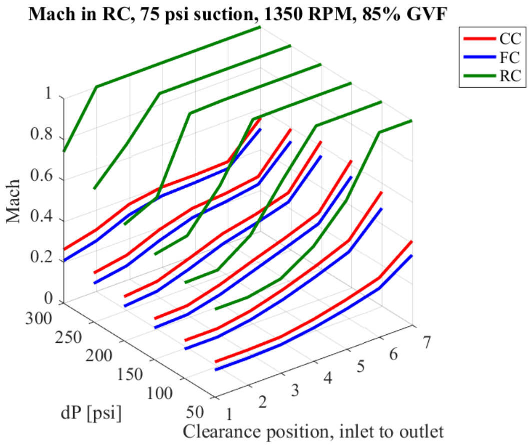
Mach in RC, 75 psi suction, 1350 RPM, 85% GVF

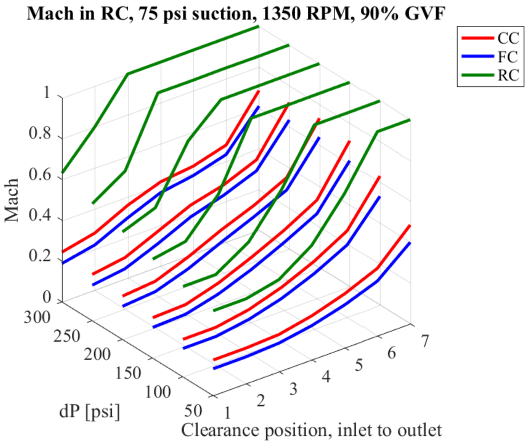
Mach in RC, 75 psi suction, 1350 RPM, 90% GVF

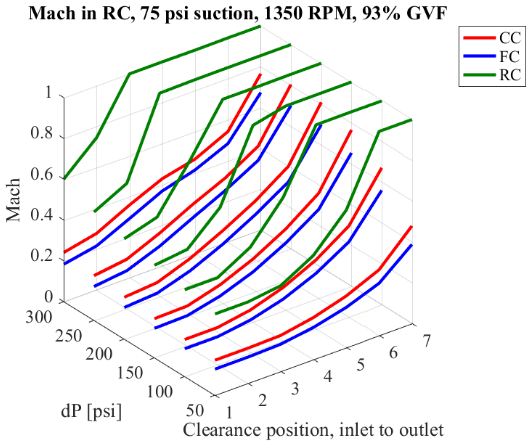
Mach in RC, 75 psi suction, 1350 RPM, 93% GVF

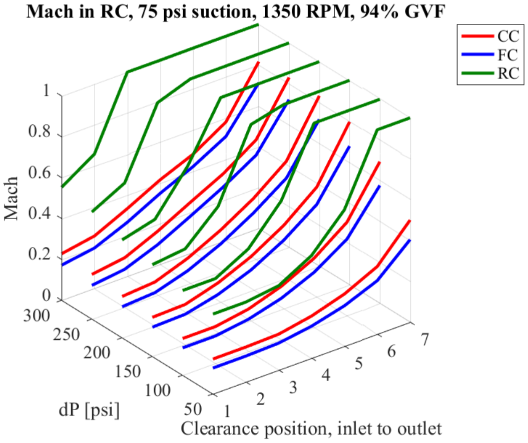
Mach in RC, 75 psi suction, 1350 RPM, 94% GVF

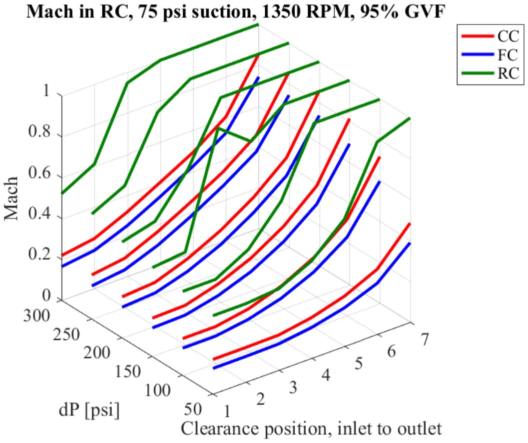
Mach in RC, 75 psi suction, 1350 RPM, 95% GVF

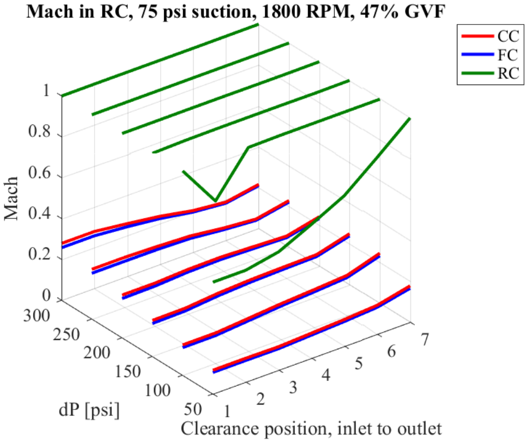
Mach in RC, 75 psi suction, 1800 RPM, 47% GVF

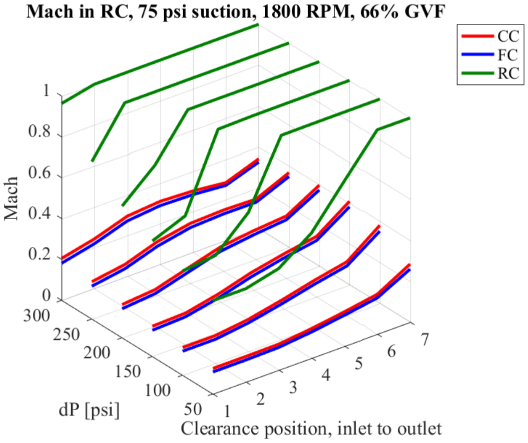
Mach in RC, 75 psi suction, 1800 RPM, 66% GVF

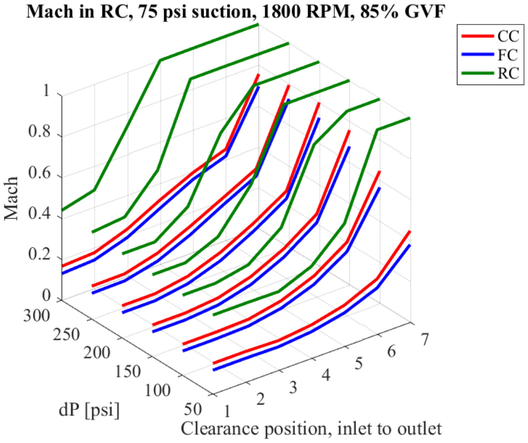
Mach in RC, 75 psi suction, 1800 RPM, 85% GVF

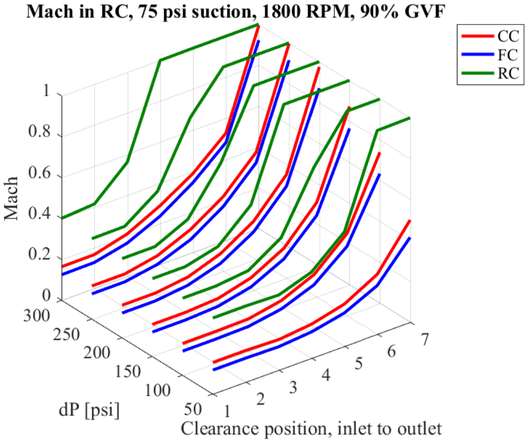
Mach in RC, 75 psi suction, 1800 RPM, 90% GVF

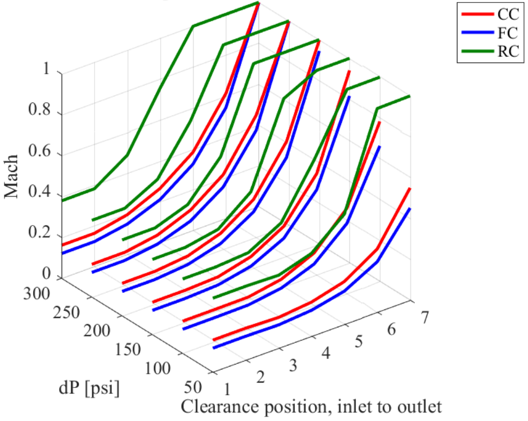
Mach in RC, 75 psi suction, 1800 RPM, 93% GVF

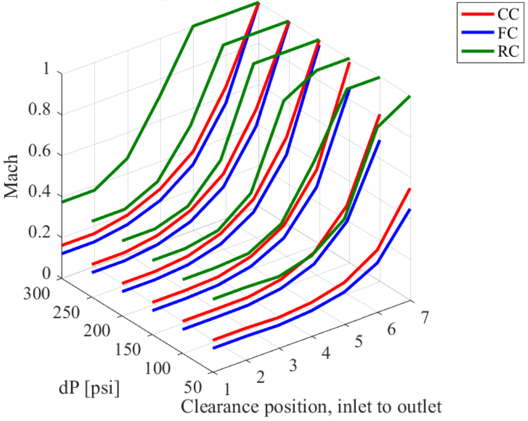
Mach in RC, 75 psi suction, 1800 RPM, 94% GVF

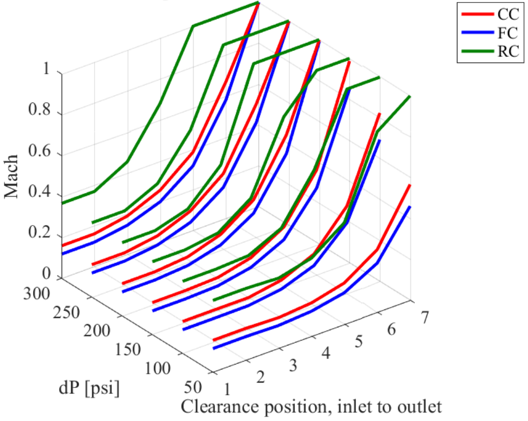
Mach in RC, 75 psi suction, 1800 RPM, 95% GVF

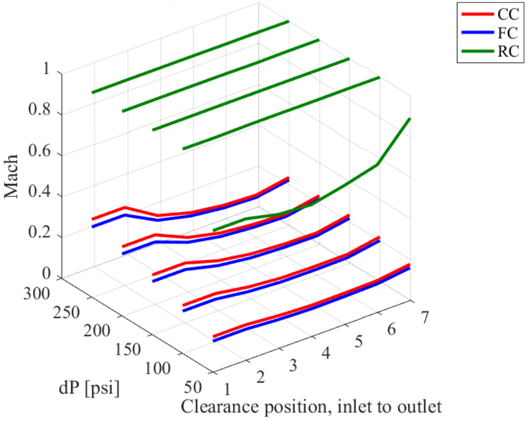
Mach in RC, 100 psi suction, 900 RPM, 47% GVF

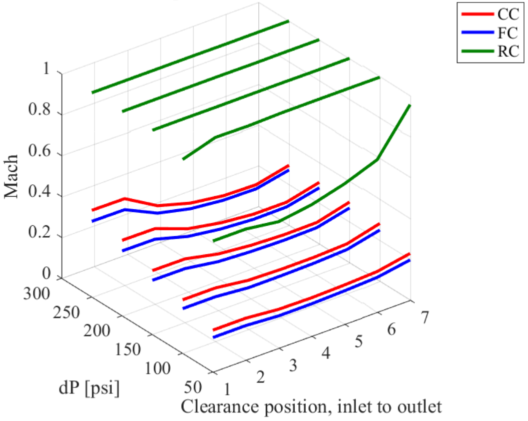
Mach in RC, 100 psi suction, 900 RPM, 66% GVF

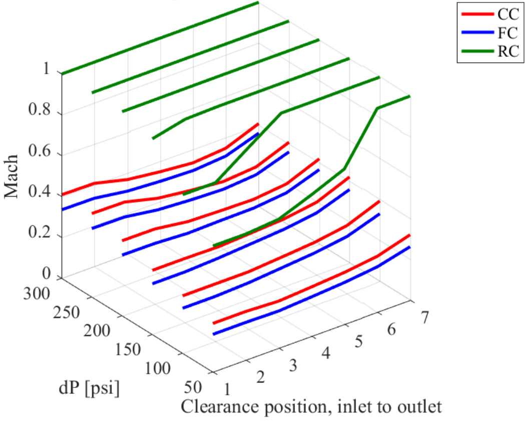
Mach in RC, 100 psi suction, 900 RPM, 85% GVF

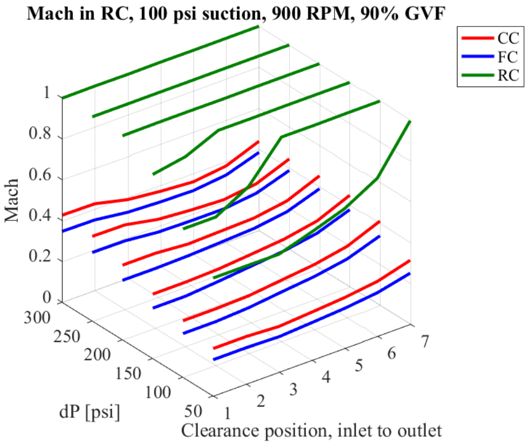
Mach in RC, 100 psi suction, 900 RPM, 90% GVF

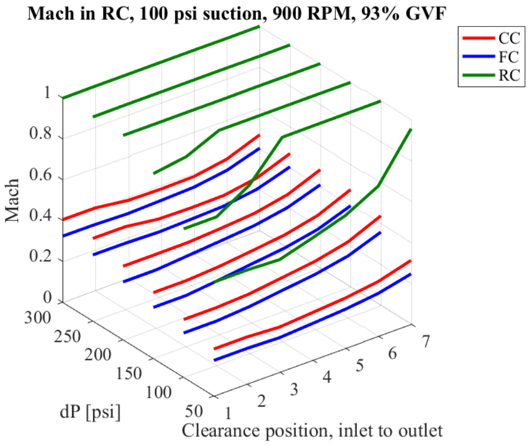
Mach in RC, 100 psi suction, 900 RPM, 93% GVF

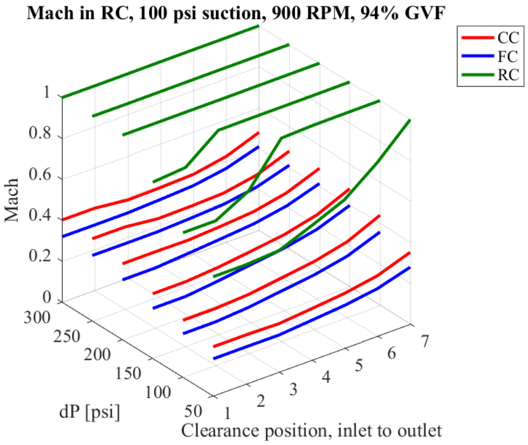
Mach in RC, 100 psi suction, 900 RPM, 94% GVF

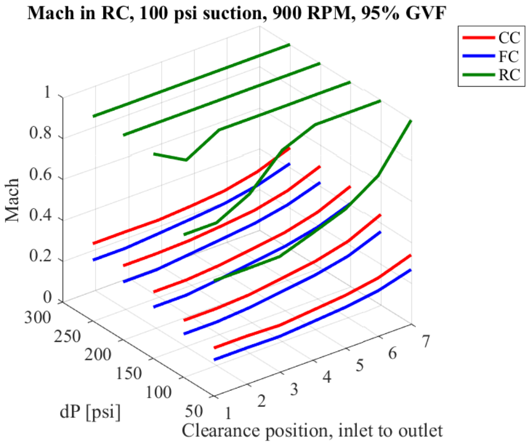
Mach in RC, 100 psi suction, 900 RPM, 95% GVF

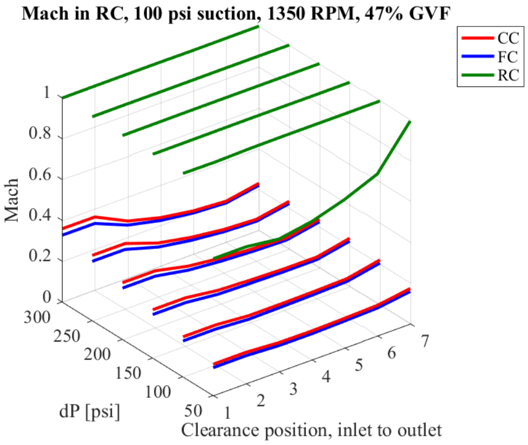
Mach in RC, 100 psi suction, 1350 RPM, 47% GVF

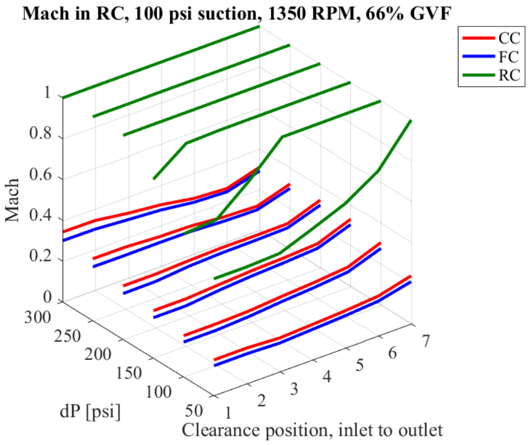
Mach in RC, 100 psi suction, 1350 RPM, 66% GVF

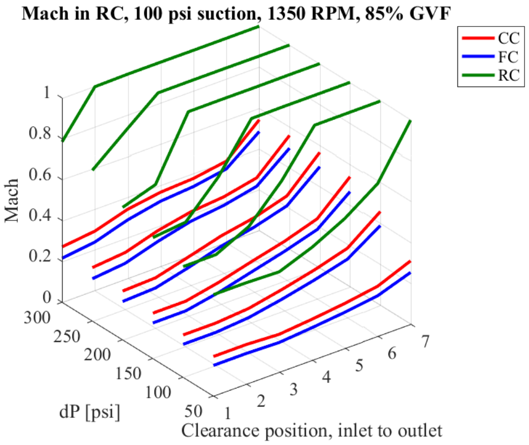
Mach in RC, 100 psi suction, 1350 RPM, 85% GVF

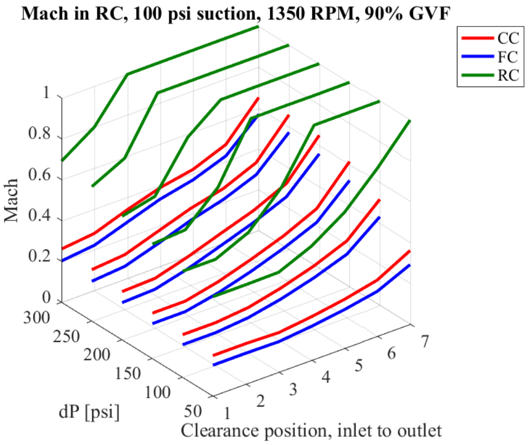
Mach in RC, 100 psi suction, 1350 RPM, 90% GVF

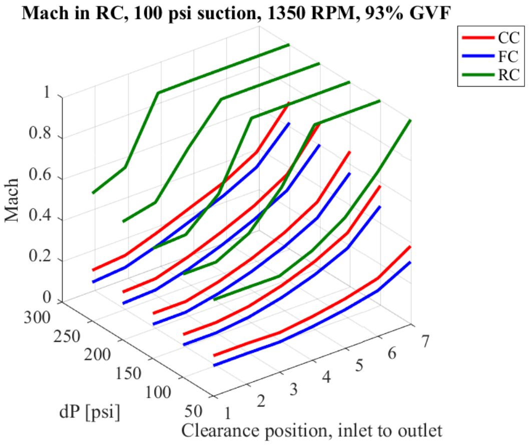
Mach in RC, 100 psi suction, 1350 RPM, 93% GVF

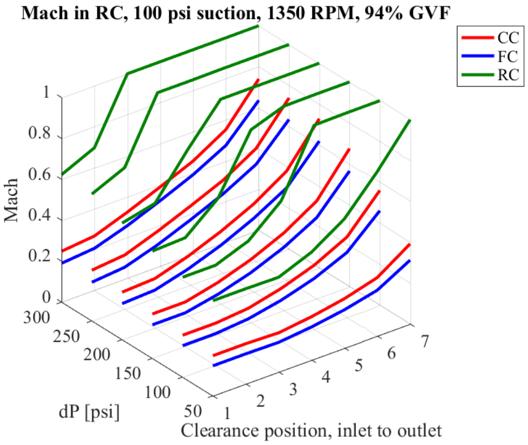
Mach in RC, 100 psi suction, 1350 RPM, 94% GVF

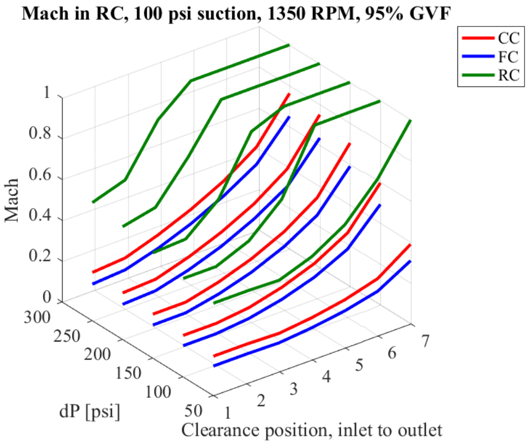
Mach in RC, 100 psi suction, 1350 RPM, 95% GVF

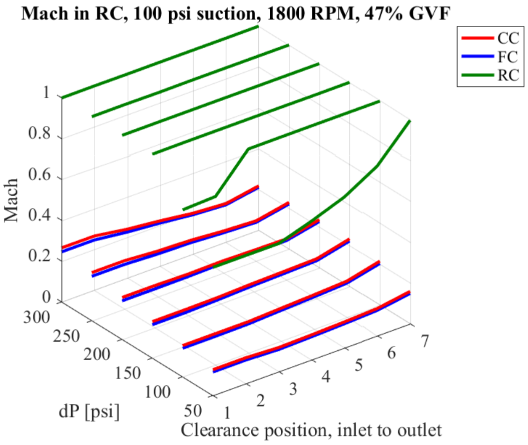
Mach in RC, 100 psi suction, 1800 RPM, 47% GVF

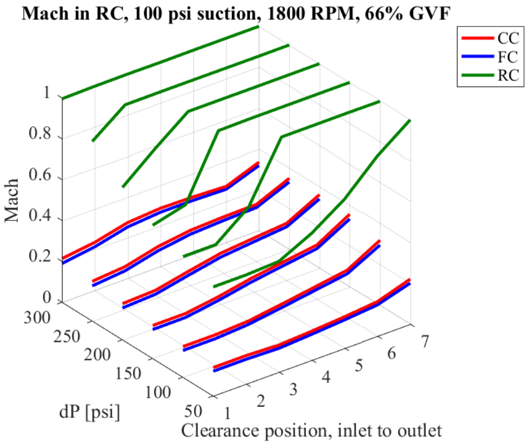
Mach in RC, 100 psi suction, 1800 RPM, 66% GVF

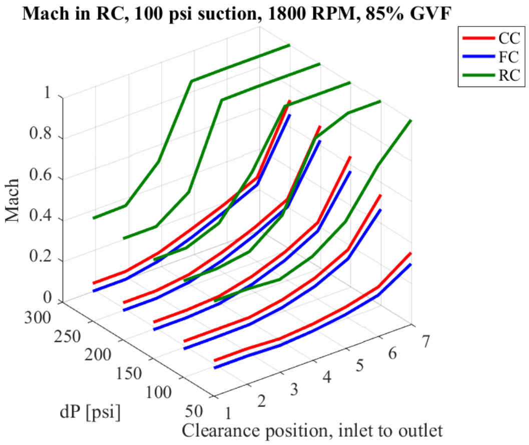
Mach in RC, 100 psi suction, 1800 RPM, 85% GVF

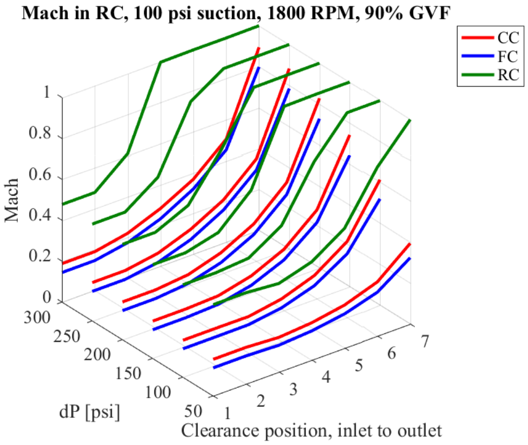
Mach in RC, 100 psi suction, 1800 RPM, 90% GVF

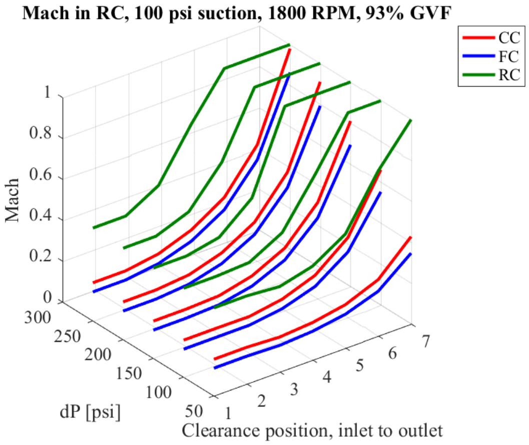
Mach in RC, 100 psi suction, 1800 RPM, 93% GVF

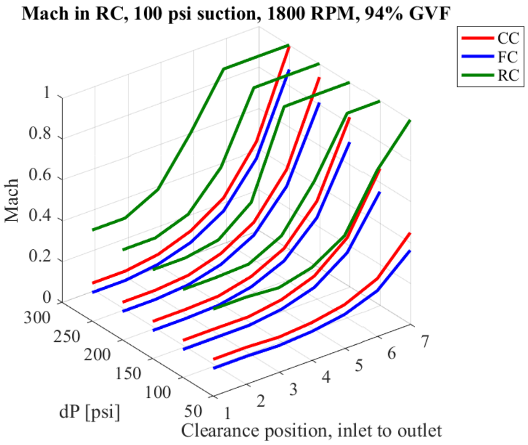
Mach in RC, 100 psi suction, 1800 RPM, 94% GVF

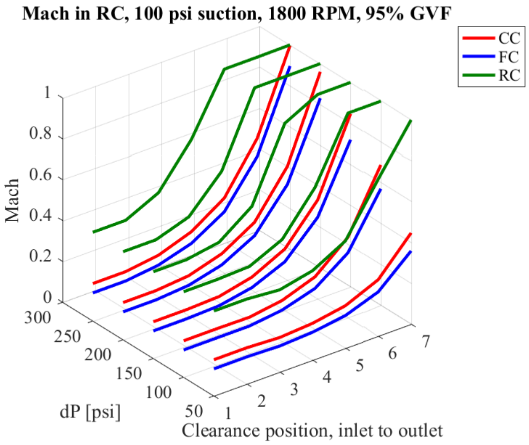
Mach in RC, 100 psi suction, 1800 RPM, 95% GVF

## A.3. Proportion of Leakage Flow Through Each Clearance and Pressure Distributions

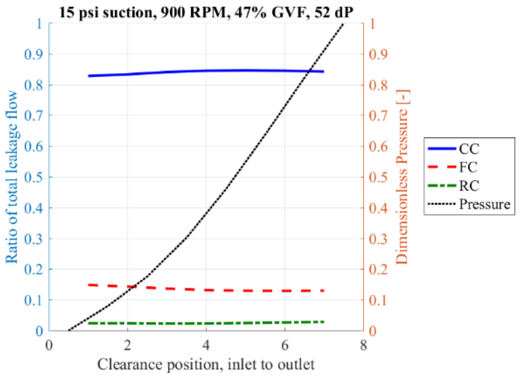

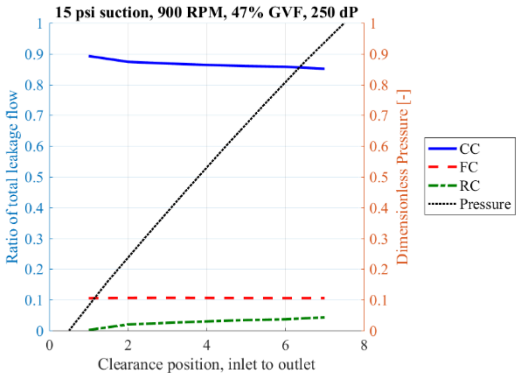

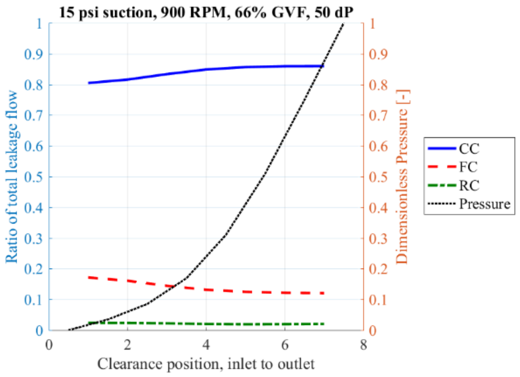

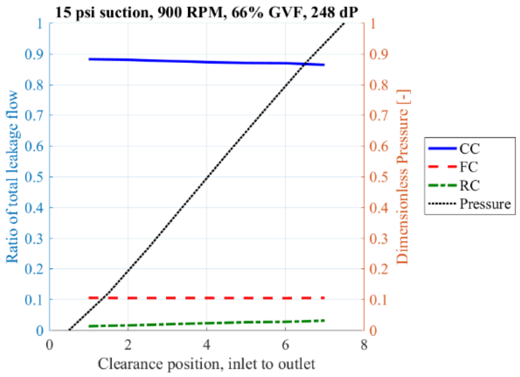

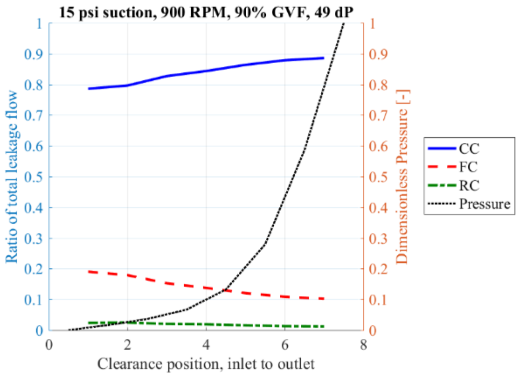

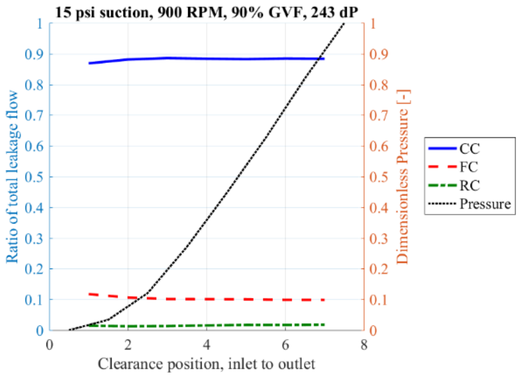

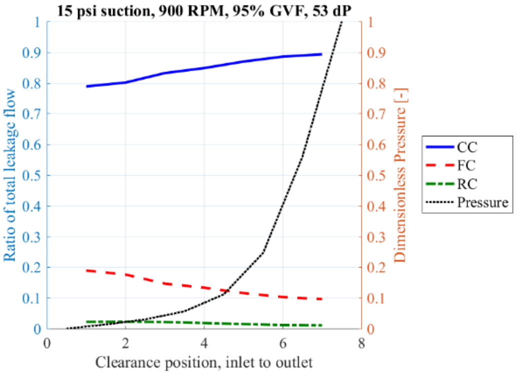
15 psi suction, 900 RPM, 95% GVF, 53 dP

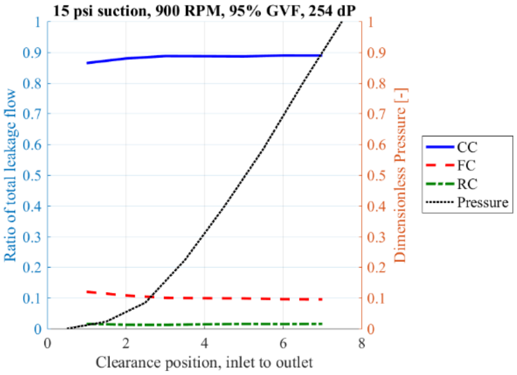
15 psi suction, 900 RPM, 95% GVF, 254 dP

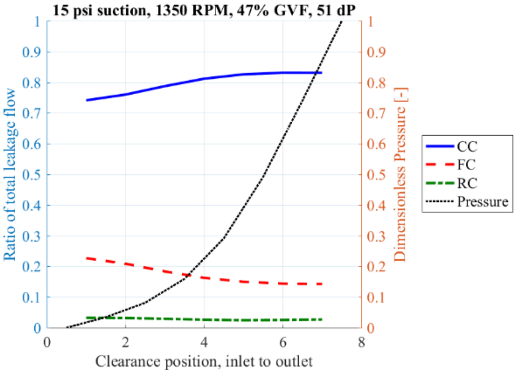
15 psi suction, 1350 RPM, 47% GVF, 51 dP

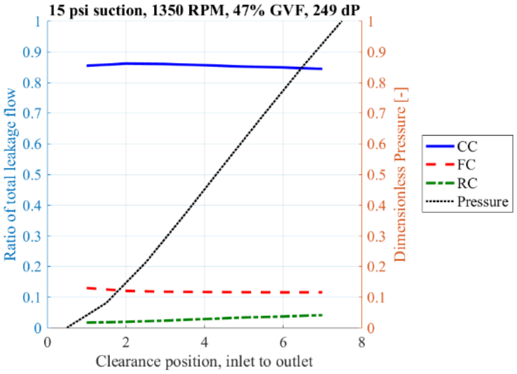
15 psi suction, 1350 RPM, 47% GVF, 249 dP

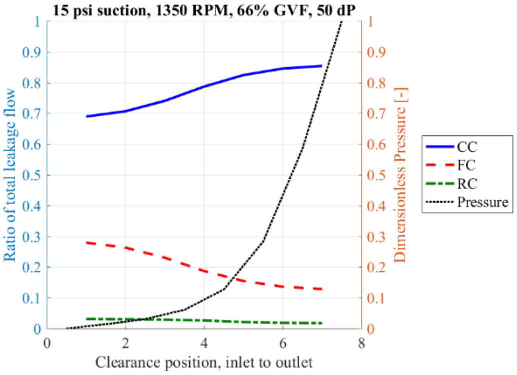
15 psi suction, 1350 RPM, 66% GVF, 50 dP

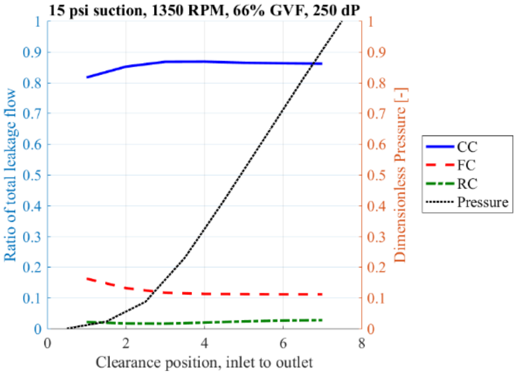
15 psi suction, 1350 RPM, 66% GVF, 250 dP

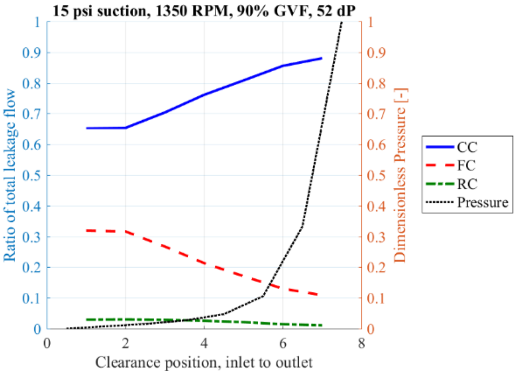
15 psi suction, 1350 RPM, 90% GVF, 52 dP

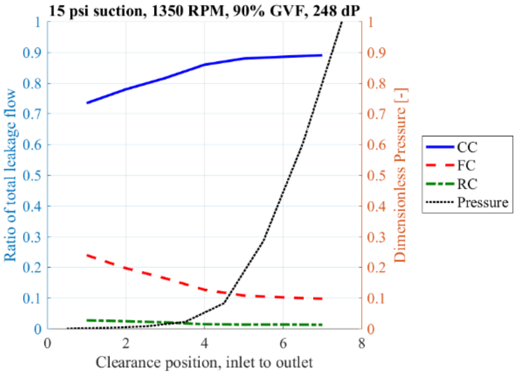
15 psi suction, 1350 RPM, 90% GVF, 248 dP

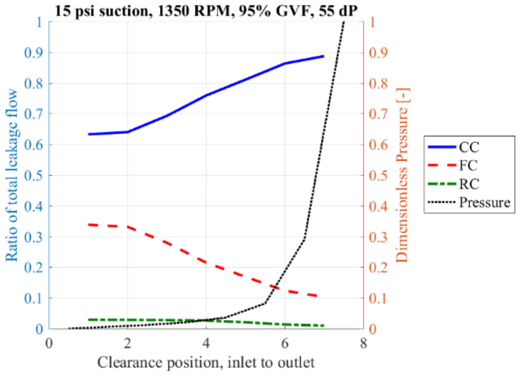
15 psi suction, 1350 RPM, 95% GVF, 55 dP
Ratio of total leakage flow
Dimensionless Pressure [-]
Clearance position, inlet to outlet
0
0.1
0.2
0.3
0.4
0.5
0.6
0.7
0.8
0.9
1
0
2
4
6
8
CC
FC
RC
Pressure

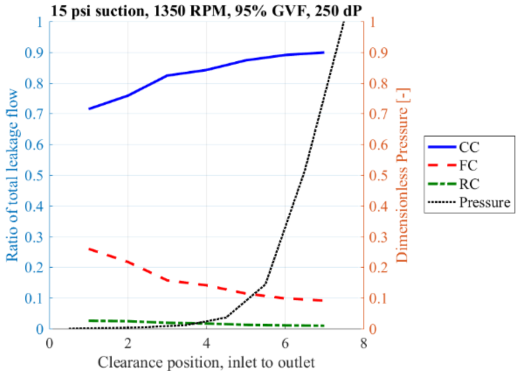
15 psi suction, 1350 RPM, 95% GVF, 250 dP
Ratio of total leakage flow
Dimensionless Pressure [-]
Clearance position, inlet to outlet
0
0.1
0.2
0.3
0.4
0.5
0.6
0.7
0.8
0.9
1
0
2
4
6
8
CC
FC
RC
Pressure

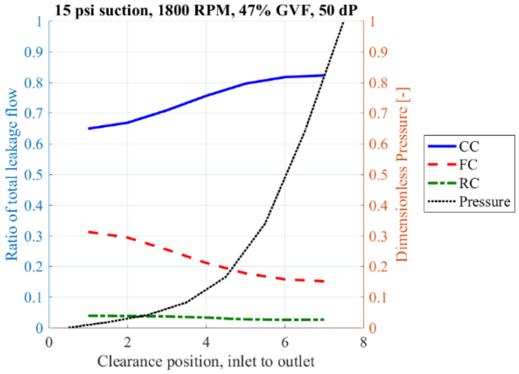
15 psi suction, 1800 RPM, 47% GVF, 50 dP
Ratio of total leakage flow
Dimensionless Pressure [-]
Clearance position, inlet to outlet
0
0.1
0.2
0.3
0.4
0.5
0.6
0.7
0.8
0.9
1
0
2
4
6
8
CC
FC
RC
Pressure

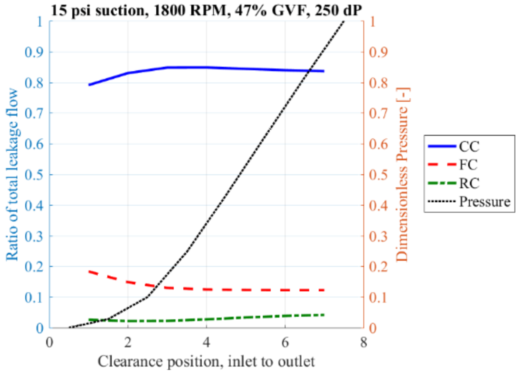
15 psi suction, 1800 RPM, 47% GVF, 250 dP
Ratio of total leakage flow
Dimensionless Pressure [-]
Clearance position, inlet to outlet
0
0.1
0.2
0.3
0.4
0.5
0.6
0.7
0.8
0.9
1
0
2
4
6
8
CC
FC
RC
Pressure

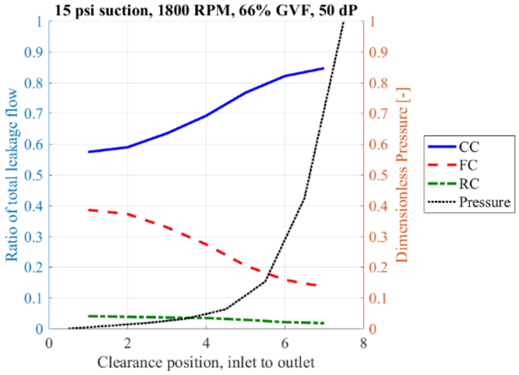
15 psi suction, 1800 RPM, 66% GVF, 50 dP
Ratio of total leakage flow
Dimensionless Pressure [-]
Clearance position, inlet to outlet
0
0.1
0.2
0.3
0.4
0.5
0.6
0.7
0.8
0.9
1
0
2
4
6
8
CC
FC
RC
Pressure

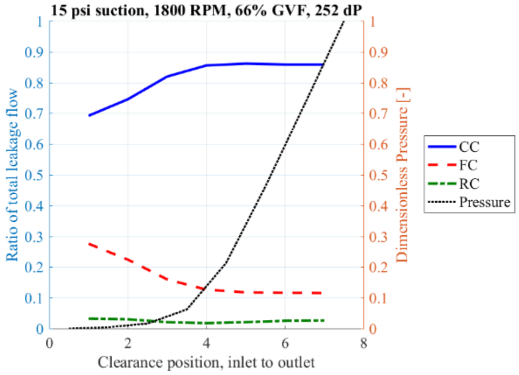
15 psi suction, 1800 RPM, 66% GVF, 252 dP
Ratio of total leakage flow
Dimensionless Pressure [-]
Clearance position, inlet to outlet
0
0.1
0.2
0.3
0.4
0.5
0.6
0.7
0.8
0.9
1
0
2
4
6
8
CC
FC
RC
Pressure

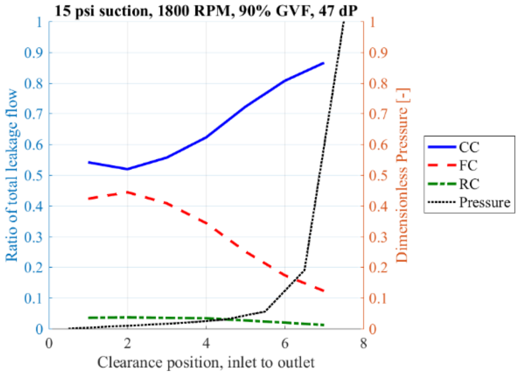
15 psi suction, 1800 RPM, 90% GVF, 47 dP
Ratio of total leakage flow
Dimensionless Pressure [-]
Clearance position, inlet to outlet
0
0.1
0.2
0.3
0.4
0.5
0.6
0.7
0.8
0.9
1
0
2
4
6
8
CC
FC
RC
Pressure

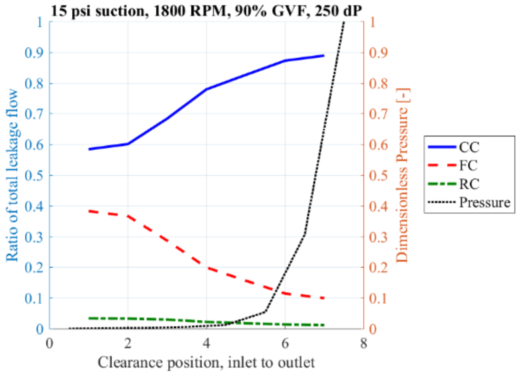
15 psi suction, 1800 RPM, 90% GVF, 250 dP
Ratio of total leakage flow
Dimensionless Pressure [-]
Clearance position, inlet to outlet
0
0.1
0.2
0.3
0.4
0.5
0.6
0.7
0.8
0.9
1
0
2
4
6
8
CC
FC
RC
Pressure

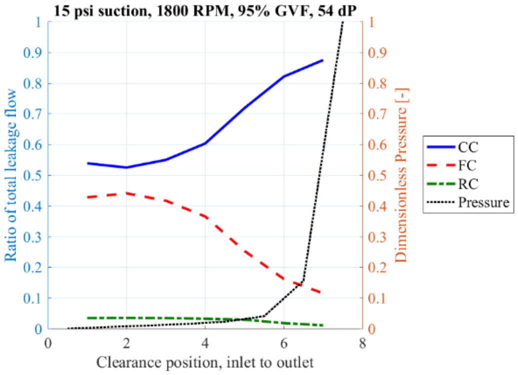
15 psi suction, 1800 RPM, 95% GVF, 54 dP

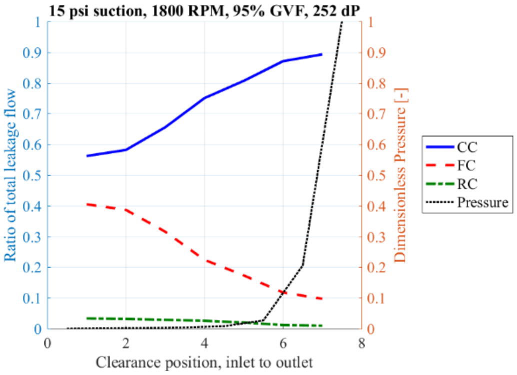
15 psi suction, 1800 RPM, 95% GVF, 252 dP

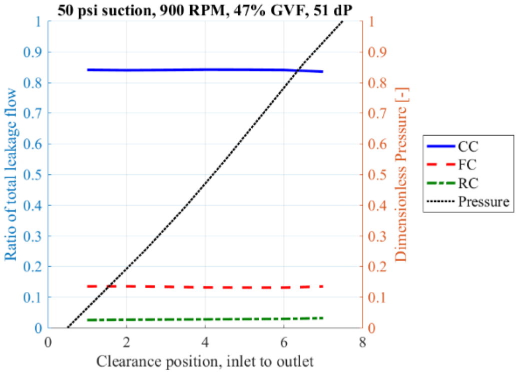
50 psi suction, 900 RPM, 47% GVF, 51 dP

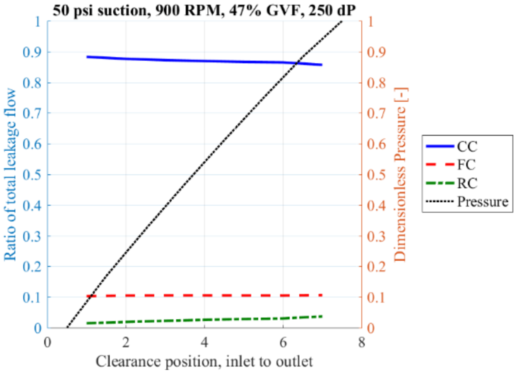
50 psi suction, 900 RPM, 47% GVF, 250 dP

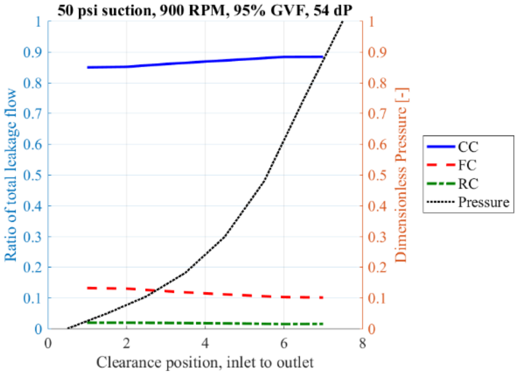
50 psi suction, 900 RPM, 95% GVF, 54 dP

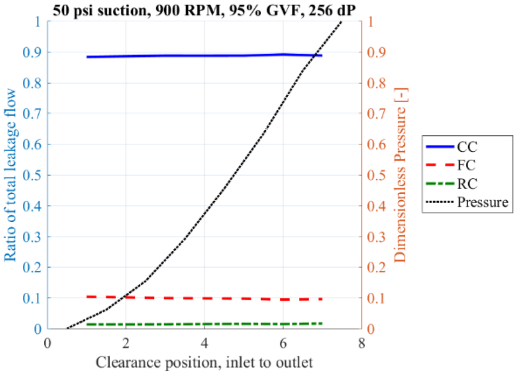
50 psi suction, 900 RPM, 95% GVF, 256 dP

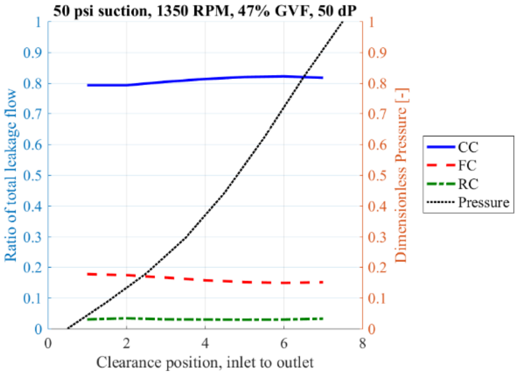
50 psi suction, 1350 RPM, 47% GVF, 50 dP

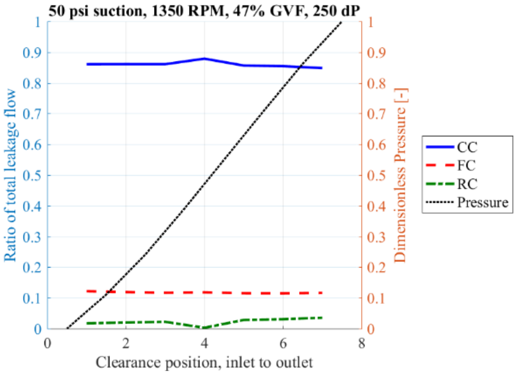
50 psi suction, 1350 RPM, 47% GVF, 250 dP

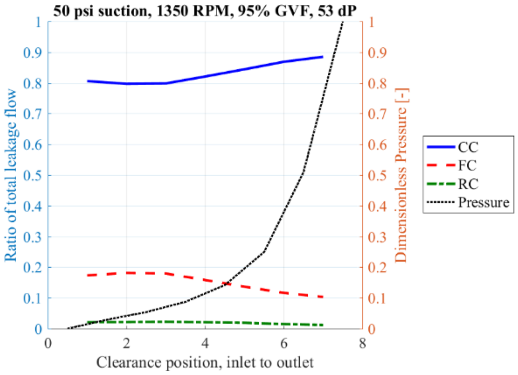
50 psi suction, 1350 RPM, 95% GVF, 53 dP

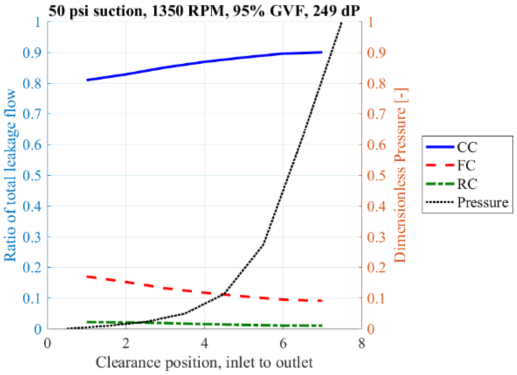
50 psi suction, 1350 RPM, 95% GVF, 249 dP

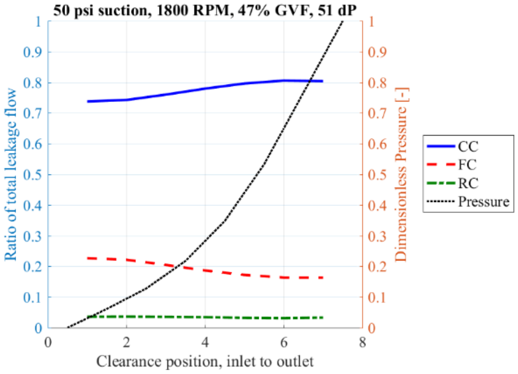
50 psi suction, 1800 RPM, 47% GVF, 51 dP

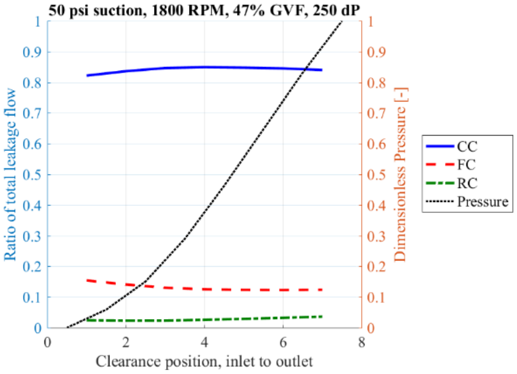
50 psi suction, 1800 RPM, 47% GVF, 250 dP

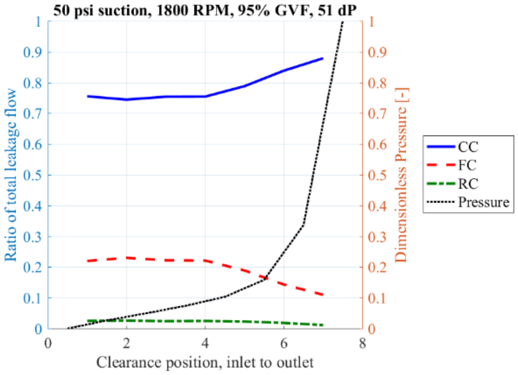
50 psi suction, 1800 RPM, 95% GVF, 51 dP

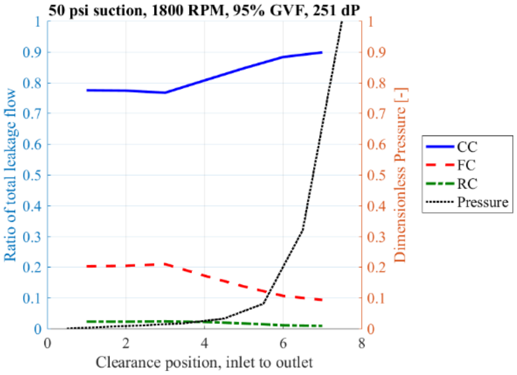
50 psi suction, 1800 RPM, 95% GVF, 251 dP

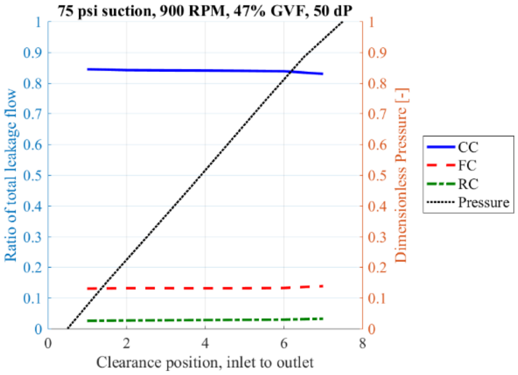
75 psi suction, 900 RPM, 47% GVF, 50 dP

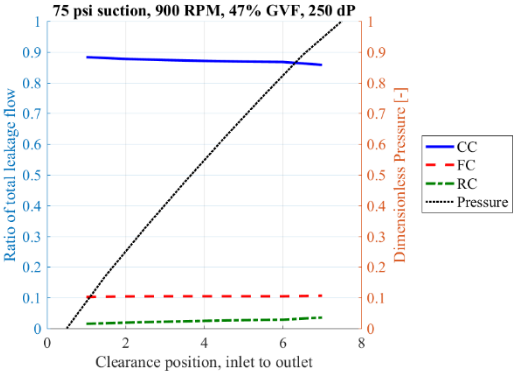
75 psi suction, 900 RPM, 47% GVF, 250 dP

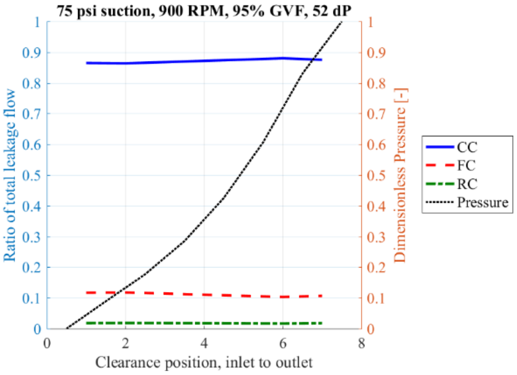
75 psi suction, 900 RPM, 95% GVF, 52 dP

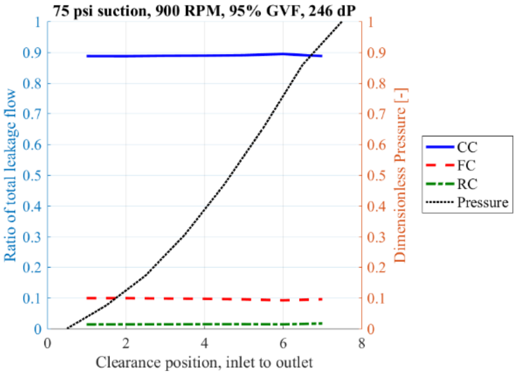
75 psi suction, 900 RPM, 95% GVF, 246 dP

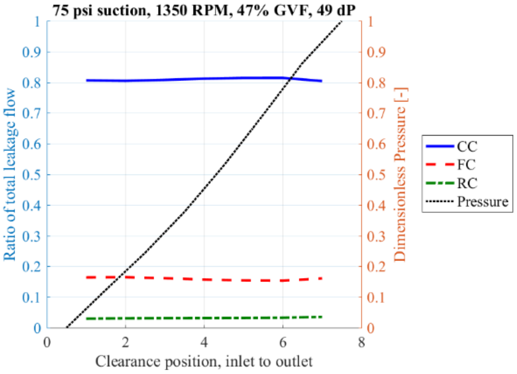
75 psi suction, 1350 RPM, 47% GVF, 49 dP

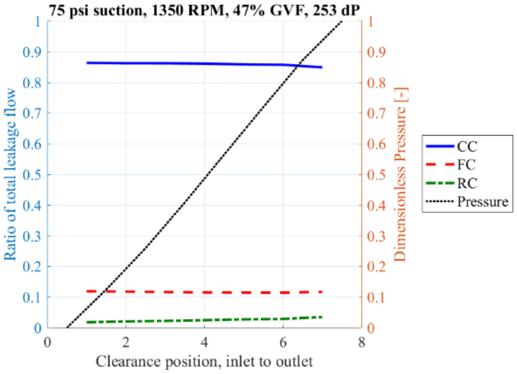
75 psi suction, 1350 RPM, 47% GVF, 253 dP

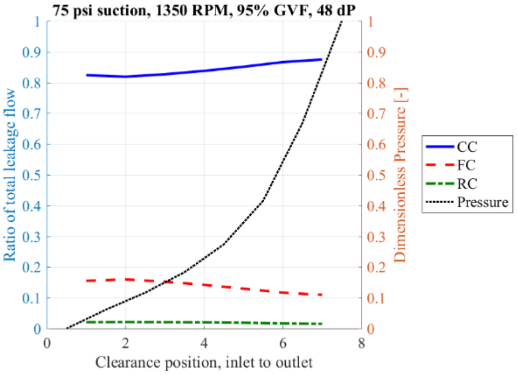
75 psi suction, 1350 RPM, 95% GVF, 48 dP

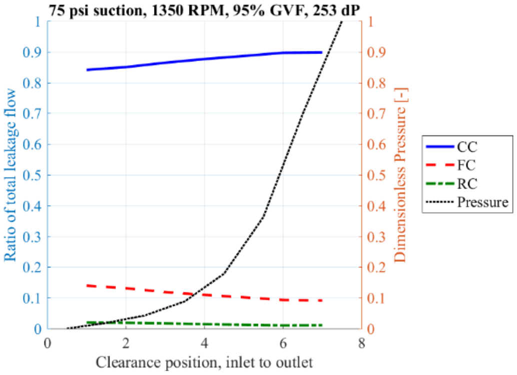
75 psi suction, 1350 RPM, 95% GVF, 253 dP

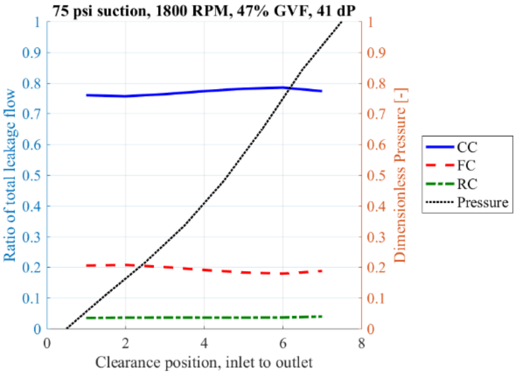
75 psi suction, 1800 RPM, 47% GVF, 41 dP

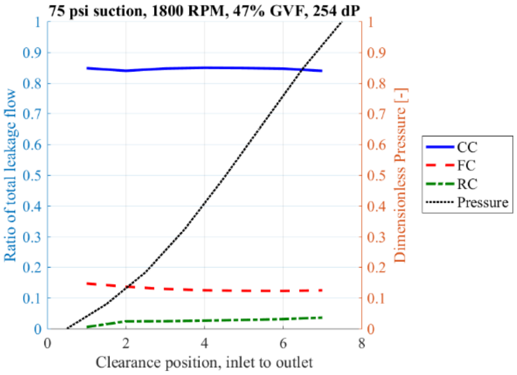
75 psi suction, 1800 RPM, 47% GVF, 254 dP

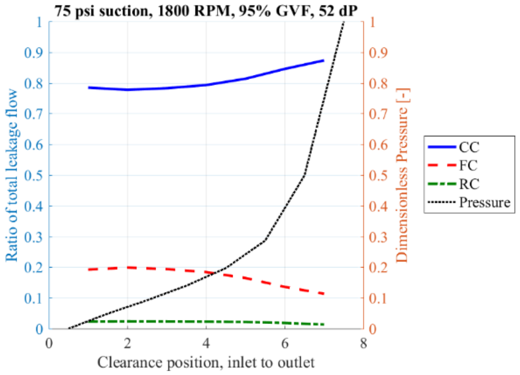
75 psi suction, 1800 RPM, 95% GVF, 52 dP

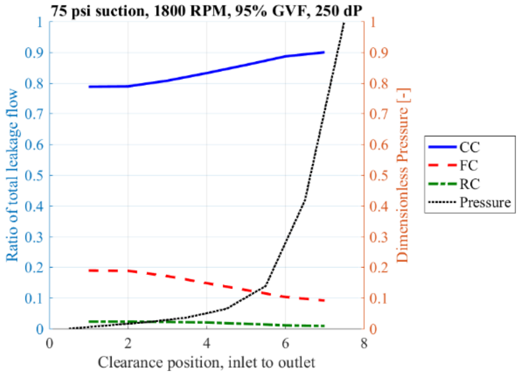
75 psi suction, 1800 RPM, 95% GVF, 250 dP

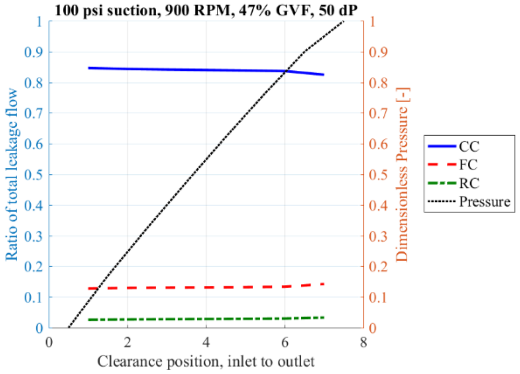
100 psi suction, 900 RPM, 47% GVF, 50 dP

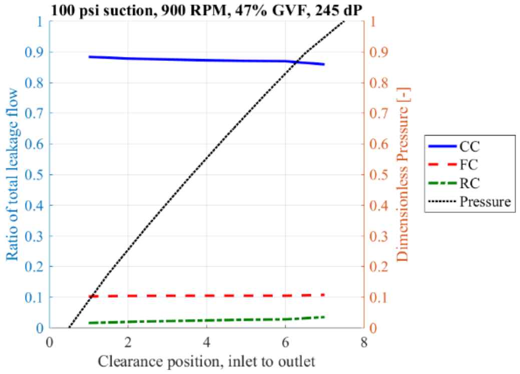
100 psi suction, 900 RPM, 47% GVF, 245 dP

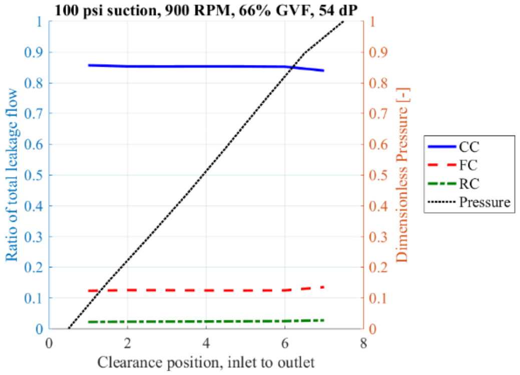
100 psi suction, 900 RPM, 66% GVF, 54 dP

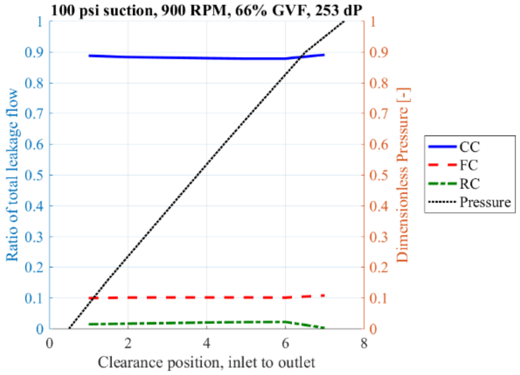
100 psi suction, 900 RPM, 66% GVF, 253 dP

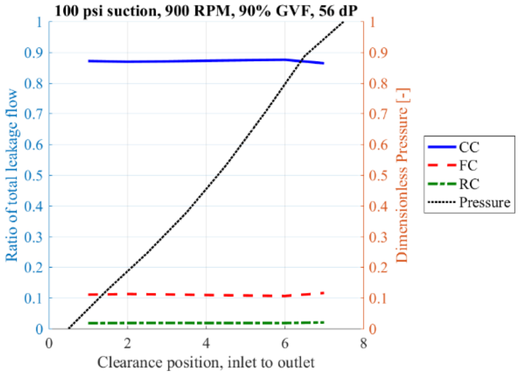
100 psi suction, 900 RPM, 90% GVF, 56 dP

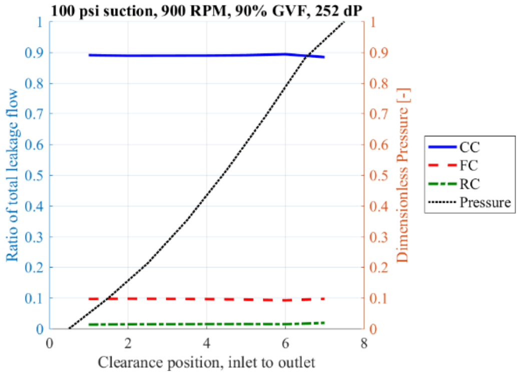
100 psi suction, 900 RPM, 90% GVF, 252 dP

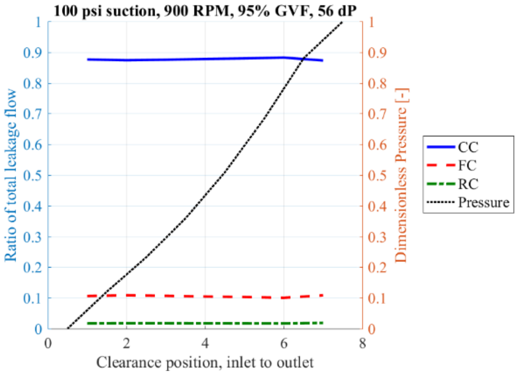
100 psi suction, 900 RPM, 95% GVF, 56 dP

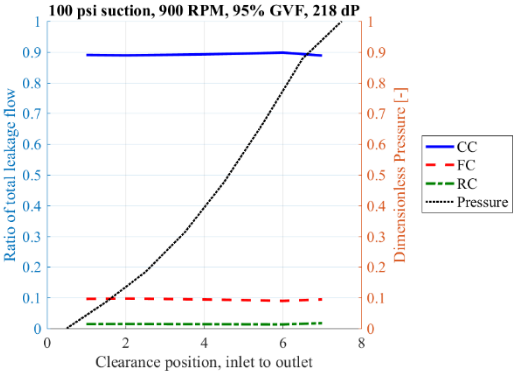
100 psi suction, 900 RPM, 95% GVF, 218 dP

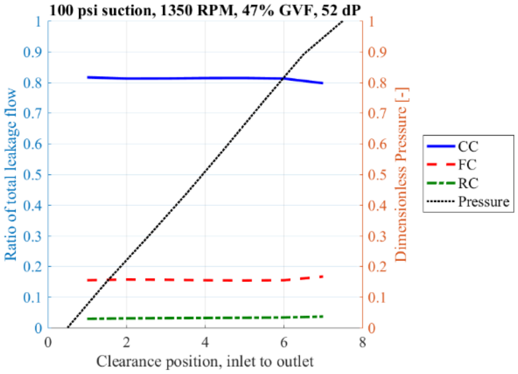
100 psi suction, 1350 RPM, 47% GVF, 52 dP

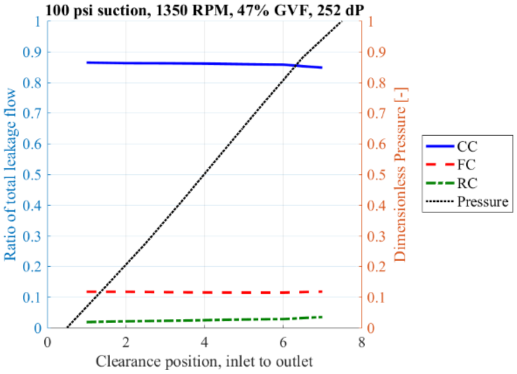
100 psi suction, 1350 RPM, 47% GVF, 252 dP

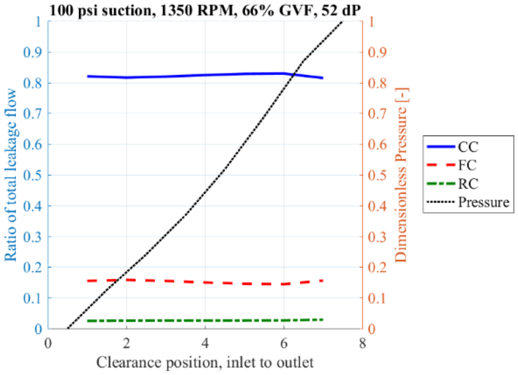
100 psi suction, 1350 RPM, 66% GVF, 52 dP

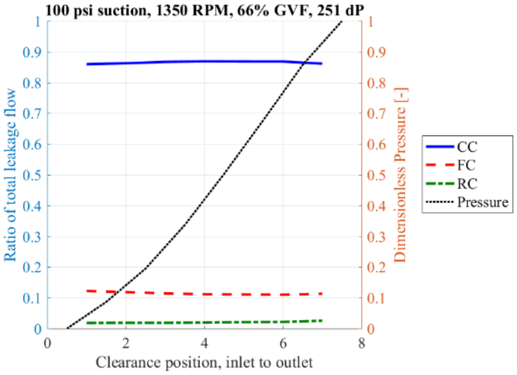
100 psi suction, 1350 RPM, 66% GVF, 251 dP

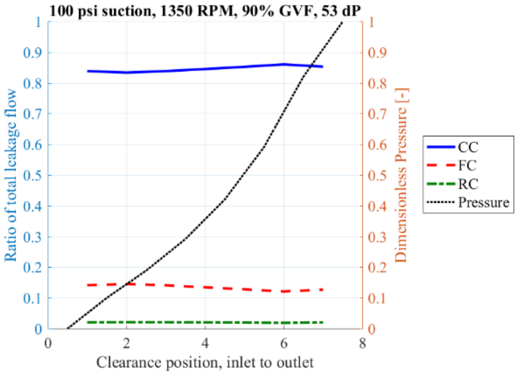
100 psi suction, 1350 RPM, 90% GVF, 53 dP

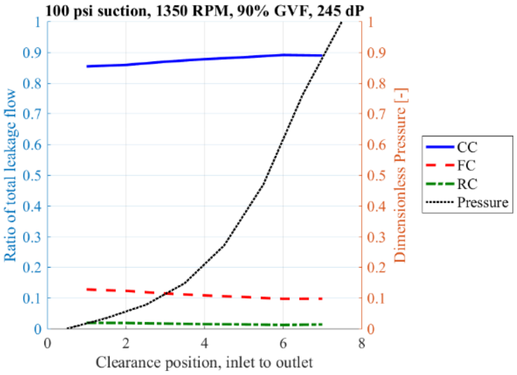
100 psi suction, 1350 RPM, 90% GVF, 245 dP

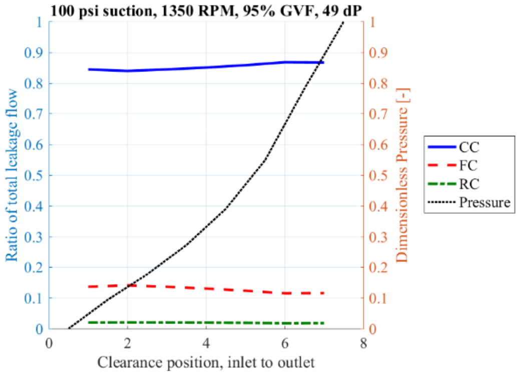
100 psi suction, 1350 RPM, 95% GVF, 49 dP
Ratio of total leakage flow
Dimensionless Pressure [-]
Clearance position, inlet to outlet
CC
FC
RC
Pressure

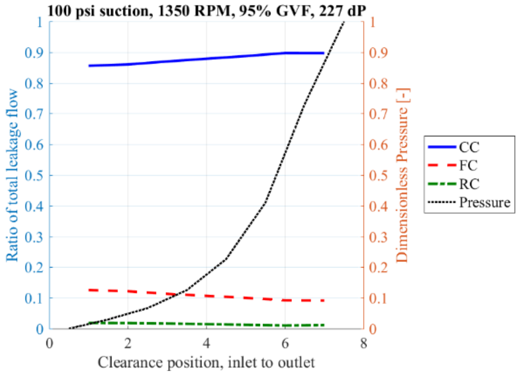
100 psi suction, 1350 RPM, 95% GVF, 227 dP
Ratio of total leakage flow
Dimensionless Pressure [-]
Clearance position, inlet to outlet
CC
FC
RC
Pressure

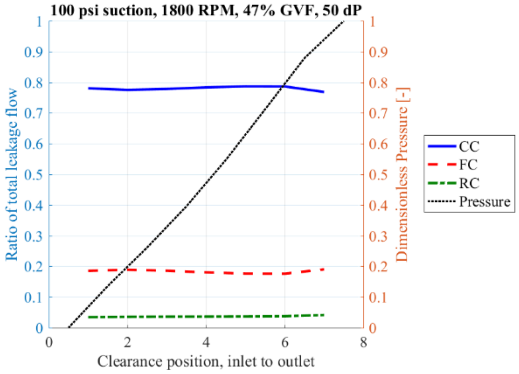
100 psi suction, 1800 RPM, 47% GVF, 50 dP
Ratio of total leakage flow
Dimensionless Pressure [-]
Clearance position, inlet to outlet
CC
FC
RC
Pressure

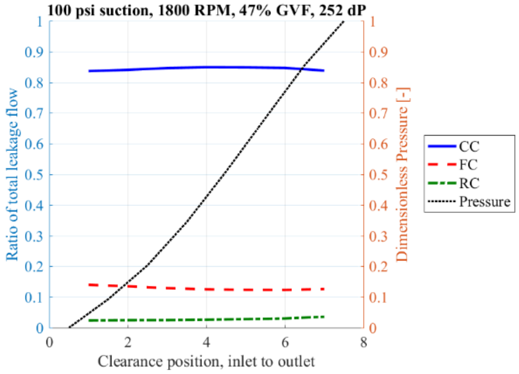
100 psi suction, 1800 RPM, 47% GVF, 252 dP
Ratio of total leakage flow
Dimensionless Pressure [-]
Clearance position, inlet to outlet
CC
FC
RC
Pressure

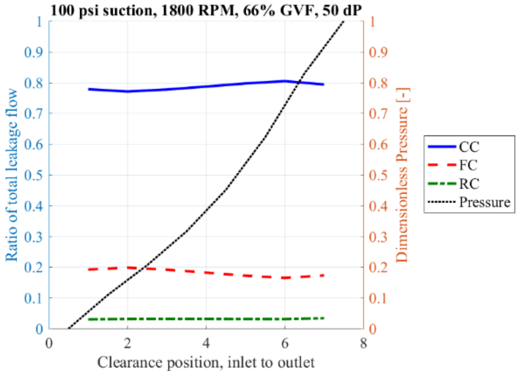
100 psi suction, 1800 RPM, 66% GVF, 50 dP
Ratio of total leakage flow
Dimensionless Pressure [-]
Clearance position, inlet to outlet
CC
FC
RC
Pressure

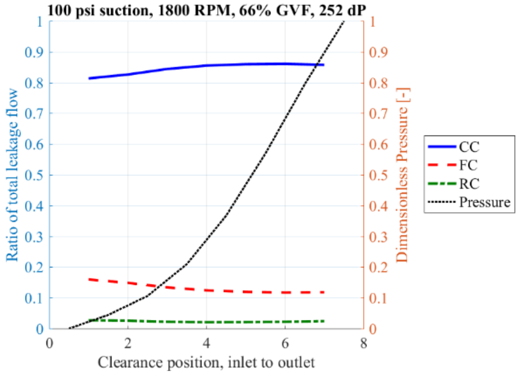
100 psi suction, 1800 RPM, 66% GVF, 252 dP
Ratio of total leakage flow
Dimensionless Pressure [-]
Clearance position, inlet to outlet
CC
FC
RC
Pressure

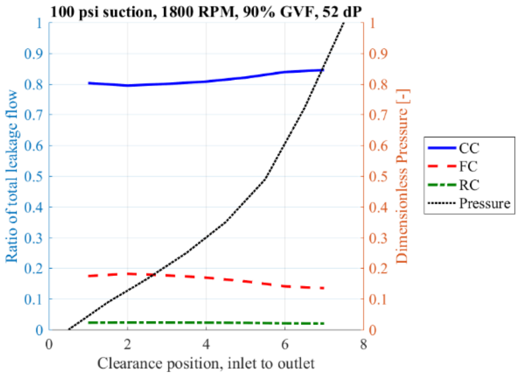
100 psi suction, 1800 RPM, 90% GVF, 52 dP

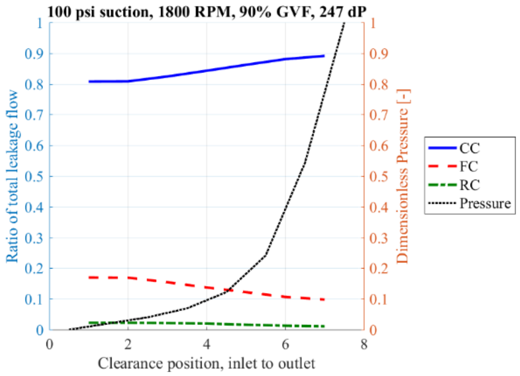
100 psi suction, 1800 RPM, 90% GVF, 247 dP

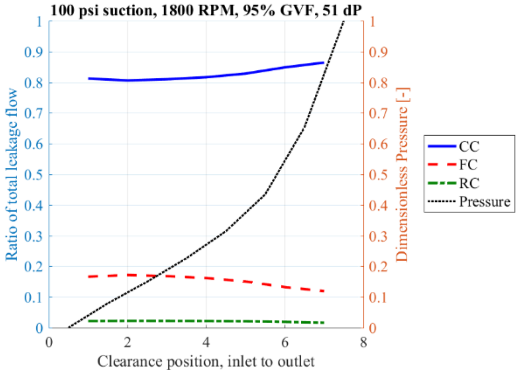
100 psi suction, 1800 RPM, 95% GVF, 51 dP

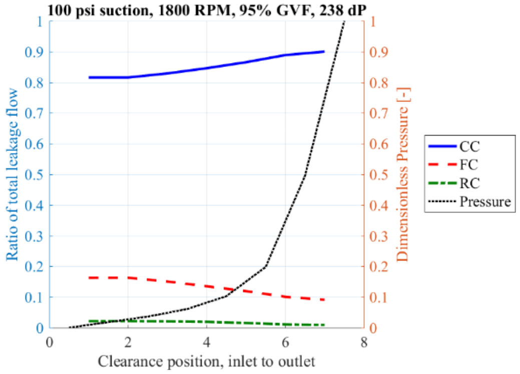
100 psi suction, 1800 RPM, 95% GVF, 238 dP